INAUGURAL - DISSERTATION

zur
Erlangung der Doktorwürde
der
Naturwissenschaftlich-Mathematischen
Gesamtfakultät
der

Ruprecht - Karls -Universität
Heidelberg

vorgelegt von
Dipl.-Phys. Jens Dilling
aus Heidelberg

Tag der mündlichen Prüfung: 23.05. 2001

Direkte Massenmessungen an exotischen Kernen mit SHIPTRAP und ISOLTRAP

Gutachter: Prof. Dr. H.-Jürgen Kluge

Prof. Dr. Andreas Wolf

Dissertation
submitted to the
Combined Faculties for the Natural Sciences and for Mathematics
of the Rupertus Carola University of
Heidelberg, Germany
for the degree of
Doctor of Natural Sciences

Direct Mass Measurements on Exotic Nuclei with SHIPTRAP and ISOLTRAP

presented by
Diplom-Physicist: Jens Dilling
born in: Heidelberg

Heidelberg, 23.05. 2001

Referees: Prof. Dr. H.-Jürgen Kluge

Prof. Dr. Andreas Wolf

Direkte Massenmessungen an exotischen Kernen mit SHIPTRAP und ISOLTRAP - Mit dem Penningfallenspektrometer ISOLTRAP am on-line Separator ISOLDE/CERN wurden direkte Massenmessungen an exotischen Xenonkernen im Bereich $114 \leq A \leq 124$ durchgeführt. Die Massen der Isotope $^{114-116}$Xe konnten zum ersten Mal gemessen werden. Mit den erhaltenen Daten wurde eine Anpassung der atomaren Massen vorgenommen. Im Vergleich mit vorhergehenden Experimenten fanden sich Diskrepanzen von bis zu $7,7$ Standardabweichungen. Diese wurden untersucht und konnten geklärt werden. Desweiteren wurde das Verhalten der Zweineutronenseparationsenergie im Bezug auf Nachbarelemente betrachtet. Hier zeigt sich ein insgesamt glatter Verlauf, was auf die Abwesenheit von drastischen Kernstruktureffekten schließen läßt. Aus dem Vergleich mit mittleren Ladungsradien und dem Fehlen von isomeren Zuständen ergibt sich , daß keine Kernformkoexistenz vorliegt. Diese Messungen waren nur durch den Einbau einer neuartigen puffergasgefüllten linearen Radiofrequenzquadrupol (RFQ)-Falle möglich. Im Rahmen dieser Arbeit wurde ein Prototyp eines solchen RFQ für ISOLTRAP entwickelt, eingebaut und getestet. Für das SHIPTRAP-Experiment, das nach dem Wienfilter SHIP bei GSI/Darmstadt aufgebaut wird, wurde ein weiterer RFQ gebaut und erste Transmissionsexperimente durchgeführt. Das SHIPTRAP-Experiment wird es möglich machen, radioaktive Sekundärstrahlen mit MeV/u-Energien zu stoppen, zu kühlen und in einer Ionenfallenanlage zu speichern. Es wurde untersucht, an welchen transuranischen Kernen erste Massenmessungen mit SHIPTRAP durchgeführt werden können.

Direct mass measurements on exotic nuclei with SHIPTRAP and ISOLTRAP - Direct mass measurements on exotic xenon nuclei with $114 \leq A \leq 124$ were carried out at the Penning trap spectrometer ISOLTRAP installed at the on-line separator ISOLDE/CERN. The masses of the isotopes $^{114-116}$Xe were determined for the first time. An atomic mass evaluation was performed taking the new data into account. In comparison with previous results discrepancies of up to 7.7 standard deviations were found. These were investigated and could be solved. The trend of the two-neutron separation energy was investigated in the context of neighboring elements. A general smooth behaviour was found showing no evidence for drastic nuclear structure effects. The comparison with nuclear charge radii and the absence of isomeric states show no fingerprint of shape co-existence. These mass measurements were only possible through the installation of the novel gas-filled linear radiofrequency (RFQ) trap. For ISOLTRAP, a prototype of such an RFQ was developed, installed and tested within this work. For the SHIPTRAP experiment, which is coupled to the Wien filter SHIP at GSI/Darmstadt, another RFQ was built and first transmission experiments were carried out. With the SHIPTRAP experiment radioactive secondary beams with MeV/u energies will be stopped, cooled and investigated in an ion trap facility. Candidates for first mass measurements of transuranium nuclei with SHIPTRAP were investigated.

Contents

Chapter 1

Introduction

One of the most fundamental properties of an atom is its mass. The mass reflects the nuclear and atomic binding energy and governs all possible interactions of the constituents of the nucleus with each other.

About 2500 different nuclides are presently known, but the masses of only about 1600 of them are experimentally determined. The ones where no experimental access was reached so far are short-lived exotic nuclides, which do not exist in nature. They are found at the borders of the chart of nuclides, further away from the valley of stability, or at the top of the chart of nuclides, which is still expanding.

The masses of the exotic nuclides are particularly important for nuclear physics. The forces that act inside the nucleus are not completely understood and no nuclear model exists that reproduces in a satisfactory way the properties of the nuclides. The mass of a nuclide depends on all nuclear interactions. Therefore, systematic mass measurements can help to broaden our knowledge on the acting forces. The nuclear shell structure, for example, is well established, but recent investigations showed hints of softening, e.g., at the magic number $N = 28$ [Zar00]. Nuclear binding energies are very sensitive to the existence of shells and can therefore provide clear signature of shell or sub-shell closure. Their measurements allow one to check whether the nuclear model holds true even at the borders of the chart of nuclides further away from β-stability.

Experimental data on masses are important for the development or improvement of nuclear-mass models. These models are used to predict the properties of nuclides, where experimental access is not possible (yet). In nuclear astrophysics the masses of the nuclides play an important role. For example in the r-process, one of the processes building the heaviest elements in the universe, the masses of the nuclides and hence the nuclear binding energy is essential to determine the path of the r-process. Herewith a better understanding of the abundance of the elements in our galaxy can be reached. However, the nuclear mass models have tremendous

variations between each other, making an objective choice difficult. Therefore it is necessary to determine the predictive power of those models by comparison with experimental results. For all these reasons mass measurements of exotic nuclides are important.

In the work presented here, two facilities are presented, the ISOLTRAP and the SHIPTRAP set-ups, where direct mass measurements on exotic nuclides are or will become possible.

The ISOLTRAP experiment is located at the on-line separator facility ISOLDE/ CERN in Geneva. The direct mass measurements are carried out with a Penning trap mass spectrometer. The necessary manipulation include cooling and bunching in a linear Paul trap filled with buffer gas and mass-selective cooling in a Penning trap.

The SHIPTRAP experiment is located behind the in-flight facility SHIP at GSI/ Darmstadt, which is a separator of the Wien filter typ. The mass measurements will be performed also with a Penning trap spectrometer. Due to the difference between those two production modes for the exotic nuclides, the required preparation for the mass measurement is naturally different. However, the cooling and bunching in a linear Paul trap are common features of the two experiments.

Such linear Paul traps or radiofrequency quadrupole (RFQ) structures allow one to accept and manipulate an ion beam, independent of its chemical or physical properties, which is in contrast for example to the previously used method of implanting the beam into a foil and subsequent evaporating out and re-ionizing the nuclides of interest.

Within this work an RFQ structure filled with buffer gas was designed, built and installed at the ISOLTRAP experiment. This work reports on the first tests of this novel instrumentation. Another gas-filled RFQ structure was designed and built for the SHIPTRAP experiment, based on the previously gained experiences.

The principles of the productions and separations of exotic nuclides is presented. The basic idea of mass measurements with Penning traps is explained together with the technique of mass selective buffer gas cooling. A larger fraction of this work is dedicated to linear Paul traps filled with buffer gas. Here the principle is explained together with the realization of the two devices, which were brought into operation.

In the second part of this work, the chapters 5 and 6, the two experiments are described in detail. For SHIPTRAP a survey is carried out on first possible mass measurements with this facility. The emphasis of the study focuses on the trans-uranium region, since the one feature of SHIP, which distinguishes it from

any facility, is the production of those nuclides. It is investigated on which nuclides direct mass measurements can be performed, and which precision can be reached taking expected production yields and performance of the SHIPTRAP facility into consideration.

The implementation of the RFQ structure for ISOLTRAP allowed one for the first time to carry out direct mass measurements on an isotopic chain of noble gases. The neutron-deficient xenon isotopes $^{114-123}$Xe were measured, where the masses of the isotopes $^{114-116}$Xe were previously not determined experimentally. The results are compared with masses predicted by various mass models and mass formulae.

Chapter 2

Production and separation of exotic nuclides

A prerequisite for mass measurements of exotic nuclides is the production and separation of those. Different processes exist that can be employed for the creation of exotic nuclides: fission, spallation, projectile fragmentation, fusion and nuclear transfer reactions. In all these production mechanisms not only one specific isotope is produced, but also other nuclides which behave then as contaminants. For the investigation of single species these unwanted nuclides have to be removed, particularly if they are produced predominantly. A brief introduction to the different currently applied production and separation methods is given in the following. A general overview can be found in [Gei95].

2.1 The ISOL method

The ISOL (Isotope Separation On-Line) method is a widely applied technique for the production and separation of exotic nuclides. A typical representative is the ISOLDE facility at CERN/Geneva.

For the production of exotic nuclides via the ISOL method an ion or proton beam with typically $100\,MeV$ to $1GeV$ kinetic energy and intensities in the μA-range is impinged on a thick target (up to $100\,g/cm^2$). Via proton induced spallation and fission various nuclides are produced and thermalized by interaction with the surrounding target material. The target container is heated to $1000 - 2000K$. The products are evaporated out and diffuse into an ion source. Here singly-charged ions are created. Electric fields are used to accelerate the ions up to typically 60 keV which allows one to send them through a magnet where isotopic separation takes place.

The production rate of a nuclide inside the target matrix is given by the primary

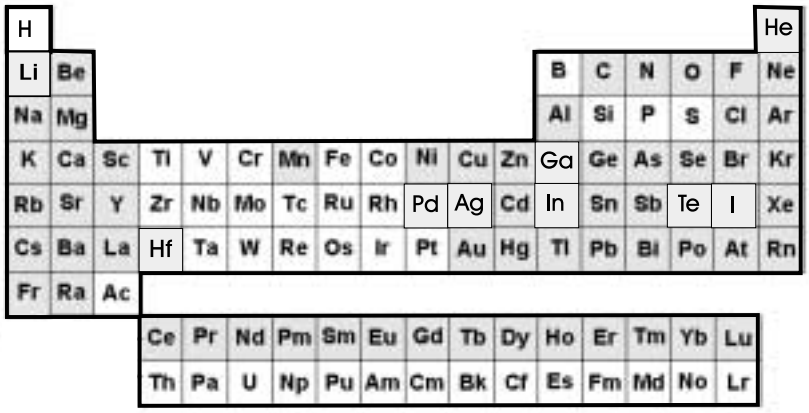

Figure 2.1: Table of elements showing those elements (gray boxes) which can be produced at the ISOLDE facility at CERN/Geneva. Taken from [Let97].

beam intensity, the target thickness and the production cross section. However, the intensity of the ion beam of exotic nuclides depends additionally on the efficiencies of the diffusion, desorption and ionization processes, and, particularly for short-lived exotic nuclides, on the period of time these processes require. In order to obtain clean beams of the isotopes of one element only, special target ion-source combinations are developed. A suppression of isobaric contaminants is possible for example by element-specific ionization like resonant laser ionization or by operating the source with a cold transfer line between target and plasma ion source where the absorption of volatile contaminants is enhanced.

The chemical properties and the nuclear half-life are crucial factors for the applicability of this method to produce, separate and deliver exotic nuclides. These are the reasons why some nuclides can be produced and delivered in a clean and sufficient way and others not at all. Figure 2.1 shows the table of elements where underlayed in gray are the elements of which isotopes can be produced and delivered at ISOLDE/CERN [Let97].

2.2 The in-flight method

The in-flight method is an alternative method for the production and separation of exotic nuclides. A facility where this is applied is the Separator for Heavy Ion Products (SHIP) at GSI/Darmstadt.

The production beam is an ion beam at high energies, typically few MeV/u to GeV/u. It is impinged on a thin target, ranging from mg/cm^2 to a few g/cm^2, but

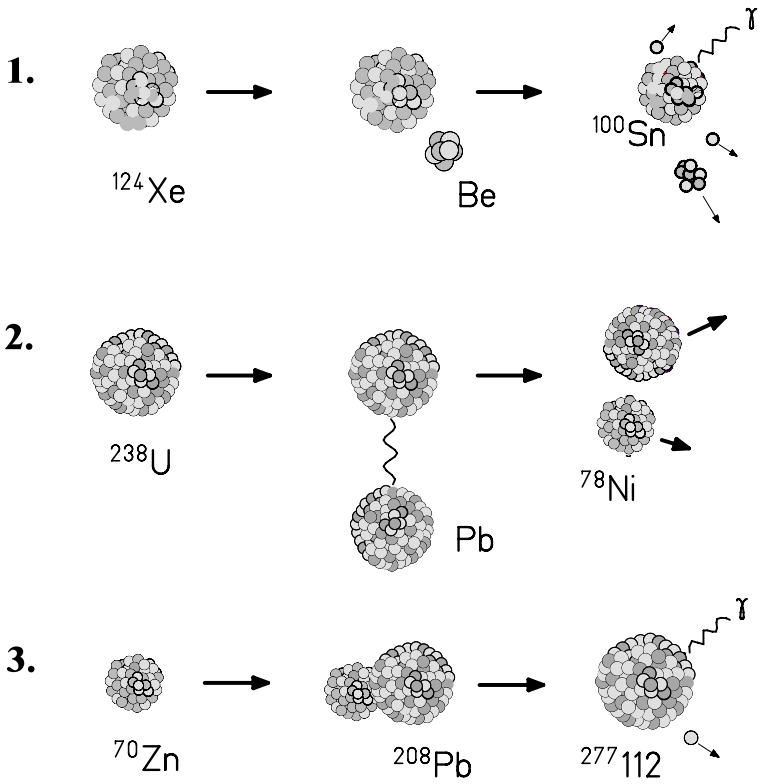

Figure 2.2: Production schemes of exotic nuclides. 1. Projectile fragmentation 2. Electromagnetic dissociation 3. Fusion reaction.

not stopped within the target material as in the ISOL method. The beam traverses the target and remains at about 80% of its original energy. Reactions mechanisms are here: projectile fragmentation, fission, electromagnetic dissociation, transfer reactions and cold or hot fusion.

In the use of high energies and low-Z target projectile fragmentation is the dominant process, where the impinging particles lose some of their nucleons or break up in a peripheral collision with target atoms. In the process of electromagnetic dissociation the traversing particle is excited by interactions with target atoms leading to evaporation of nucleons or to induced fission. For lower energies, near the Coulomb barrier, a compound nucleus can be formed in a fusion reaction. The compound nucleus evaporates off nucleons until it reaches a more stable configuration. Figure 2.2 shows a schematic of examples of these reactions. For all processes the products are highly charged, after the interaction with the target and have high energies. Secondary beam energies range from few keV/u to GeV/u.

A combination of electric and magnetic fields is used for in-flight separators (for highest energies only magnetic fields). The advantage of this method is the fast

production and separation time, which is basically the transit time through the ion-optical system. Typical flight times are on the order of microseconds.

For the production rates the target thickness, the primary beam intensity and the production cross sections have to be considered. A disadvantage is the fact that the primary beam intensities are usually lower compared to the ISOL method. This is due to the comparably thin targets, which have to be used: the atomic energy loss of the primary beam has to be on the same order as the energy window for the production process for a given reaction. For thicker targets the ratio of heat dissipation to energy absorption is lower, therefore the target would melt at higher beam currents. For the new generation of in-flight facilities special attention has to be put in a new target technology in order to circumvent this problem. However, the clear advantage of this method is that all isotopes of the chart of nuclides can be produced in principle. For example, transuranium nuclides can be generated, which are entirely inaccessible at on-line facilities.

In the scope of this work, two experiments are described where one is installed at the on-line facility ISOLDE, namely ISOLTRAP, and the other at the in-flight facility SHIP, namely SHIPTRAP. Due to the different production mechanisms and hence different secondary beam energies, specialized techniques for the preparation of the ion beam for experiments in traps have to be utilized. The basic ideas are, however, for both experiments very similar and are explained in the following.

Chapter 3

Penning trap techniques

In this chapter a short introduction to Penning trap techniques is given. The principle is explained of confining a charged particle in a Penning trap by a superposition of a magnetic and an electric field. The storage and necessary preparation for precision experiments is described as well as two methods to determine the masses of the stored particles. More detailed descriptions are given in [Bro86, Bol89, Kre91].

3.1 Theory of Penning traps

Charged particles with mass m and charge q are stored in a Penning trap by the combination of a strong homogeneous magnetic field and a static electric field. The Lorentz force generates a radial confinement and with only a magnetic field B the particles perform a circular motion perpendicular to the magnetic field lines with the true cyclotron frequency

$$\omega_c = \frac{q}{m} \cdot B. \tag{3.1}$$

An electrostatic potential is applied, confining the charged particles in the direction parallel to the magnetic field lines. This is realized by a DC-voltage U_0 between the ring electrode (see fig.3.1) and the end caps, acting as the source of a repulsive force along the magnetic field lines towards the trap center. An harmonic potential is most suited for the application presented here. Such a potential is a quadrupole potential, which is given in radial (ρ) and axial (z) components by

$$U(\rho, z) = \frac{U_o}{4d^2}(2z^2 - \rho^2). \tag{3.2}$$

The quadrupole potential has hyperbolic equipotential lines and is realized by using electrodes of this form. Figure 3.1 shows the geometry, where ρ is the radial and z the longitudinal distance from the trap center to the electrodes. In general the parameter

$$d = \sqrt{\frac{1}{2}(z^2 + \frac{\rho^2}{2})} \tag{3.3}$$

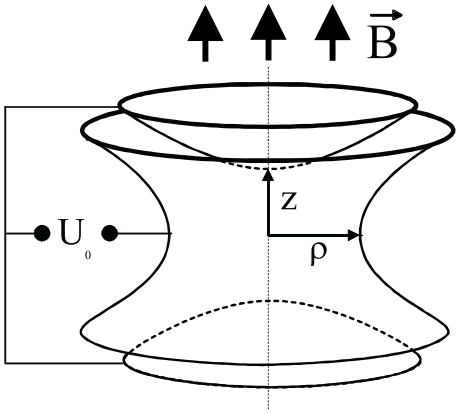

Figure 3.1: Scheme of a Penning trap. The electrodes (two end caps and one ring electrode) have hyperbolic shape.

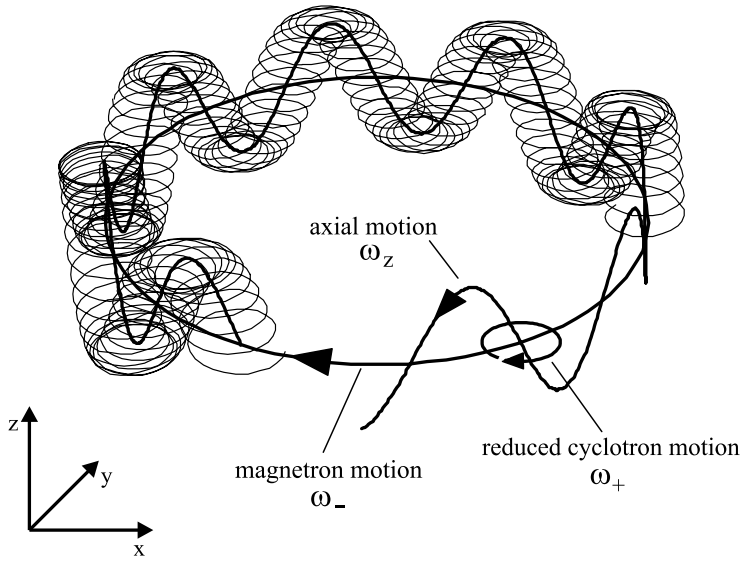

Figure 3.2: Motion of a charged particle in a Penning trap.

is used as a characteristic dimension of a Penning trap.
The force resulting from the superposition of electric and magnetic fields is given by

$$\vec{F} = -q \cdot (\vec{E} + \vec{v} \times \vec{B}) \,. \tag{3.4}$$

The equations of motion can be derived by $\vec{F} = m \cdot \vec{a}$. The solutions are three independent harmonic oscillations. In the axial direction the characteristic eigen frequency is

$$\omega_z = \sqrt{\frac{qU_0}{md^2}} \,. \tag{3.5}$$

In the radial directions the motion of the particle is a superposition of two circular motions, which are due to the combination of electric and magnetic fields. From the $\vec{E} \times \vec{B}$ term in (3.4) the so-called magnetron motion results with frequency ω_-. The cyclotron motion in a pure magnetic field is modified in a Penning trap due to the effect of the electric field and the resulting frequency is ω_+. This motion is called reduced or modified cyclotron motion. The two frequencies are related to the true cyclotron frequency via

$$\omega_c = \omega_+ + \omega_-, \tag{3.6}$$

and the radial frequencies are given by

$$\omega_\pm = \frac{1}{2}(\omega_c \pm \sqrt{\omega_c^2 - 2\omega_z^2}). \tag{3.7}$$

The stability condition for the trapping can be deduced from this equation. Since the square-root term has to be positive for stable trajectories, the condition $\omega_c^2 - 2\omega_z^2 > 0$ has to be fulfilled. Figure 3.2 shows the motion of a charged particle in a Penning trap. The three eigen motions are indicated. Typical values for the frequencies $\nu = \omega/2\pi$ of a single positively charged particle are shown in table 3.1 for conditions at the ISOLTRAP precision trap.

Table 3.1: Frequencies of the eigen motions in a Penning trap for a proton and an ion with mass $M = 100\,amu$. The frequencies are typical for ISOLTRAP with a magnetic field of $B = 6\,T$, a trap size of $d = 10\,mm$ and a potential of $U_0 = +10V$.

frequency	proton	ion ($M = 100\,amu$)
ν_c	$100\,MHz$	$1\,MHz$
ν_z	$500\,kHz$	$50\,kHz$
ν_-	$1\,kHz$	$1\,kHz$

3.2 Mass measurements with Penning traps

In the following two methods are described to determine the mass of charged particles stored in a Penning trap. The first is the so-called time-of-flight (TOF) measurement, which is applied at the ISOLTRAP experiment and the second is called Fourier Transform-Mass Spectrometry (FT-MS) or Fourier Transform-Ion Cyclotron Resonance (FT-ICR). The latter is foreseen for measurements at SHIPTRAP on ions with very small production rates.

3.2.1 Time-of-Flight mass measurement

For TOF measurements the charged particles have to be prepared in the Penning trap. This is done by an electric quadrupole excitation with the field components

$$\begin{aligned} E_x &= E_0 \times y \times cos(\omega_0 t) \\ E_y &= E_0 \times x \times cos(\omega_0 t)\,. \end{aligned} \tag{3.8}$$

This leads to a coupling of the magnetron and cyclotron motion [Bol89]. A periodic energy conversion from one motion into the other takes place, if the resonance frequency $\omega_0 = \omega_+ + \omega_- = \omega_c$ is applied. The time for such a conversion is given by

$$T_{\omega_- \to \omega_+} = \frac{\pi \cdot (\omega_+ - \omega_-)}{r_0} \tag{3.9}$$

with

$$r_0 = \frac{q}{m} \cdot E_0. \tag{3.10}$$

The radii of the magnetron or, respectively, cyclotron motion are identical after a conversion. The conversion is complete if the time of excitation is $n \cdot T_{\omega_- \to \omega_+}$. For non-integers the final state is a mixed form of magnetron and cyclotron motions. The required quadrupole field is realized for a Penning trap by applying quadrupolar RF-potentials to a four-split ring electrode. If initially the ions have been prepared in a pure magnetron motion, the radial energy E_r increases during the process of conversion from the slow magnetron motion to a fast cyclotron motion with much higher radial energy E_r.

For the TOF measurement the charged particles are released from the trap after their excitation. Static electric fields accelerate the particles through the inhomogeneous part of the magnetic field onto a detector. The time between releasing the particles from the trap to detecting a signal on the detector is the time of flight. A schematic is shown in fig.3.3.

The magnetic moment of an ion orbiting in a magnetic field is given by

$$\vec{\mu} = (\frac{E_r}{B})\vec{e_z}\,, \tag{3.11}$$

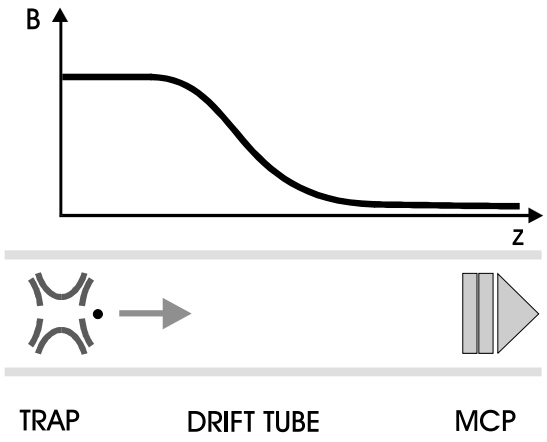

Figure 3.3: Schematic of the TOF measurement. The ions are released from the trap and drift through the inhomogeneous magnetic field to the micro channel plate (MCP) detector.

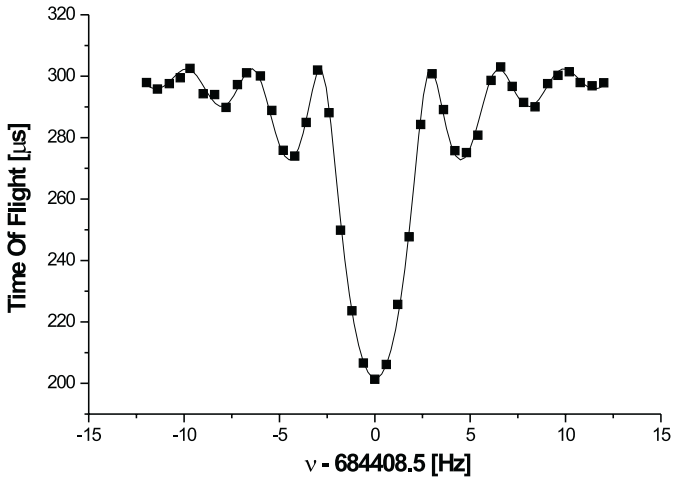

Figure 3.4: Cyclotron resonance for ^{133}Cs ions. The continuous line is the theoretically expected shape [Koe95b] of the resonance fitted to the data points.

where E_r is the radial energy. While drifting out of the magnet through the part of the magnetic field where a gradient exists, the magnetic moment interacts with this gradient and the resulting force in z-direction is

$$F_z = -\nabla(\mu \cdot B\,). \tag{3.12}$$

Due to this force, radial energy is converted into longitudinal energy [Grä80, Kre91]. Therefore, the ions with high radial energy reach the detector faster than ions with low radial energy. This is the case for a resonant excitation at ω_c, converting the initially (low) magnetron energy into (high) cyclotron energy. Hence the TOF can be used as a measure whether the mass-dependent frequency for the preparation was found or not. By measuring the TOF as a function of applied rf, the cyclotron frequency of the ions under investigation is determined. The mass of this ion is obtained via (3.1) where the magnetic field B is determined in a reference measurement on ions of well-known mass. Figure 3.4 shows the time of flight as a function of applied quadrupole excitation frequency for singly charged ^{133}Cs ions, together with the theoretically expected shape of the resonance [Koe95b]. The total number of detected ions for such a measurement of exotic nuclides is typically about 3000.

3.2.2 Fourier Transform-Mass Spectrometry

A different method of determining the mass of charged particles in a Penning trap is the non-destructive Fourier Transform-Mass Spectrometry (FT-MS). This is a standard method for chemical applications. A general overview is given in [Gua95, Com86].

For the FT-MS the particles are excited by an RF dipole field at their modified cyclotron frequency. In commercial instruments, the ions are generally confined in a cubic box, where two electrodes are used as end-caps and four electrodes as ring electrodes. A schematic is shown in fig.3.5. Two opposite electrodes of the 'ring electrode' are used to excite the ions, the other to observe the image current. Due to their motion the charged particles induce an image AC-current on the segmented electrodes. The axial motion also generates a current on the outer electrodes with a characteristic frequency. The induced currents are read out via a low-noise amplifier and are Fourier transformed. In this way, the frequencies ω_+ and ω_z can be directly measured. The invariance theorem [Bro86]

$$\omega_c^2 = \omega_+^2 + \omega_-^2 + \omega_z^2 \tag{3.13}$$

and

$$\omega_- \approx \frac{\omega_z^2}{2\omega_+} \tag{3.14}$$

relate these two frequencies then to the mass of the particle. Reference measurements with particles of well-known mass make relative experiments possible, so the

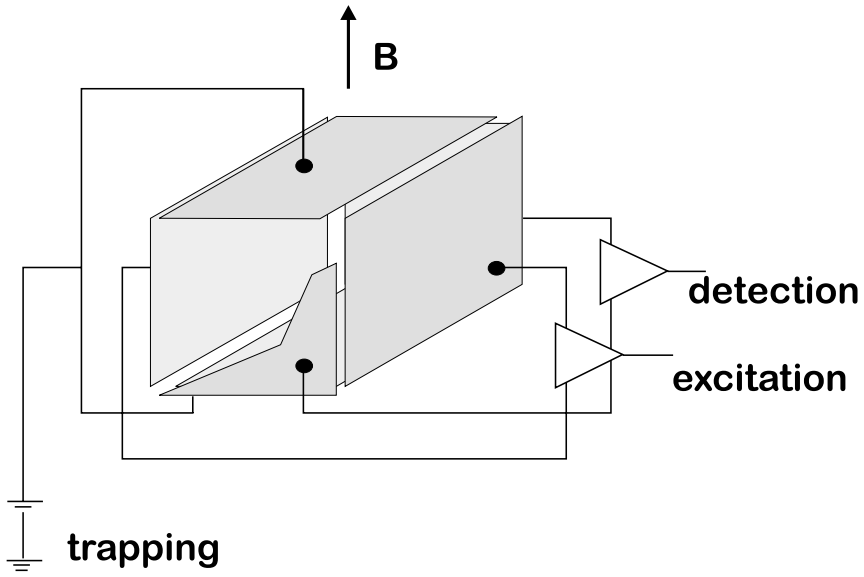

Figure 3.5: Principle of Fourier Transform-Mass Spectrometry in a cubic ion trap. Connections for trapping, dipolar excitation and detection are shown.

magnetic field cancels out. Employing this technique, the mass of charged particle can be measured non-destructively. However, the sensitivity for such a system is rather low, and a few hundred ions are in general necessary to achieve detectable signals. The resolution that is reached with these FT-MS devices is limited therefore by Coulomb interaction effects due to the large amount of simultaneously stored ions [Bol92]. Another limitation arises from the fact that no electric quadrupol potential is employed and the resonance frequency ω_c is then only an approximation of $q/m \cdot B$ (see (3.2)).

Single ion detection

For the detection of small induced currents, for example for few or single ions it is necessary to enhance the signal by use of a resonance circuit of high quality factor Q. This is done by coupling the low noise amplifier via a parallel inductance L to the pick-up electrodes. Together with the capacity C of the the trap electrodes a resonance circuit is formed. Choosing the components such that $\omega_+ = \omega_{LC} = 1/\sqrt{LC}$, the circuit can be operated in resonance frequency. In this way, a high amplification can be reached. However, the disadvantage in such a scheme is, that only one specific frequency or isotope can be measured (depending on the resonance width of the circuit). This can be overcome by employing a tunable circuit, where the resonance frequency can be shifted by changing the parameters of the electronic components. A schematic of such a system with hyperbolic electrodes is shown in fig.3.6.

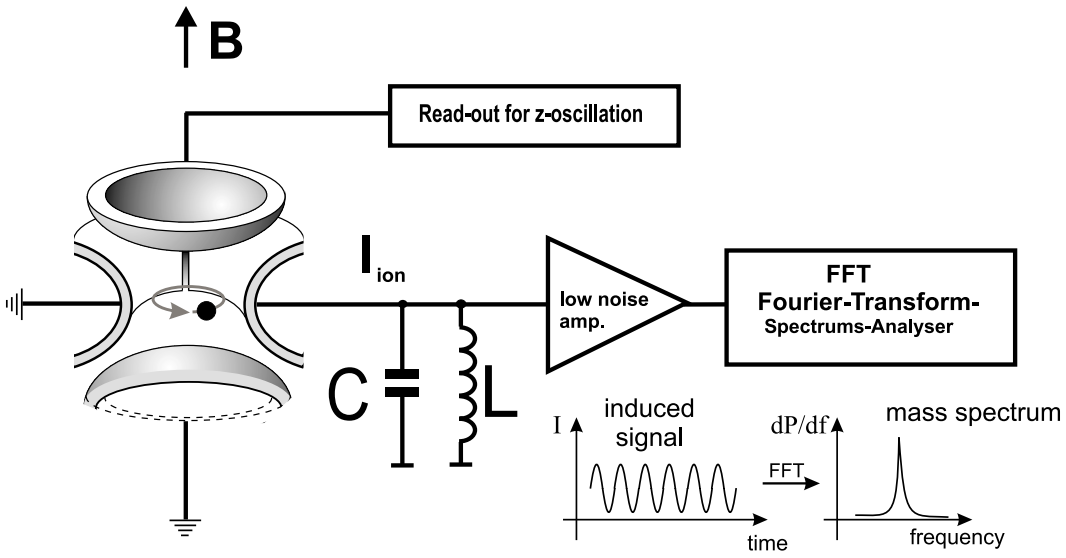

Figure 3.6: Schematic of Fourier Transform-Mass Spectrometry with a tuned circuit for single ions. The particles excited by rf in the Penning trap induce image currents on the segmented ring electrodes and the end caps, which is read out and Fourier transformed.

Expected signal

The expected signal S for one ion with charge state q is

$$S = U_{induced} = I_{ion} \cdot R\,, \tag{3.15}$$

where in the resonance case

$$R = \frac{Q_{LC}}{\omega} \cdot C\,. \tag{3.16}$$

ω is the cyclotron frequency, C the capacity and Q_{LC} the quality factor of the LC-circuit which is defined by $Q_{LC} = \omega/\Delta\omega_{FWHM}$. The induced current can be calculated to [Sta98]

$$I_{ion} = \frac{1}{\sqrt{2}} \cdot \frac{r}{\rho} \cdot q \cdot \omega, \tag{3.17}$$

where r is the radius of the orbiting ion, q its charge state and ρ is the size of the trap which is used to pick up the image currents. The signal is given as

$$S = \frac{1}{\sqrt{2}} \cdot \frac{r}{\rho} \cdot \frac{q}{C} \cdot Q_{LC}. \tag{3.18}$$

The signal increases with the amplitude of the ion motion and with a smaller trap geometry. It also scales linearly with the charge of the stored ions.

Table 3.2: Comparison of the induced current I, signal S and signal-to-noise ratio S/N for different numbers of stored ions, absolute temperatures T and quality factors Q_{LC} of the used detection circuit. Parameters are typical for the SHIPTRAP set-up (see text).

Ions	T [K]	Q	I [pA]	S [μV]	S/N
1	293	50	0.01	0.07	0.88
10	293	50	0.12	0.71	8.82
100	293	50	1.22	7.12	88.25
100	77	50	1.22	7.12	172.14
100	77	250	1.22	35.44	384.92
1	4	250	0.01	0.35	16.89
100	4	250	1.22	35.44	1688.81

For singly-charged ions and small numbers of trapped ions, the thermal noise of the resonance circuit has to be considered (Johnson noise). This white noise is given by [Hor91]

$$N = \sqrt{4\,kT \cdot R \cdot \delta f}, \tag{3.19}$$

which is the voltage generated by a resistor R depending on the absolute temperature T, the Boltzmann's constant k, and the bandwidth δf of the actual signal to be measured. The latter one can be taken from the linewidth $V = \delta f/f$. The signal-to-noise (S/N) ratio is

$$\frac{S}{N} = \frac{\sqrt{\pi}}{2} \cdot \frac{r}{\rho} \cdot q \cdot \frac{1}{\sqrt{V}} \cdot \sqrt{\frac{Q_{LC}}{kT \cdot C}}\,. \tag{3.20}$$

An estimation for the expected current, voltage and signal-to-noise ratio can be carried out. Let's assume a system that could be employed at SHIPTRAP for measurements on stored ions with mass $M = 250\,amu$. Parameters are: magnetic field $B = 7\,T$, electric field $U_0 = 10\,V$, trap diameter $\rho = 32\,mm$, ion magnetron radius $r = 8\,mm$, cyclotron frequency $\omega_c/2\pi = 420\,kHz$, capacity $C = 20\,pF$, inductance (for resonance case) $L = 7.2\,mH$ and resistor $R = 900\,k\Omega$. These are typical values for such circuits. Table 3.2 shows the expected values for different conditions of the detection scheme. The S/N-ratio for a single ion at room temperature for a circuit quality factor of $Q_{LC} = 50$ is $S/N = 0.88$ and therefore hardly detectable. However, by increasing the number of ions stored simultaneously this detection becomes feasible. Going to a cooled system, the noise is significantly reduced and the S/N-ratio increases by a factor of about 20 for a system at liquid helium temperature.

The cooled system has two clear advantages: the noise is reduced and super conducting coils can be employed, resulting in a higher Q_{LC}-factor. However, this

demands a cryogenic version of the trap and the electronics at $T = 4\,K$. Technically, this is more difficult than a room temperature system, but was already realized, for example for Penning trap experiments on stable particles [VDy87, NHe00, Bra99], or for a Penning trap for the proton/antiproton mass comparison, coupled to an accelerator facility, where the particles of interest had to be produced externally [Gab95].

The expected bandwidth of the cyclotron resonance was taken to be $\delta f/f = 1 \cdot 10^{-6}$ for this calculation, based on the fact that it is dominated by the fluctuations of the magnetic field itself. The resonance frequency is given by $\omega_c = q/m \cdot B$. Therefore $\delta B/B$ couples directly to the frequency. For the SHIPTRAP system the magnet specifications are given by $\delta B/B \leq 1 \times 10^{-8}$ per hour. So the bandwidth used here is a conservative approximation.

3.2.3 Comparison between TOF and FT mass spectrometry in a Penning trap

For precision mass measurements both techniques can be applied. The resolution of the TOF and the FT-MS measurements is given by the Fourier limit of the excitation or observation time T_{RF}, which is [Koe95b]

$$\Delta\nu_{FWHM} \approx \frac{0.95}{T_{RF}}. \tag{3.21}$$

For example for an ion of mass $M = 250\,amu$ the resolution would be for $T_{RF} = 0.5\,s$ in the above set-up

$$\Delta\nu_{FWHM} \approx \frac{0.95}{0.5\,s} = 1.9\,Hz \Rightarrow \frac{\Delta\nu_{FWHM}}{\nu} = \frac{1.9\,Hz}{420\,kHz} = 4.5 \times 10^{-6}. \tag{3.22}$$

However, for the FT-MS the required number of ions is lower than for the TOF method for a mass measurement. For TOF-MS, the minimum number of detected ions is a few hundred. The requirements for FT-MS would be only 1-100 ions to reach reasonable precision. For a system operating at liquid He temperature, a single measurement on a single ion would allow mass measurements within an accuracy well below 10^{-6}. Technically more demanding is the cryo-technique for the electronics and the trap itself that has to be applied to get single-ion spectra, where for example for 100 ions at room temperature with standard coils ($Q_{LC} = 50$) sufficient signal-to-noise ratios can be achieved.

For applications at SHIPTRAP for ions with very small production rates, only the FT-MS at liquid-helium temperature seems possible. The ions delivered by SHIP and accumulated in the RFQ linear trap (see below) would be stored in the trap and an RF-excitation would be performed. In this way a non-destructive FT-MS on a single ion can be carried out.

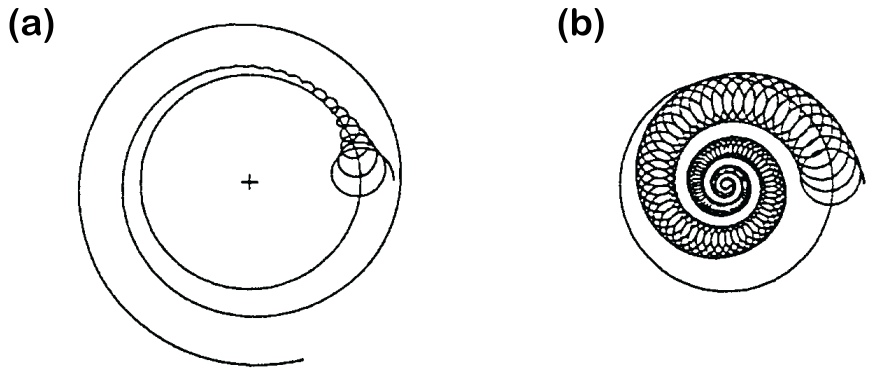

Figure 3.7: Motion of a charged particle in a Penning trap in the azimuthal plane in buffer gas. The central cross defines the center of the trap and the circle the initial magnetron orbit. (a): fast cooling of the cyclotron motion and slow increase in magnetron amplitude. (b): additional RF-excitation at ω_c; the net effect is a cooling of both motions and a centering. Taken from [Sav91].

3.3 Mass-selective buffer gas cooling in a Penning trap

A necessary prerequisite for precision mass measurements is the preparation of an isobarically clean sample. This can be accomplished by mass-selective buffer gas cooling [Sav91, Koe95b]. The ions are loaded into a Penning trap where buffer gas at a moderate pressure is present, typically around $p = 4 \times 10^{-6}\, mbar$. Noble gases are used to minimize charge exchange processes. The interaction of the stored ions with the buffer gas is mainly due to an interaction with the induced dipole moments of the buffer gas atoms or molecules, and not due to an elastic scattering process on a hard sphere [Ell78]. Therefore, the cooling of the ion is based on the collisions with buffer gas particles and can be described by a viscous-drag model. Such a behaviour is well approximated by a damping force proportional to velocity

$$\vec{F} = -\delta \cdot m \cdot \vec{v}\,, \tag{3.23}$$

with the damping coefficient

$$\delta = \frac{q}{m \cdot k_0} \cdot \frac{p_{norm}}{T_{norm}}\,. \tag{3.24}$$

Here, k_0 is the ion mobility which is tabulated for various combinations for ions in buffer gas in [Ell78], p_{norm} is the pressure with respect to standard pressure p_N, and T_{norm} is the corresponding normalized temperature. Including this term in the equation of motion of the ions the amplitudes of the three eigen motions can be

expressed as a function of time

$$\begin{aligned} A_+(t) &= A_+(0) \cdot e^{-\alpha_+ \cdot t} \\ A_-(t) &= A_-(0) \cdot e^{+\alpha_- \cdot t} \\ A_z(t) &= A_z(0) \cdot e^{-\alpha_z \cdot t} \end{aligned} \tag{3.25}$$

with

$$\alpha_\pm = \delta \frac{\omega_\pm}{\omega_+ - \omega_-} \quad \text{and} \quad \alpha_z = \frac{\delta}{2}\,, \tag{3.26}$$

where $A_i(0)$ describes the initial amplitudes in the different motions. The amplitudes of the reduced cyclotron motion ($A_+(t)$) and of the axial motion ($A_z(t)$) decay exponentially, while the one for the magnetron motion ($A_-(t)$) grows with time. Hence the ions are lost, once the amplitude is larger than the size of the trap electrodes. This can be overcome by applying an additional electric radiofrequency quadrupole field at the frequency

$$\omega_{RF} = \omega_c = \omega_+ + \omega_- = \frac{q}{m} \cdot B\,. \tag{3.27}$$

A coupling of both motions, the magnetron and the reduced cyclotron motion, sets in and, for example, for an ion with initially only magnetron motion this coupling leads to a complete conversion into cyclotron motion. The amplitude of this motion is continuously cooled by the damping force of the buffer gas. The net result of buffer gas damping and simultaneous RF-excitation is a cooling and centering of the ion cloud. Additionally, this process is isotope selective since the RF-resonance frequency directly depends on the mass of the ions.

Figure 3.7 shows a simulation of the motion of a charged particle in the azimuthal plane of a Penning trap. On the left side the buffer gas affects the cyclotron motion and leads to a fast damping of the amplitude while the magnetron orbit increases slowly. The particle is finally lost by hitting the trap electrode. On the right side, an additional quadrupole excitation at the cyclotron resonance frequency is applied. The coupling of the two motions slows down the cooling of the cyclotron motion, but reduces the magnetron amplitude. The net result is a cooling and centering of the ion motion. However, this effect requires that the conversion time from magnetron to cyclotron motion is short compared to the increase of the magnetron motion itself. This is the case if the damping coefficient δ is large compared to the conversion time $T_{\omega_- \rightarrow \omega_+}$. The conversion time (see eq. 3.9) depends on the applied amplitude of the quadrupole field. For a proper choice of those parameters a mass selective cooling to buffer gas temperature can be achieved for the radial and the axial motions. The centering allows one to selectively extract the ions through an orifice in the end cap of the Penning trap. At a given opening diameter only the ions on smaller orbits, hence the cooled and centered ones, are ejected. Two conditions for precision experiments are fulfilled with this method: the preparation of a mono-isobaric ion sample which occupies a small phase space volume.

Chapter 4

A linear gas-filled Paul trap for cooling and bunching

4.1 Theory of Paul traps

In a Paul trap the confining potential is created with oscillating electric fields, and no magnetic fields are applied. The simplest form of such a trapping field is the quadrupole field. The potential is given by

$$\phi = \frac{\phi_0}{2r_0^2}(\lambda x^2 + \sigma y^2 + \gamma z^2)\,, \tag{4.1}$$

where ϕ_0 is the applied oscillating electric potential, λ, σ and γ are constants depending on the field to be generated, and r_0 depends on the geometry. The constants have to be chosen to fulfill Laplace's equation

$$\nabla^2\phi = 0\,, \tag{4.2}$$

which requires, beside the trivial case:

$$\lambda + \sigma + \gamma = 0\,. \tag{4.3}$$

A three dimensional trapping potential for charged particles is formed by using the geometry shown in fig. 4.1, which is the same as the one used for a Penning trap but using oscillating electric fields. The potentials at the end caps and the ring electrode are on opposite phase. Such devices were initially invented by W. Paul [Pau53] and a overview is given in [Pau89]. They can be used for various applications [Gos95, Sch98, Lun92].

In the following the focus is on the two-dimensional form of the Paul trap, in general called mass filter or ion guide. A review is given in [Daw95].

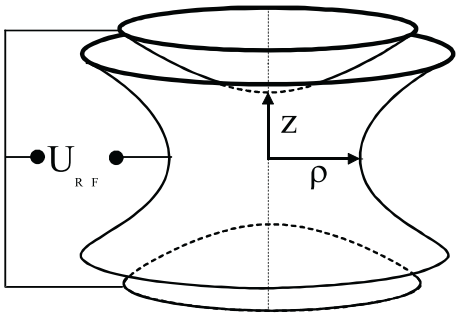

Figure 4.1: Schematic of a Paul trap. The three electrodes (two end caps and one ring electrode) have hyperbolic shape. Radiofrequency is applied between end-caps and ring electrode.

For the two-dimensional case the coefficient in the z-direction vanishes ($\gamma = 0$). For symmetry reasons we consider $\lambda = -\sigma = 1$. The potential is given by

$$\phi(x, y) = \phi_0 \frac{x^2 - y^2}{2r_0^2} \,. \tag{4.4}$$

A realization of this device is a four-rod structure as shown in fig. 4.2, where the rods are formed to hyperbolic shape and the applied potential is $\pm\phi_0/2$. For practical reasons, the rods are often shaped cylindrical and the deviations from the ideal field generated with such a geometry are found to be minor [Day54, Den71] if a ratio of the rod radius R to the structure opening radius r_0 of

$$\frac{R}{r_0} = 1.14511 \tag{4.5}$$

is taken [Lee71]. A voltage of $\pm(U - Vcos\Omega \cdot t)/2$ is applied to the two pairs of opposite rods, where U is a DC-voltage and $Vcos\Omega \cdot t$ is the AC-voltage at the radiofrequency Ω. The potential at a time t and a point (x, y) is given by

$$\phi(x, y, t) = (U - Vcos\Omega \cdot t) \frac{x^2 - y^2}{2r_0^2} \,. \tag{4.6}$$

The equations of motion of a charged particle with mass m and charge q_e are

$$\begin{aligned} \ddot{x} + \frac{q_e}{mr_0^2}(U - Vcos\Omega \cdot t)x &= 0 \\ \ddot{y} - \frac{q_e}{mr_0^2}(U - Vcos\Omega \cdot t)y &= 0 \\ \ddot{z} &= 0 \end{aligned} \tag{4.7}$$

Obviously there is no longitudinal force and a charged particle entering the device will keep its momentum component in z-direction, but will interact radially with the

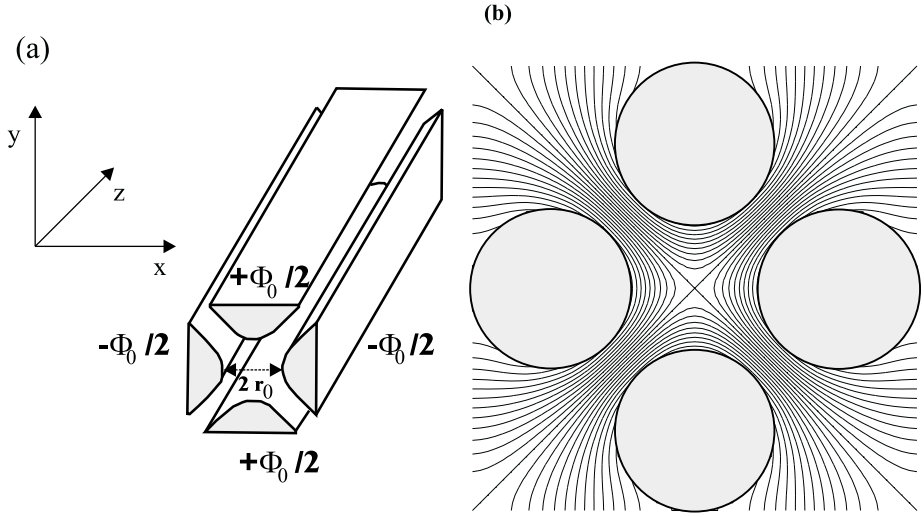

Figure 4.2: Schematic of a Paul massfilter. (a) Ideal two-dimensional Paul mass filter geometry with hyperbolic electrodes. The applied potentials are indicated. The distance between the opposite rods is $d = 2 \cdot r_0$. (b) Circular rods including equipotential lines in x/y-direction.

electric field.

The equations can be solved by introducing the stability parameters

$$a \equiv \frac{4q_eU}{mr_0^2\Omega^2} \quad ; \quad q \equiv \frac{2q_eV}{mr_0^2\Omega^2} \tag{4.8}$$

and the phase parameter

$$2\zeta \equiv \Omega \cdot t\,. \tag{4.9}$$

Two differential equations can be written

$$\begin{aligned} \frac{d^2x}{d\zeta^2} + (a - 2q \cdot cos2\zeta)x = 0 \\ \frac{d^2y}{d\zeta^2} - (a - 2q \cdot cos2\zeta)y = 0 \end{aligned} \tag{4.10}$$

or in a more general form

$$\frac{d^2u}{d\zeta^2} + (a - 2q \cdot cos(2\zeta))u = 0\,, \tag{4.11}$$

where u is substituted for x and y. This is the so-called *Mathieu differential equation.* By applying Floquet's theorem the general solution of this equation can be given as a Fourier sum of two fundamental solutions [Ars64]:

$$u(\zeta) = A \cdot e^{\mu\zeta} \sum_{n=-\infty}^{\infty} C_{2n} \cdot e^{i2n\zeta} + B \cdot e^{-\mu\zeta} \cdot \sum_{n=-\infty}^{\infty} C_{2n} \cdot e^{-i2n\zeta}\,. \tag{4.12}$$

The parameters A and B are integration constants depending on the initial conditions of the motion of the charged particle, the position u and velocity $\dot{u}$, and the initial phase of the oscillating RF-field. The constants C_{2n} and μ depend on the values of a and q in a complicated manner, but not on the initial conditions. This means that the solution of the Mathieu equation, i.e. the motion of the charged particle, depends on the stability parameters a and q. A requirement arises from the boundary conditions given by the geometry of the four-rod structure. The maximum amplitude u_{max} of the oscillating motion has to remain within the structure, hence r_0. Therefore stable solutions are found only when the term μ in the exponent stays finite for $\zeta \to \infty$. On the other hand unstable solutions are found when μ increases with $\zeta \to \infty$. With the definition of the *secular parameter* $\beta = i\mu$ the solutions can be classified into four categories:

- μ is real and $\mu \neq 0$: unstable because $e^{\mu\zeta}$ is divergent for $\zeta \to \infty$.
- $\mu = i\beta$ is imaginary and β is not an integer: solutions are stable and periodic.
- μ has a real and an imaginary part: solutions are unstable apart from the case where $u = \dot{u} = 0$.
- $\mu = i\beta$, with β is an integer: solutions are periodic but unstable. These solutions define the borders in the $a-q$-diagram between stable and unstable solutions.

However, only approximations exist for the parameter β as a function of a and q. The expression

$$\beta = \sqrt{a - \frac{(a-1)q^2}{2(a-1)^2 - q^2} - \frac{(5a-7)q^4}{32(a-1)^3(a-4)} - \frac{(9a^2+58a+29)q^6}{64(a-1)^5(a-4)(a-9)}} \quad (4.13)$$

is a good approximation for small values of the stability parameters [Car72]. In fig. 4.3 solutions of the Mathieu equation in the parameter space of a and q are shown. The areas which fulfill the criteria of stability are shaded in the graphs. In (a) the general solution is shown. From the original equation it is clear that the diagram is symmetric with respect to the a-axis. Stable solutions for the equation of motion are given for stable combination of the parameters a and q. Graph (b) shows a closer view on the stability diagram for the motion in x-direction, however stable trajectories are only those which are stable in x- and y-direction. This is depicted in fig. (c), where the stability diagram for a is mirrored on the q-axis into the $(-a)$-space. The regions of stability for a two-dimensional Paul trap are then given by the overlapping areas in the diagram. The different regimes are called first, second, etc. stability region. All other combinations of the parameters lead to a loss of the charged particle. The stability region used in general is the first one, which is the easiest to achieve experimentally and the largest in parameter space. By operating a four-rod structure with stability parameters within this regime, the charge particles

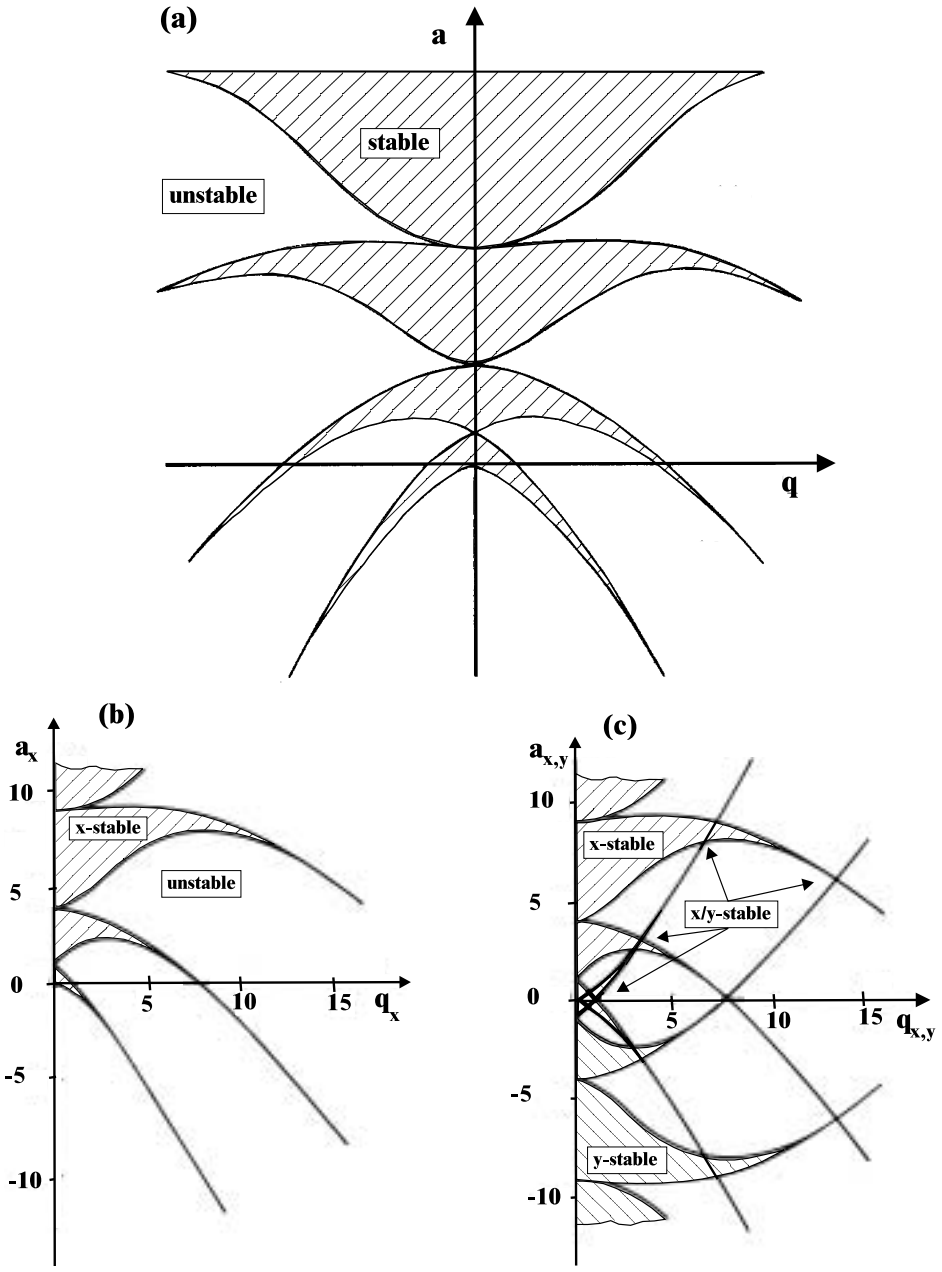

Figure 4.3: Stability diagrams of the Mathieu differential equation. (a) A stable solution for the equation of motion is given by a stable combination of the parameters a and q. The areas are shaded where that condition is true. (b) Zoomed view for the two-dimensional case, the stable x-motions are indicated. (c) Mirroring the a-diagram on the q-axis to get the y-motion stability diagram. Stable motion in x/y-direction is only in the overlapping regions. Graphs according to [Gos95].

Table 4.1: Parameters of the different graphs in fig.4.4 for the combinations of the stability parameters a and q for a four-rod structure such as the one used for SHIPTRAP, with $r_0 = 3.9\,mm$, frequency $f = 1\,MHz$ and an ion of mass $M = 133\,amu$ is assumed. The used AC-voltage is $U_{op} = 114\,V$.

figure	q-value	a-value	DC-voltage $U[V]$	comment
a	0.55	-0.162	-16.818	just outside stability
b	0.55	0	0	in the 1^{st} stability region
c	0.55	0.425	44.125	unstable (x-unstable, y-stable)
d	0.55	2.50	259.125	in 2^{nd} stability region

entering into it will be transmitted. For an a, q combination outside this area, where either only the x- or y-motion is stable or even none of them, the entering particles will hit the electrodes and will be lost. Because the $a-$ and $q-$parameter depend on the mass of the particle, such an radiofrequency quadrupole (RFQ) structure acts as a mass filter.

Examples of trajectories for different points in the stability diagram are shown in fig. 4.4. All diagrams show the radial amplitude u as a function of time t. In table 4.1 the combinations for a and q and the parameters to reach those stability values are given for the RFQ structure used at SHIPTRAP. Four cases are shown: (a) unstable motion: both amplitudes of the so-called macro and micro motion are steadily rising, the particle is therefore lost, (b) stable motion: oscillation around the center-line, (c) unstable motion, (d) stable motion.

Figure 4.5(a) displays a zoomed view of the stability diagram, showing the first stability region of an RFQ. The two nearly triangular regimes, which are symmetric with respect to the q-axis, define the area of transmitted charged particles. For fixed values of $r_0\,, \Omega\,, U$ and V, all charged particles with the same q_e/m-ratio have the same operation point in the a, q-diagram. From 4.8, it is evident that the a/q-ratio is equal to $2 \cdot U/V$ and independent of q_e/m. The operation points of all particles lie on a straight line, going through the origin of the stability diagram. This is in general called *mass scan line* [Daw95], shown in fig.4.5(b). The lower intersection of this line with the boundary line of the stability regime defines $q(low)$ and the upper intersection $q(high)$. If the slope of the mass scan line is so high that there is no intersection, all entering particles have unstable trajectories and are not transmitted. By having zero slope of the mass scan line, corresponding to $a = 0$, all ions with $q \leq 0.908$ are transmitted. $q = 0.908$ is the intersection of the stability regime with the a-axis. By choosing the slope of the mass scan line, one defines the mass resolution of the RFQ mass filter. The resolution at the peak of the stability

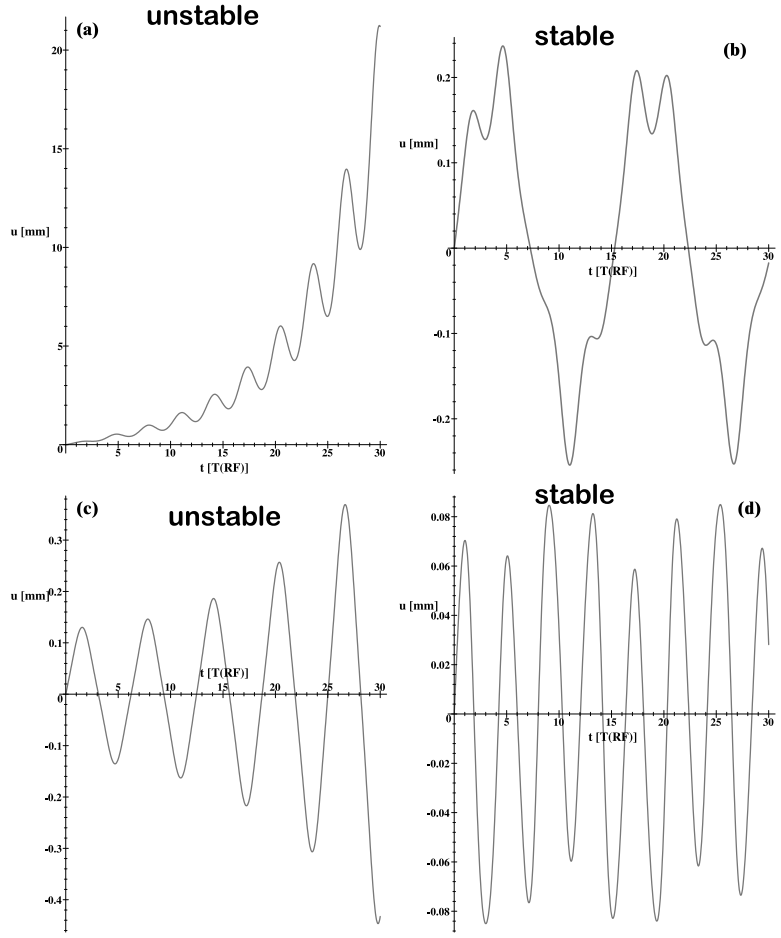

Figure 4.4: Ion trajectories as a function of time for different points in the stability diagram: (a) $q = 0.55, a = -0.1625$, (b) $q = 0.55, a = 0$, (c) $q = 0.55, a = 0.425$ and (d) $q = 0.55, a = 2.5$. For more details see table 4.1.

region is $m/\Delta m = \infty$ and for a zero slope it is $m/\Delta m = 0$ for $q \leq 0.908$. In this way, the mass filter can be operated in three modes: (1) transmission of all ions, no mass selection ($m/\Delta m = 0$), (2) transmission of ions in a range of q_e/m and (3) transmission of an ion with one specific q_e/m ratio. The three cases are shown in fig.4.5(b).

Examples of the mass filtering effect are shown in fig.4.6 and 4.7. In fig.4.6 a four-rod structure, as used for SHIPTRAP, is operated at fixed parameters. In the given example the ions with mass $M = 133\,amu$ are transmitted. For $M = 125\,amu$ the amplitudes of the trajectories increase and the ions are lost. The operating points are indicated (fig.4.6(b)). In such a case the RFQ could be employed to suppress nearby masses. Another example is shown in fig. 4.7. The ions with mass $M = 40\,amu$ have unstable trajectories, where ^{133}Cs is transmitted. The

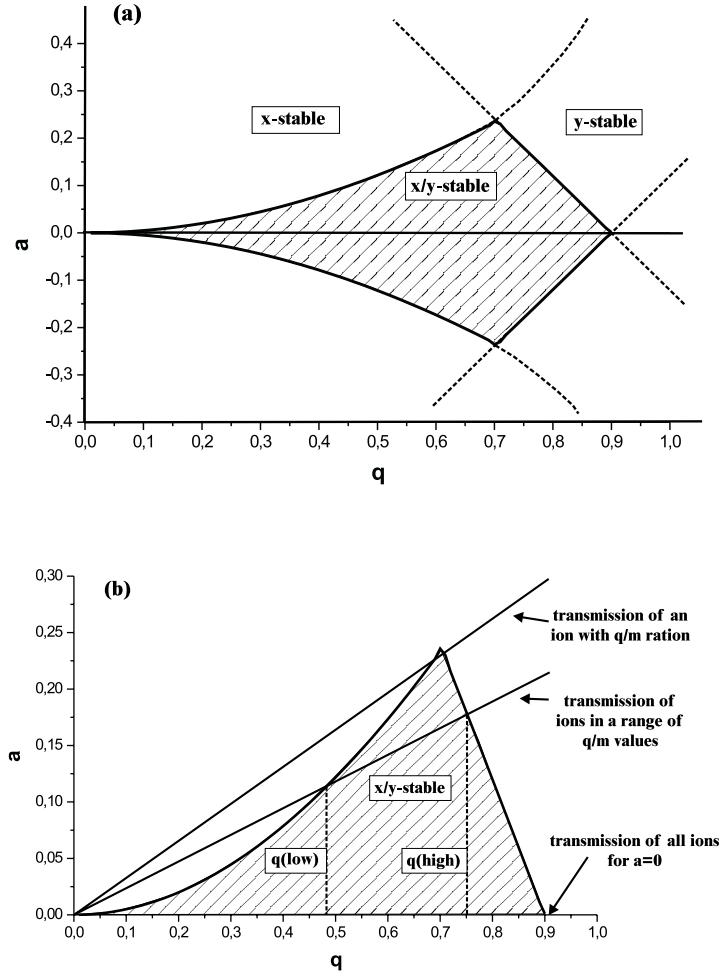

Figure 4.5: Part of the stability diagram shown in fig.4.3(c) for the solutions of the Mathieu differential equation. (a) Enlarged view of the first region of stability in x/y-direction for a two-dimensional Paul trap. The shaded area is stable in both directions. (b) First stability region with mass scan lines for operating an RFQ as a mass filter.

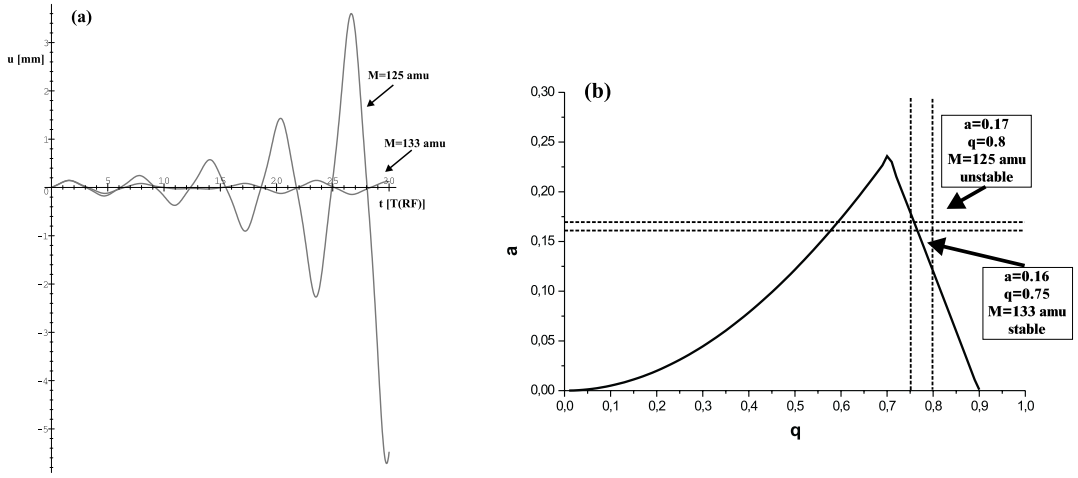

Figure 4.6: (a) Calculated trajectories of ions with different masses in the RFQ structure of SHIPTRAP, operated at stable voltages. (b) Stability diagram of the structure with working points for the two masses.

corresponding a/q-values are indicated in the stability diagram in fig. 4.7 (b). Ions of mass $M = 40\,amu$ are potentially present in the SHIPTRAP device because of ionized argon buffer gas. The mass filtering effect could therefore be utilized to remove contaminants as a preparation for precision experiments in a Penning trap.

4.2 RFQ structures as cooler and buncher

RFQ structures as described above can be used either as mass filters or in the so-called RF-only mode ($a = 0$) as an ion guide system. Transmission is maximum in this configuration. All ions with masses corresponding to stability parameters $q \leq 0.908$ have stable trajectories. These RFQ devices can be filled with a buffer gas for cooling of the injected ions.

4.2.1 The cooling process

The cooling process can be described by the interaction of an ion with buffer gas atoms or molecules via the induced dipole field. This mechanism can be depicted by the viscous-drag model as a velocity-depending repulsive force. It was shown by experimental results and by comparisons [FHer00, Sch98] with a full Monte-Carlo calculation, that such a model is appropriate for masses of ions much heavier than the buffer gas atoms at low energies ($E_{kin} \leq 10\,eV$). For cases where the ion mass and the buffer gas mass are comparable, it can be seen in Monte-Carlo simulations that the transmitted ions can be kicked out of phase with respect to the external field by single head-on collisions [Lun99]. This is the main loss mechanism and is called RF-heating. For the calculations presented here, the conditions for the viscous-drag

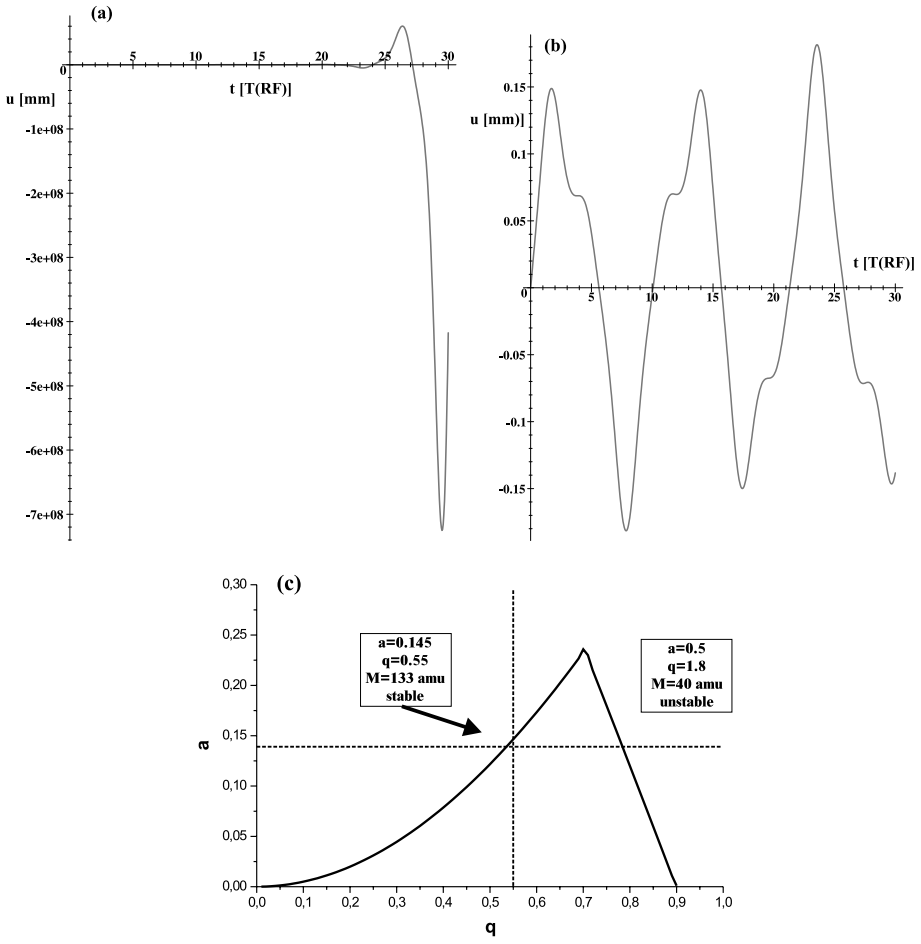

Figure 4.7: Calculated trajectories of ions with different masses in a SHIPTRAP-type RFQ structure operated at the same voltages for (a) $M = 40\,amu$ and (b) $M = 133\,amu$. (c) Stability diagram of the structure with indicated working point or a/q-parameters for the two masses. Note the different scales for the amplitude of the graphs.

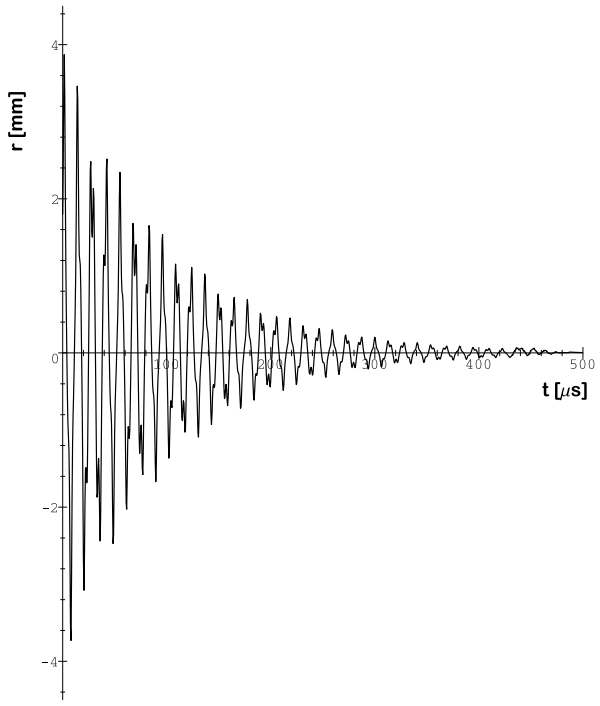

Figure 4.8: Radial amplitude of Hg^+ ions in the helium gas-filled RFQ structure for SHIPTRAP as a function of time operated at $p_{He} = 4 \cdot 10^{-2}\, mbar$. Initial kinetic energy for the calculation is $E_{kin} = 10\, eV$.

model apply. The entering ions interact with the RF-field and experience a centering force. Interactions with the buffer gas lead to an energy loss process, where after a certain time the ions reach the temperature of the buffer gas. The force due to the interaction with the buffer gas can be written as in the case of mass selective buffer gas cooling in a Penning trap (see section 2.5)

$$\vec{F} = -\delta \cdot m \cdot \vec{v}\,, \tag{4.14}$$

where m and $\vec{v}$ are the mass and the velocity of the transmitted ions. The so-called damping coefficient δ is defined as

$$\delta = \frac{q_e}{m} \cdot \frac{1}{k}\,. \tag{4.15}$$

k is the ion mobility, tabulated in [Daw95] in normalized form

$$k_0 = k \cdot \frac{p}{p_N} \cdot \frac{T_N}{T}\,, \tag{4.16}$$

with respect to standard pressure p_N and temperature T_N. The mobility is taken to be constant since it was shown in [Lun99] that only for kinetic energies below

$1eV$ non-negligible changes occur. Figure 4.8 shows a simulation of mercury ions in an one-meter long RFQ structure of the SHIPTRAP type filled with helium buffer gas. The radial amplitude as a function of time decays and thermal equilibrium is reached after $\approx 500\mu s$.

4.2.2 Required length and buffer gas pressure for the cooling process

Calculations with different pressure were carried out in order to determine the required time or corresponding longitudinal length of the RFQ structure to reach sufficient cooling. In fig. 4.9 the radial amplitude is shown as a function of longitudinal position for Hg^+ ions in an RFQ structure filled with He gas. In diagram (a) the helium pressure is $5 \cdot 10^{-3}\,mbar$, too low to damp the radial amplitudes with the length of the RFQ structure of $1000\,mm$. At $p_{He} = 2 \cdot 10^{-2}\,mbar$ in (b) the Hg^+ ions thermalize after about $l = 900\,mm$ longitudinal travel. For $5 \cdot 10^{-2}\,mbar$ this takes place already at $l = 500\,mm$ in (c), and for a helium pressure of $8 \cdot 10^{-2}\,mbar$ at $l = 300\,mm$.

For operating an RFQ structure under buffer gas the following three practical factors have to be considered:

- Discharge effects: the applied voltages to the gas-filled RFQ structure have to be lower than for high-vacuum conditions.
- Pumping requirements: the buffer gas has to be pumped away outside the RFQ structure.
- Gas impurities: charge exchange processes as a loss of ions.

For all these reasons the required gas load should be kept minimal. It was found that by operating the RFQ structure at a helium pressure of $p_{He} = 2 \cdot 10^{-2}\,mbar$, discharge effects at the required voltages do not occur and the gas load can be removed using differential pumping and standard turbo molecular pumps. A three-dimensional graph of the radial amplitude as a function of time at these conditions is shown in fig. 4.10. From these calculations a conservative length of the RFQ structure on the order of $L = 1200\,mm$ was determined to operate the device in the cooler mode.

The path of the ions within the RFQ structure can be significantly enhanced by applying an additional longitudinal electric field. This prevents the ions from escaping the structure, as shown in fig. 4.11. In this way the ions stay inside for a multi-path period. They lose kinetic energy by interaction with the buffer gas and reach finally thermal equilibrium. The cooled ions, which are distributed along the entire structure, can be extracted by opening the confining potential. However, in

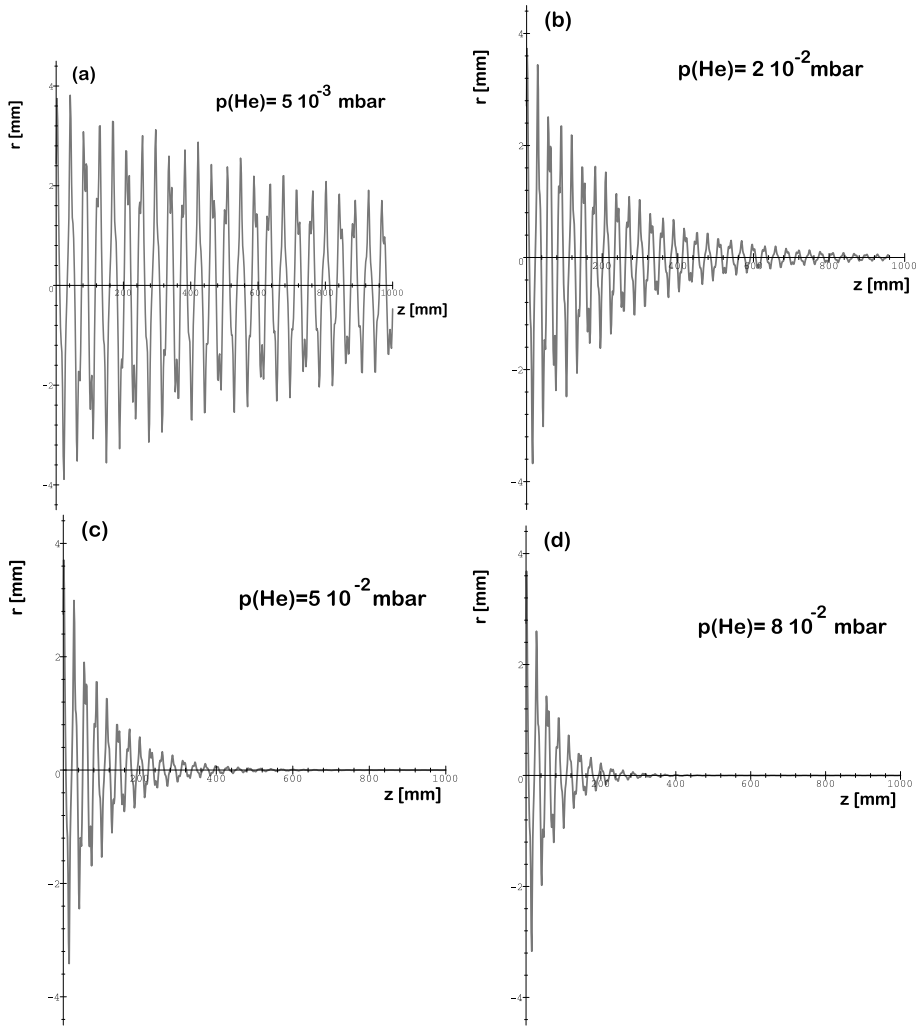

Figure 4.9: Radial amplitude of mercury ions in the RFQ structure of SHIPTRAP filled with He gas with pressures as indicated as a function of longitudinal position in the structure.

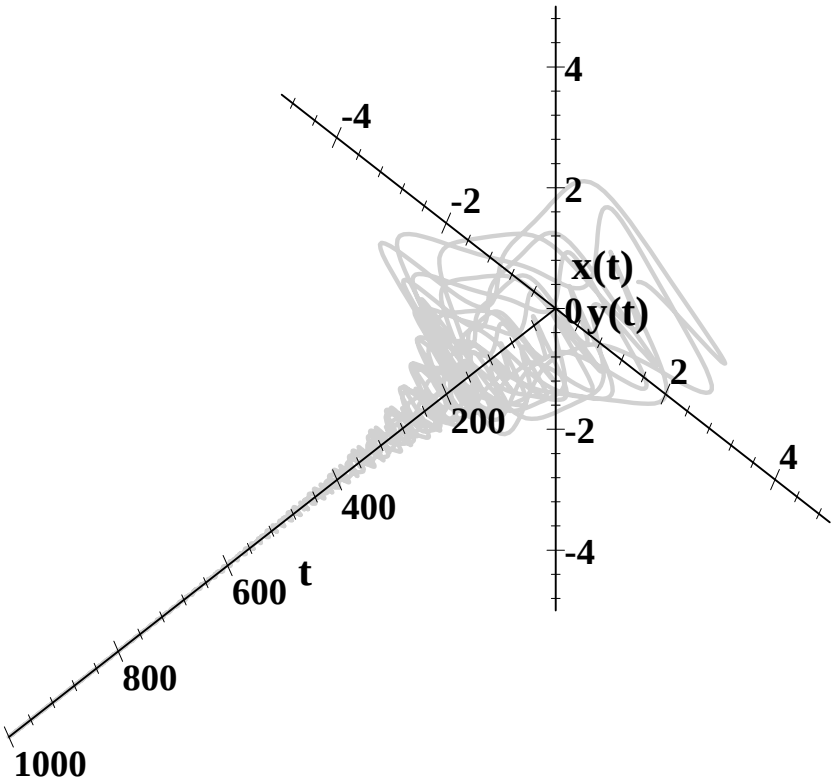

Figure 4.10: Three-dimensional trajectory of Hg^+ ions in the helium gas-filled RFQ structure of SHIPTRAP, operated at $p_{He} = 2 \cdot 10^{-2}\, mbar$. Initial longitudinal and transverse energy is $E_{kin} = 10\, eV$. The time scale is in μs and the radial amplitudes $x(t)$ and $y(t)$ in mm.

that way the extracted ion puls would have a broad puls width. This disadvantage can be overcome by employing a longitudinally segmented RFQ structure with a potential as shown in fig. 4.12. The ions can be loaded permanently and an accumulation in a small region of the RFQ structure takes place, where the ions reach thermal equilibrium with the buffer gas. Figure 4.13 shows calculations of trajectories of mercury ions in an RFQ structure where such a longitudinal potential is applied. In diagram (a) the ion motion in longitudinal direction is damped rather quickly. After few oscillations at about $500\, \mu s$ equilibrium is reached. In the figures (b) and (c) this is not the case, even after $6\, ms$ the motion is not completely damped. Therefore the required gas pressure is on the order of $p_{min} \approx 2 \cdot 10^{-2}\, mbar$.

In such a configuration the collected cooled ions can again be extracted by switching the potential at the exit electrode to a more negative value. The ion ensemble would be extracted as a bunch from the RFQ structure.

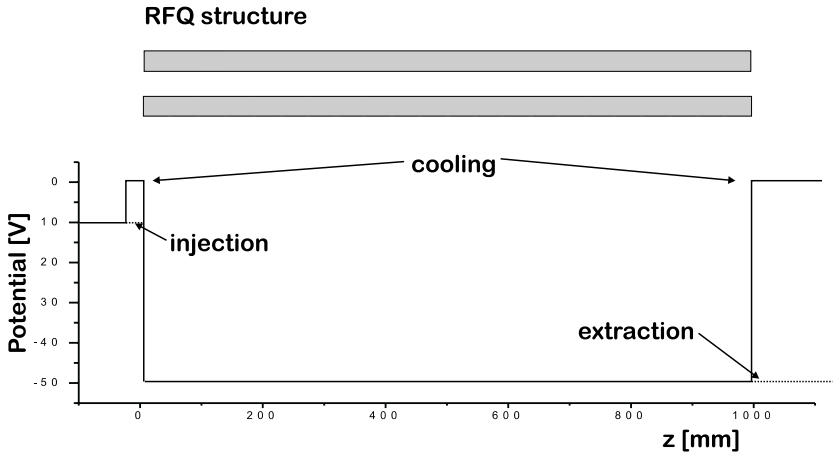

Figure 4.11: Longitudinal confining potential of an RFQ structure.The solid line at $z \leq 0\,mm$ shows the injection condition. The voltage is switched to $0\,V$ at $z \approx 0\,mm$ for cooling the ions after injection. The solid line represents the conditions for cooling. By lowering the voltage at $z \geq 1000\,mm$ (dotted line), the ions can be extracted.

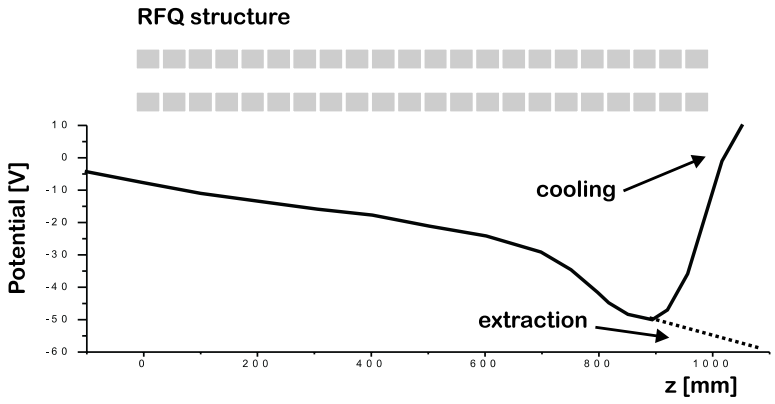

Figure 4.12: Segmented RFQ structure (top) together with a longitudinal confining potential with a smooth gradient and a minimum $U_{min} = -50V$ at z-position $900\,mm$ (bottom). The solid line shows the conditions for injection and cooling, the dotted one for pulsed extraction.

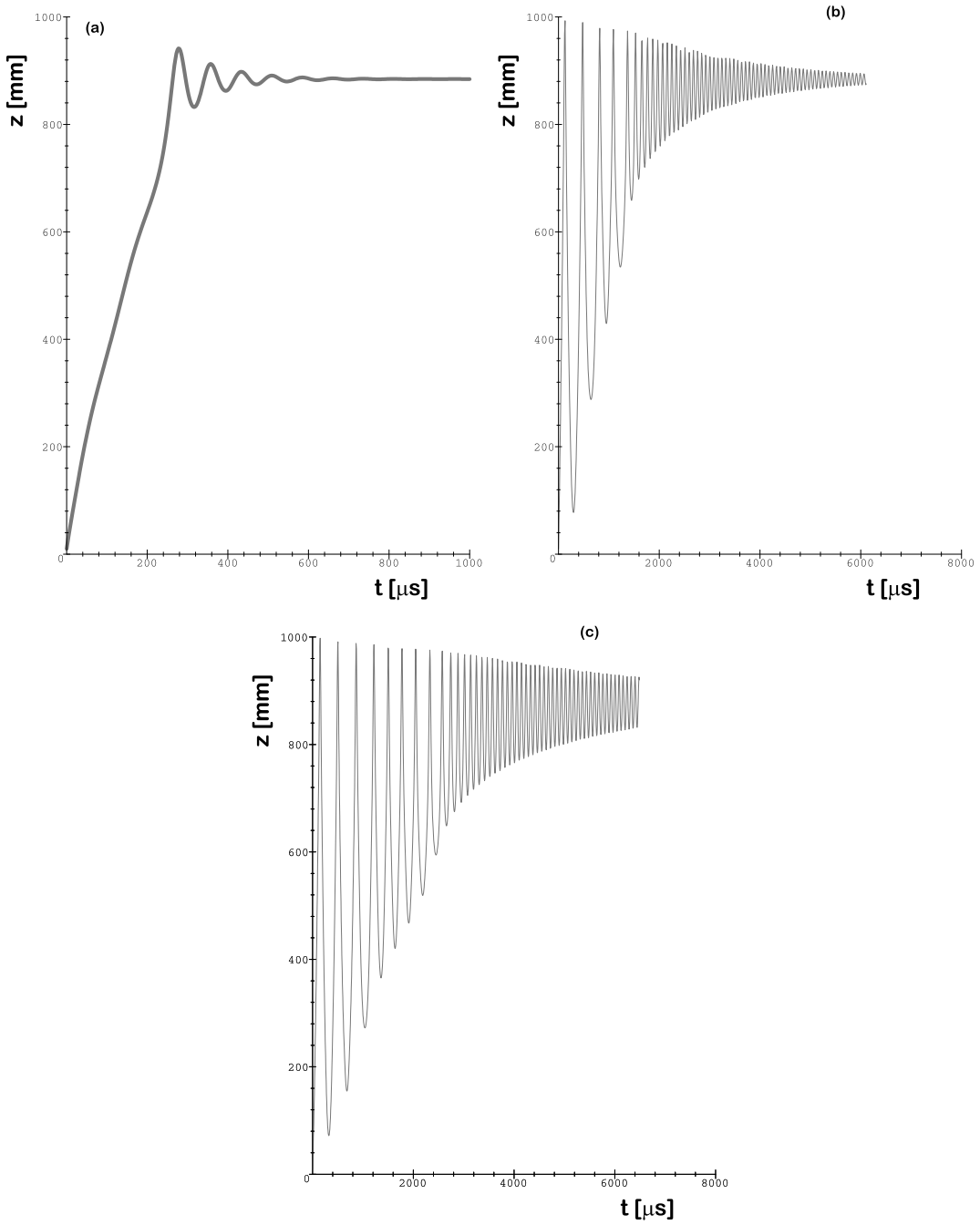

Figure 4.13: Longitudinal position as a function of time of Hg^+ ions in a SHIPTRAP-type longitudinally segmented RFQ structure filled with helium buffer gas.(a) Hg^+ in He at $p_{He} = 2 \cdot 10^{-2}\, mbar$, (b) Hg^+ in He at $p_{He} = 1 \cdot 10^{-3}\, mbar$, (c) Hg^+ in He at $p_{He} = 5 \cdot 10^{-4}\, mbar$. The initial kinetic energy of the entering ions is $E_{kin} = 10\, eV$. Note the different time scales for the graphs.

4.2.3 Properties of the cooled bunch

The properties of the cooled ion ensemble are investigated in a simulation using the SIMION [S3D00] code. This commercial software allows the user to define a geometry including the applied potential. The code calculates the fields where the ion trajectories can be traced through. The used geometry was a SHIPTRAP type RFQ structure with longitudinal potential. The tracing started in the minimum of the longitudinal potential. The following starting conditions were used:

- Ions are in thermal equilibrium with buffer gas. A conservative approximation of twice the buffer-gas temperature ($592\,K$) is taken.
- Ions are randomly Boltzmann distributed.
- Harmonic longitudinal potential is approximated.
- Extraction time $\Delta t = 0$, corresponding to the time to switch the trapping potential to an opening potential.

The ions are released from the RFQ buncher and detected after $z = 1000\,mm$ in the simulation. Kinetic energy, x-and y-position, velocity components and time of flight are recorded and the emittance is calculated. Figure 4.14 (a) and (b) show the longitudinal and transverse emittance for ions with mass $M = 200\,amu$ and an extraction voltage of $U_{extr} = 1000\,V$. The simulation was performed with 3000 ions. The ellipses shown in fig.4.14 contain 95% of the ions. For the longitudinal emittance a value of $\epsilon_{long} = 2.5\,eV\,\mu s$ and for the transverse emittance $\epsilon_{trans} = 5\pi\,mm\,mrad$ was calculated. This corresponds to a beam spot of $2.5 \cdot 2\,mm^2$ shown in fig. 4.14(c). This allows one to transfer the cooled ion sample into the Penning trap apparatus without losses for further manipulation and measurements.

4.3 Experimental realization of an RFQ cooler and buncher

For the work presented here two RFQ structures were designed, built and commissioned. The first one for the ISOLTRAP experiment at ISOLDE / CERN. Here, a prototype RFQ was built and first tests were carried out. This RFQ is now replaced by an improved version, based on the gained experiences. This final ISOLTRAP system is described in more detail in [FHe01b, FHer00]. The second RFQ structure built within this work was for the SHIPTRAP facility at GSI / Darmstadt. In the following the prototype RFQ structure for ISOLTRAP and the one for SHIPTRAP are described.

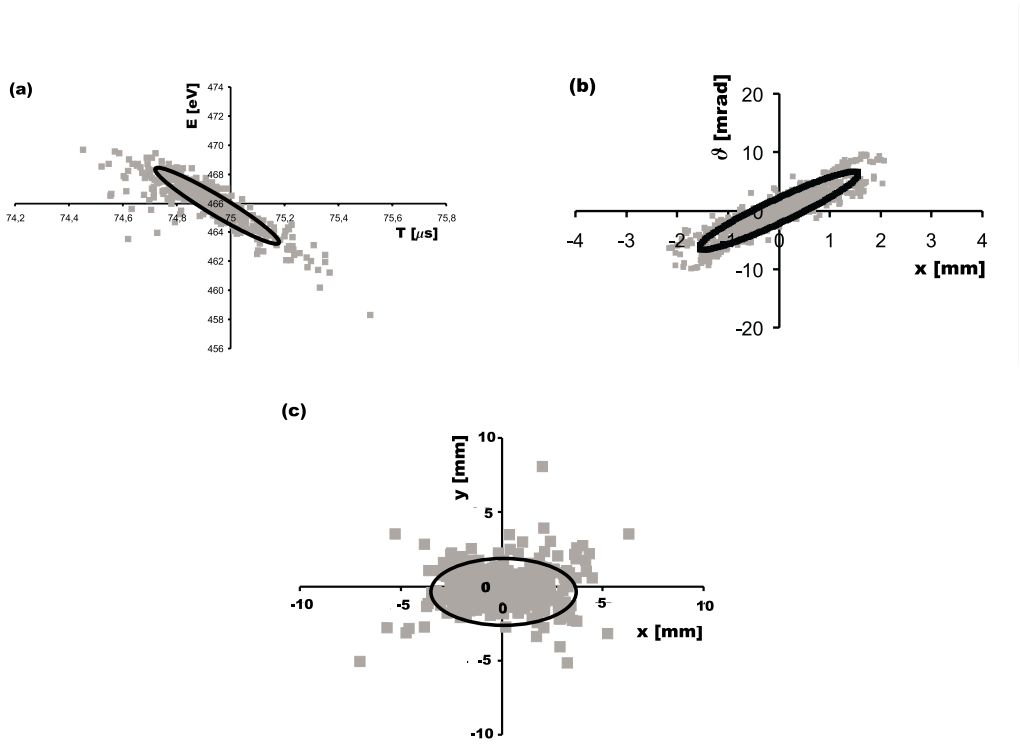

Figure 4.14: Computation of longitudinal (a) and transverse (b) emittance of an ion bunch with $M = 200\,amu$ released from a SHIPTRAP-type RFQ structure after thermal equilibrium with the buffer gas is reached. Extraction voltage $U_{extr} = 1\,kV$. (c) Beam spot at position $z = 1000\,mm$ behind the RFQ is $2.5 \cdot 2\,mm^2$. For details see text.

4.3.1 The ISOLTRAP RFQ buncher

At ISOLDE/CERN, where the ISOLTRAP experiment is located, the DC ion beam has a kinetic energy of $E_{kin} = 60\,keV$ and a transverse emittance of $\epsilon_{trans} = 35\pi mm\,mrad$ [SSi98]. Therefore the requirements for the RFQ structure were the following:

- Convert the $60\,keV$-beam into a beam with an energy below $3\,keV$.
- Reduce the transverse emittance for high injection efficiency of the beam into the Penning trap.
- Transform the DC beam into ion bunches for efficient injection into the Penning trap.

These criteria were approached previously by installing a gas-filled Paul trap [Sch98] with classical three-dimensional hyperbolic geometry. With this device the requirements could be fulfilled. However, the transfer efficiency into and from the Paul trap

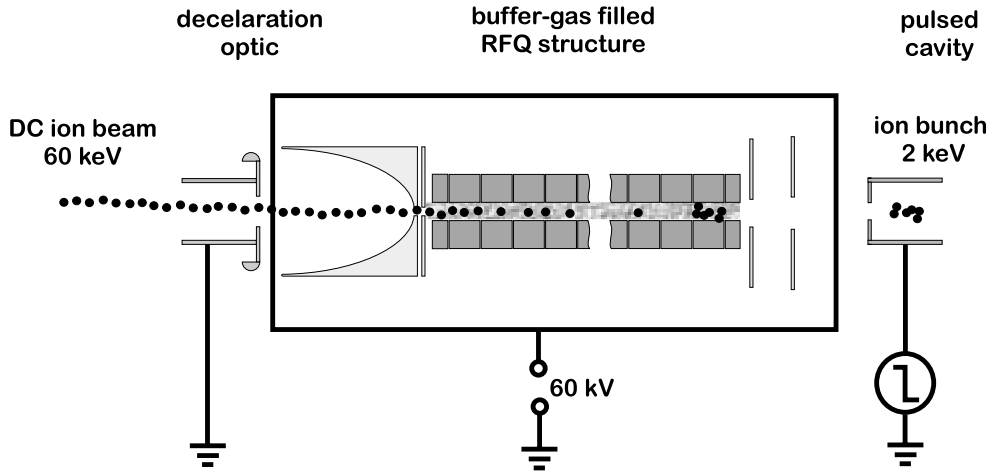

Figure 4.15: Principle of the RFQ cooler and buncher structure for ISOLTRAP.

to the Penning trap spectrometer was rather low ($\epsilon \approx 10^{-7}$). The linear RFQ structure has the advantage over the three-dimensional Paul trap that much lower RF amplitudes are used and injection and extraction are independent of the phase of the applied RF and losses are expected to be minimal. For this reason the ISOLTRAP RFQ buncher was designed.

A schematic of the RFQ system is shown in fig. 4.15. The gas-filled RFQ structure is floating on high voltage. The continuous ISOLDE beam is electrostatically retarded and especially shaped deceleration electrodes [Kel98] focus the beam into the RFQ. Interactions with the buffer gas cool the ions as discussed in the previous section. They accumulate in the end section of the structure. Then, the extracted bunch enters a pulsed cavity [Sch98]. While the bunch is inside the tube, the applied potential is switched from $U_{enter} = 58\,kV$ to ground. Because the tube acts as a Faraday cage, the singly-charged ions keep the initial potential difference between RFQ structure and pulsed cavity as kinetic energy. With this RFQ-concept all requirements could be matched.

The design of the RFQ itself is based on concepts developed at McGill University [Kim97]. Investigations of the cooling process were carried out at McGill using an RFQ structure with a length of $400\,mm$, operated without longitudinal trapping. For the ISOLTRAP buncher this concept was further developed and other considerations had to be taken into account:

- All material for the structure should be chosen to reach UHV. This is necessary to avoid charge exchange processes with residual gas atoms and molecules that would lead to a loss of ions. This is a condition that arises from the nature of on-line experiments, where the ions to be investigated are often produced only in low quantities. Therefore all loss mechanisms should be minimized.

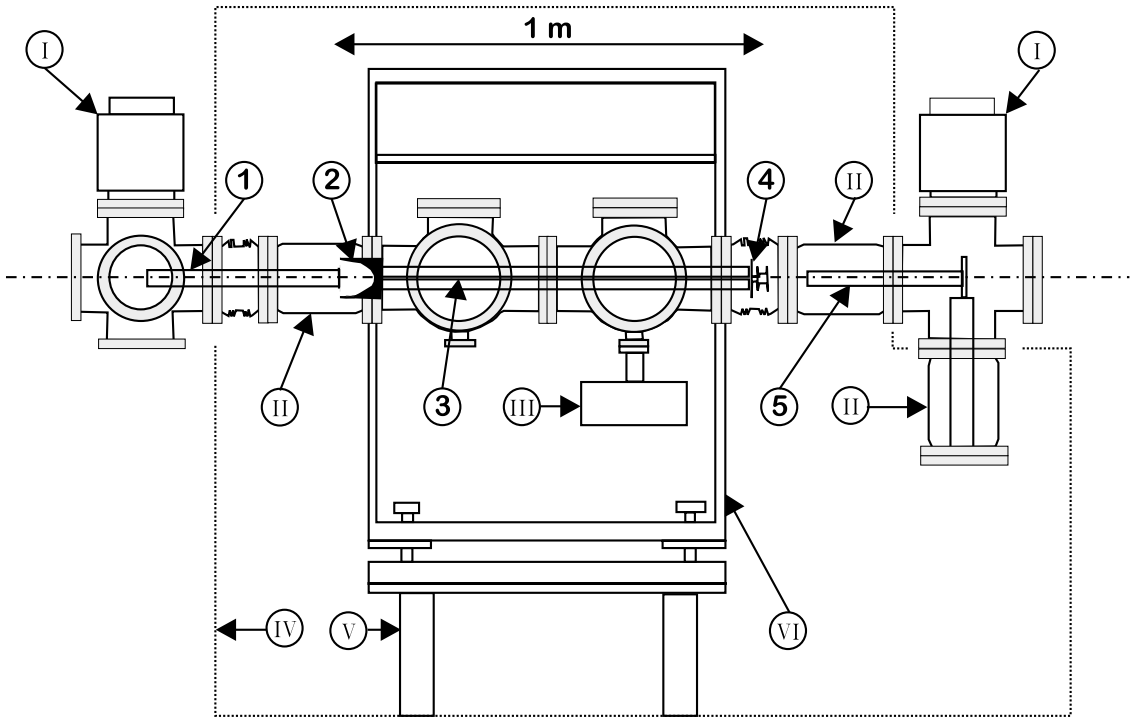

Figure 4.16: Experimental set-up of the buncher RFQ structure for ISOLTRAP. 1: grounded injection electrode, 2: focusing retardation electrode, 3: RFQ structure, 4: extraction optics, 5: pulsed cavity, I: vacuum pumps, II: ceramic insulator tubes, III: DC and RF supplies, IV: grounded cage, V: insulator support stand, VI: high voltage cage.

- Gas load should be handled with standard turbo molecular pumps which are located outside the high-voltage area.

Experimental set-up

Figure 4.16 shows the experimental set-up of the buncher structure of ISOLTRAP. The ISOLDE beam with $E_{kin} = 60\,keV$ enters the structure from the left. On the right the bunches are ejected into the beam transport system of ISOLTRAP. The complete system including RF- and DC-supplies, electronics and gas inlet system is situated on a high-voltage platform (VI). This platform is mounted on plastic insulators (V) inside a grounded cage (IV). The connection to the beam lines is made via ceramic vacuum tubes (II) of length $L = 250\,mm$. The pumps (I) are located just outside the grounded cage on beam-line potential. More details concerning the vacuum system and the gas-inlet are given in section 4.3.1. The ion optical system consists of three main parts, namely the decelaration optics, the RFQ structure, and the pulsed cavity.

Table 4.2: Dimensions of the RFQ structure for ISOLTRAP.

Element	Dimension [mm]
length of grounded injection electrode	400
opening diameter of grounded injection electrode	10
opening diameter of injection electrode	6
diameter of rod electrode	12
diameter of outer support rod	8
diameter of gas-sealing rod	6
open diameter between opposite rods ($2 \cdot r_0$)	12
length of rod electrode	20
thickness of mica spacer	0.03
length of end electrode	10
total length of RFQ rods	861.29
diameter of extraction hole	6
length of pulsed cavity	380

Injection

The decelaration optics is specifically arranged to accept the ISOLDE beam. It consists of a grounded injection tube. The next element is an elliptical shaped (semi-axes: $r_1 = 85\,mm\,, r_2 = 43\,mm$) electrode sitting at a DC potential of $U_1 = 58.9\,kV$. The following optical element is a disc of thickness $L_{disc} = 2\,mm$ with a hole of $d = 5\,mm$. This element is supplied with a DC voltage of $U_2 = 59.9\,kV$. This configuration together with the attached RFQ structure elements at proper potential allows one to refocus the electrostatically retarded and therefore diverging ISOLDE beam into the RFQ structure. This system is described in more detail in [Kel98].

RFQ structure

The second ion optical system is the RFQ structure. As described above, it consists of four rods which are longitudinally segmented. The mechanical principle is depicted in fig.4.17 and dimensions are given in table4.2. The concept of the separation of electrodes is shown in (a) and is based on cylindrical electrodes sitting on an aluminum oxide ceramic tube. Mica spacers are employed to insulate the adjacent electrodes from each other. The end electrodes (not shown) are attached to the inner support rod providing a clamping of all elements. The four rods are fixed to a mounting disc ((b)) via ceramic stand-off elements. Additional outer support rods stabilize the structure. These outer support rods together with eight ceramic sticks, so-called gas sealing rods, form basically a closed structure in radial direction.

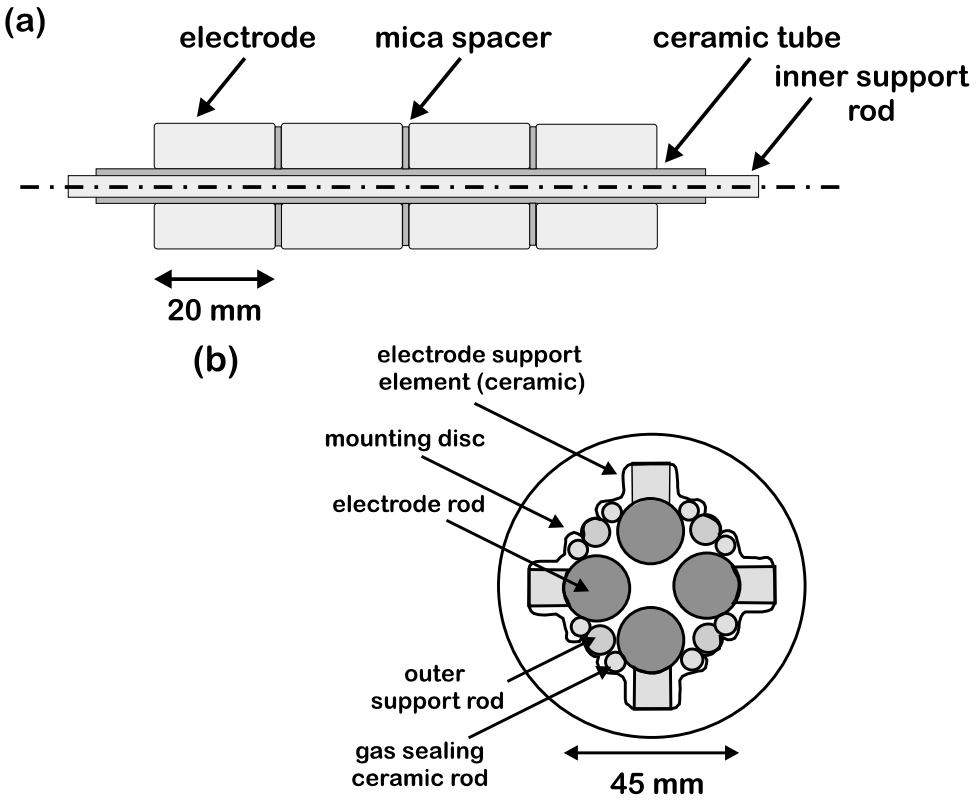

Figure 4.17: Mechanical principle of the RFQ structure for ISOLTRAP.

The potentials on the last RFQ segments can be switched to extract the cooled ion bunch. For ion optical adjustments a set of vertical and horizontal steerers and an einzel lens system is used. For accelerating the ions out of the RFQ structure a potential difference between the RFQ high-voltage platform and the pulsed cavity on the order of two to three kV is initially applied. By pulsing the last segments of the four rod structure the ion stack enters then the drift tube. A fast high-voltage switch (Behlke HTS 650) with a rise time of $\tau \approx 250\,ns$ grounds the cavity while the bunch is inside. Therefore the ions exiting the cavity keep their initially gained kinetic energy. The tube is mounted in an adjustable way to match the longitudinal axes with the RFQ axes. This principle is described in more detail in [Sch98].

For all ion-optical elements only UHV compatible material was employed. Stainless steel was used for the electrodes, mica, aluminum oxide or glas-ceramic was employed for insulation and the electrical connections were made with Capton coated wires.

Vacuum system

The gas load required for the cooling process has to be removed employing differential pumping and standard turbo molecular pumps which should be located outside the high-voltage area. A point of concern are discharge processes which occur at rather low voltages with such a high gas pressure. A particularly critical area is the grounded injection tube facing the decelaration electrode with a $5\,mm$ gap and a potential difference of nearly $60\,kV$. The Paschen curve [Mee53] for helium gives a maximum pressure on the order of $10^{-5}\,mbar$ before discharges occur. Finally, reasonable vacuum conditions should be reached in the ISOLDE beam line in front of the RFQ buncher and towards the Penning trap spectrometer. Therefore, the following criteria should be fulfilled:

- Base pressure, without buffer gas, in the UHV regime.
- Buffer gas pressure for cooling in the interior of the RFQ: $p_{He} = 2 \cdot 10^{-2}\,mbar$.
- Maximum pressure to avoid discharge at decelaration electrode $p_{He} \approx 10^{-5}\,mbar$.
- ISOLDE and transfer beam line pressure $p_{He} \approx 10^{-6} - 10^{-7}\,mbar$.

From these conditions the following system was designed. Stainless steel chambers of CF 150 and CF 100 were employed as vacuum housing. Two magnetic-bearing double-stage turbo molecular pumps (Pfeiffer TMU 1000MC) with a pumping speed of $870\,l/s$ for helium were placed just outside the high-voltage area. These pumps were backed by one $40\,m^3/h$ pre-pump. Differential pumping was accomplished by sealing the He gas region in the RFQ structure from the exterior and allowing the gas flow only through the small openings of the beam entrance and exit. This region is therefore pumped only through those diaphragms. The gas inlet is a stainless steel capillary tube connected to the central region of the RFQ structure. The gas flow is controlled with a needle valve which is regulated via a controller (Balzer EVR 116 and RVC 200). With this controller also a full-range pressure gauge (Balzer PKR 250) connected to the vacuum chamber is read out. The measured pressure was found in initial tests to be about one order of magnitude lower than inside the RFQ structure. With this gas inlet and read-back system the pressure can be kept stable within 5%. Table 4.3 shows the results of gas flow calculations and the experimental values. The RFQ interior is assumed to be cylindrical and the flow to be in the laminar regime [Wut95].

The experimental results for operating the system without buffer gas showed at the RFQ vacuum chamber values of $p_{RFQ} = 1 \cdot 10^{-7}\,mbar$ after a standard preparation procedure. This is in accordance with the expectations, where only the out-gassing from the metal surfaces is taken into account. Operating the system with buffer-gas allowed one to apply the required high voltage. Therefore all necessary criteria could be matched.

Table 4.3: Results of gas flow calculations and experimental test of the ISOLTRAP RFQ vacuum system. A cylindrical tube for the interior of the RFQ and laminar flow are assumed. The initial helium flow at the gas inlet is $Q = 4 \cdot 10^{-2}\, mbar \cdot l/s$. The calculated pressure (P_{cal}), the calculated effective pumping speed (S_{eff}) and the experimental pressure (P_{exp}), if available, are listed.

Position	P_{cal} [mbar]	S_{eff} [l/s]	P_{exp} [mbar]
inside RFQ (center)	$2 \cdot 10^{-2}$	2	$3 \cdot 10^{-2}$
inside RFQ (decel. el.)	$3 \cdot 10^{-3}$	5	
between grd. and decel. el.	$4 \cdot 10^{-5}$	355	
cross underneath pump	$2 \cdot 10{-}5$	680	$3 \cdot 10^{-5}$
transfer beamline	$1 \cdot 10^{-7}$	820	$1 \cdot 10^{-7}$

Experimental test results

Tests were carried out with this prototype RFQ structure to check the performance of the device. Figure 4.18 shows photographs of the assembled RFQ structure, together with the retardation electrode (a) and a view along the axes (b).

First tests were carried out in order to reach the necessary pressure conditions for cooling of the ions inside the RFQ while apply the required high voltages for the retardation. The RF potentials where applied and amplitudes of up to $V_{pp} = 130\, V$ could be achieved at a frequency of $\Omega/2\,\pi = 520\, kHz$. This corresponds to a stability parameter of $q = 0.5$ for mercury or cesium ions at different RF voltages. However, difficulties arose when switching the trapping DC potential open for the extraction process. Discharges occurred due to changing the voltages from $U_{trap} = +2\, V$ to $U_{extr} = -200\, V$. The discharge processes caused permanent contacts by forming conducting bridges within the mica spacers. These made the application of the longitudinal trapping potential impossible in its foreseen manner and trapping could not be established. Therefore only tests without longitudinal trapping potential were carried out corresponding to single-pass non-bunched experiments. For example, a check of the injection of the ISOLDE beam into the device was performed. Applying the necessary high voltages for retardation and an RF-field of $U_{pp} = 130\, V$ at $\Omega = 520\, kHz$ the continuous beam was detected on the extraction plate of the ejection ion optics with a pico-amperemeter. Efficiencies on the order of $\epsilon = 10\%$ were found by comparing the currents measured in this way with the current measured by a Faraday-cup in the transfer beam line of ISOLDE up-stream the RFQ structure.

Based on the experience of these tests the design of a new buncher device with a different mechanical concept was necessary. The structure presently in use at ISOLTRAP is described in [FHe01b, FHer00]. The concept based on ceramic cylin-

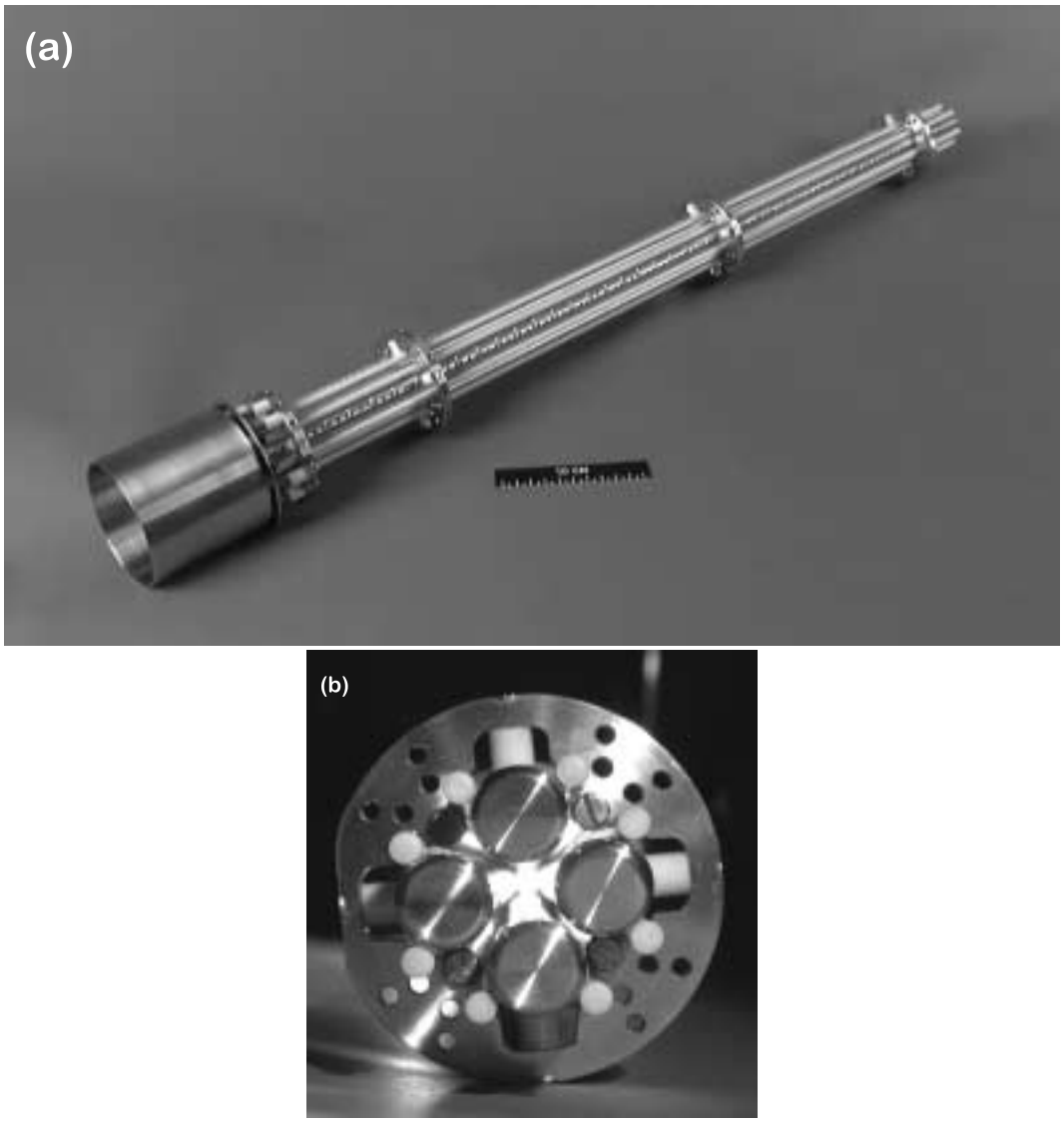

Figure 4.18: Photographs of the RFQ structure for ISOLTRAP. (a) Assembled structure together with the retardation electrode. (b) View along the structure.

ders as spacers was therefore also used for the SHIPTRAP buncher and is presented in the next chapter. With the new RFQ structure of ISOLTRAP experiments where carried out which are presented in chapter 6.4.

4.3.2 The SHIPTRAP RFQ buncher

A second RFQ structure for the SHIPTRAP experiment at GSI/Darmstadt was built. Here, the requirements are quite different from those for the ISOLTRAP device:

- The entering beam has lower kinetic energy ($E_{kin} \approx 100 - 200\,eV$).
- No high-voltage platform is needed.
- The mass of the nuclides to be investigated is higher, going up to $M = 260\,amu$.
- A large gas flow has to be taken into account entering the four rod structure from the stopping chamber operating at high gas pressure.

Figure 4.19 shows the experimental set-up of the SHIPTRAP RFQ structure with an ion source for test purposes. Ions are injected from the left into the RFQ structure where cooling and bunching is performed. Then, the ions are extracted and detected with either a channeltron, a Faraday-cup or by a beam-viewing system. The vacuum system consists basically of five vacuum vessels, one CF 100 double-cross for the ion-source, three CF 150 crosses for the RFQ structure and another CF 100 double-cross for the detection section. The complete structure is pumped by four turbo molecular pumps, two pumps with a pumping speed for helium of $400\,l/s$ (Pfeiffer TMU 450MC) (I) and two with $870\,l/s$ (Pfeiffer TMU 1000MC) (II). All four turbo pumps are backed separately by $14\,m^3/h$ roughing pumps.

Ion source and injection optics

A commercial crossed-beam ion source (Pfeiffer BN845346) (fig.4.19 Nr.1) is installed in the first double-cross. The ion source is connected to a gas inlet which allows one to feed in He, Kr or Xe gas. The ion source and the extraction ion optics are directly coupled to the RFQ structure. Ion optical simulations with the SIMION [S3D00] code showed a transfer efficiency of 100% from the source to the structure. Figure 4.20 shows the geometry of the ion source and the injection optics together with equipotenial lines.

RFQ structure

The RFQ structure consists of four segmented rods where the separation of the individual electrodes is done with ceramic cylinders. Figure 4.21 shows the basic mechanical concept. The electrodes have a notch in which the ceramic spacers fit. The gap between neighboring electrodes is $l = 0.2\,mm$. The ceramic cylinders are

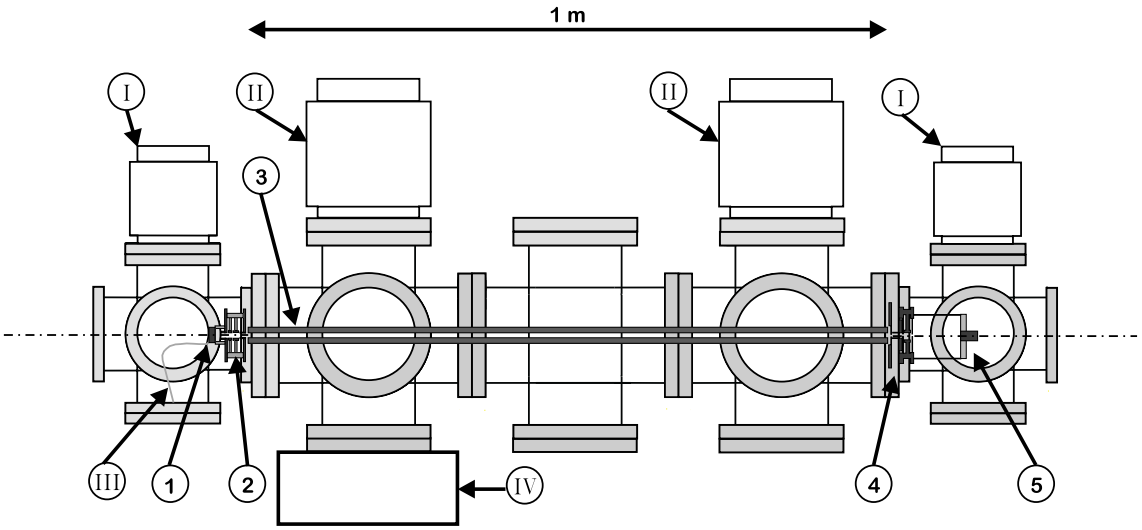

Figure 4.19: Off-line set-up of the RFQ structure for SHIPTRAP. 1: cross beam ion source, 2: injection ion optics, 3: RFQ structure, 4: extraction optics, 5: detection system, I and II: turbo pumps, III: ion source gas feeding, IV: RF and DC supplies.

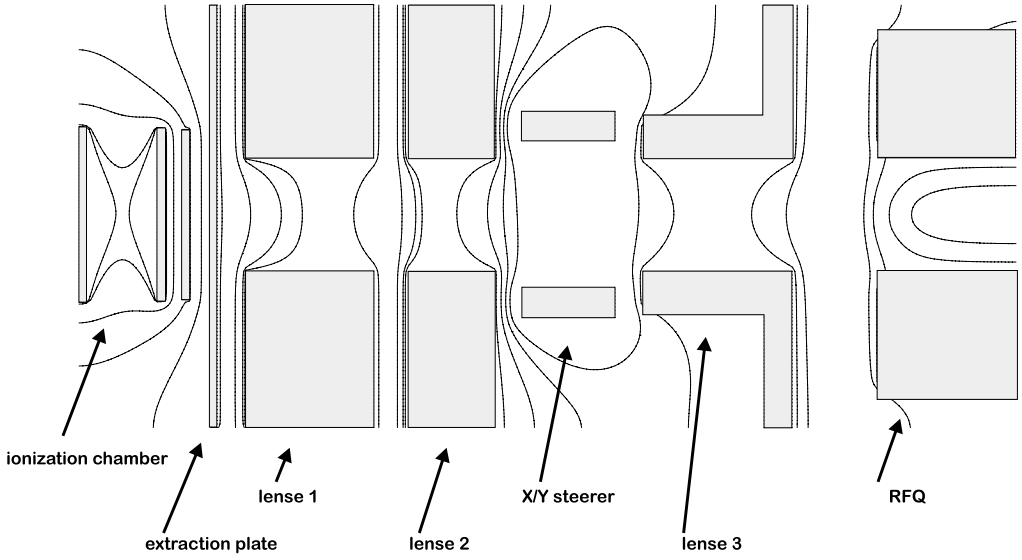

Figure 4.20: Geometry and equipotential contour lines for the ion source and injection optics. Applied voltages are given in table 4.5.

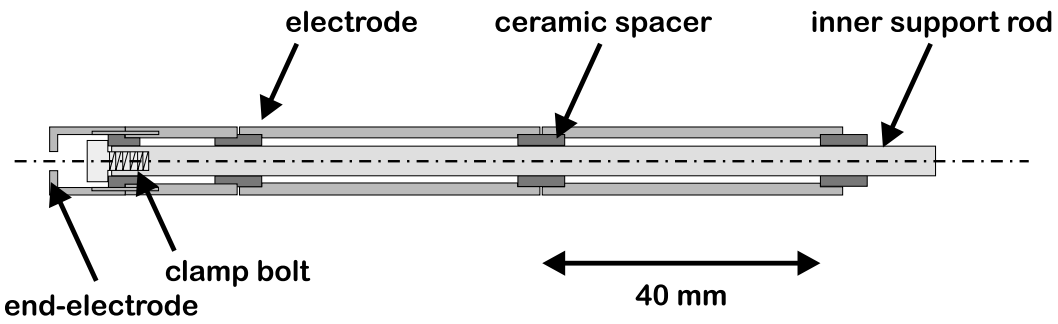

Figure 4.21: Mechanical principle of the SHIPTRAP RFQ structure.

mounted on the inner support rod. Special end electrodes are connected to the inner rod. In this way all electrodes are clamped together longitudinally. The rods are held in place by a glas ceramic mounting disc. Table 4.4 gives details of the mechanical dimensions. The electrode diameter and therefore also the inner radius r_0 is only 2/3 the size of the ISOLTRAP device. This is mainly due to the higher mass range to be transmitted. Since the stability parameter q is defined as $q = \frac{2 \cdot q_e \cdot V}{\Omega^2 \cdot r_0^2 \cdot m}$ the same q-value as for the ISOLTRAP geometry can be reached with only about 40% of the RF amplitude. This is of great importance for high masses because less RF power is required. The smaller geometry is here also applicable due to the different properties of the injected beam. A retarded and diverging beam has to be accepted at ISOLTRAP, while for SHIPTRAP a low-energetic ($E_{kin} = 100\,eV$) beam is entering the structure. The length of the electrodes is not equal, but rather electrodes of different dimensions were used to optimize the harmonicity of the trapping potential (see table 4.4). This is another modification with respect to the ISOLTRAP geometry.

Extraction and detection

In the last chamber the detection system including the extraction ion optics is housed. The extraction optics is optimized for maximum transfer efficiency using the simulation code SIMION. Figure 4.22 shows calculations where the cooled ions are extracted from the RFQ structure and accelerated onto a detector. Parameters of operation of the system, including extraction, are listed in table 4.5. Two detectors system are foreseen to monitor the ejected beam bunch: a Faraday-cup (FC) combined with a channeltron detector (Pfeiffer BKM 25252) and a beam-viewing system (Colutron BVS-1). The latter consists of a micro-sphere plate in front of a phosphor screen and a CCD-camera. The FC detector can be used for higher ion currents ($I_{ion} = \mu\, A$), when a non-bunching mode is applied or in high-pressure conditions (for example at $p = 2 \cdot 10^{-5}\, mbar$). For single-ion counts the channeltron is employed. With the beam-viewing system the spatial properties of the extracted

Table 4.4: Dimensions of the RFQ structure for SHIPTRAP

Element	Dimension [mm]
diameter of rod electrode	9
open diameter between opposite rods ($2 \cdot r_0$)	7.8
length of rod electrode #1 - #21	40
length of rod electrode #21 - #27	20
length of rod electrode #28 - #30	10
length of rod electrode #31	8
length of rod electrode (trap center) #32	4
length of rod electrode #33	8
length of end electrode	25
total length of RFQ rods	1067

bunch can be monitored and the transverse emittance profile can be investigated.

Special care has to be taken with respect of loss mechanisms, since the SHIPTRAP RFQ structure is foreseen for the cooling and bunching of exotic nuclides with low production yields. The entire set-up is made out of stainless steel and ceramic to avoid charge-exchange processes with residual gas atoms or molecules. Even the connection wires used are stainless steel. This allows one to bake the system and reach UHV conditions.

Vaccum tests

Figure 4.23 shows photographs of the assembled structure and details of the electrodes and spacers. With this RFQ structure the initial experiments were performed. Vacuum tests were first carried out as to see whether the requirements could be matched. Table 4.6 lists the achieved values without out-backing the system. An operation is feasible under these conditions.

Transmission tests

Transmissions test with the RFQ structure were carried out for Ar^+ and Xe^+ ions without buffer gas and hence without cooling and bunching. The ions were created in the crossed-beam ion source, which was fed by the noble gas. The transfer ion optics between ion source and buncher was operated with maximum transmission. For the experiments, the RF amplitude was varied between $0\,V_{pp}$ and $45\,V_{pp}$ for argon ions at RF frequency $600\,KHz$ or between $0\,V_{pp}$ and $130\,V_{pp}$ for $\nu_{RF} = 1\,MHz$. A Faraday cup behind the buncher was used for the detection of the ion current. Figure 4.24 shows two transmission curves for argon ions at the different frequencies. The entire scope of the stability parameter q is covered for both plots. Since the buncher was

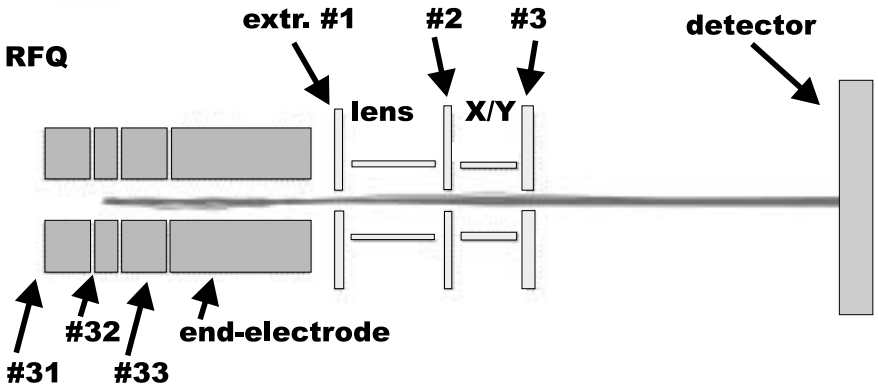

Figure 4.22: Simulation of the extracted ion bunch from the RFQ structure for SHIPTRAP.

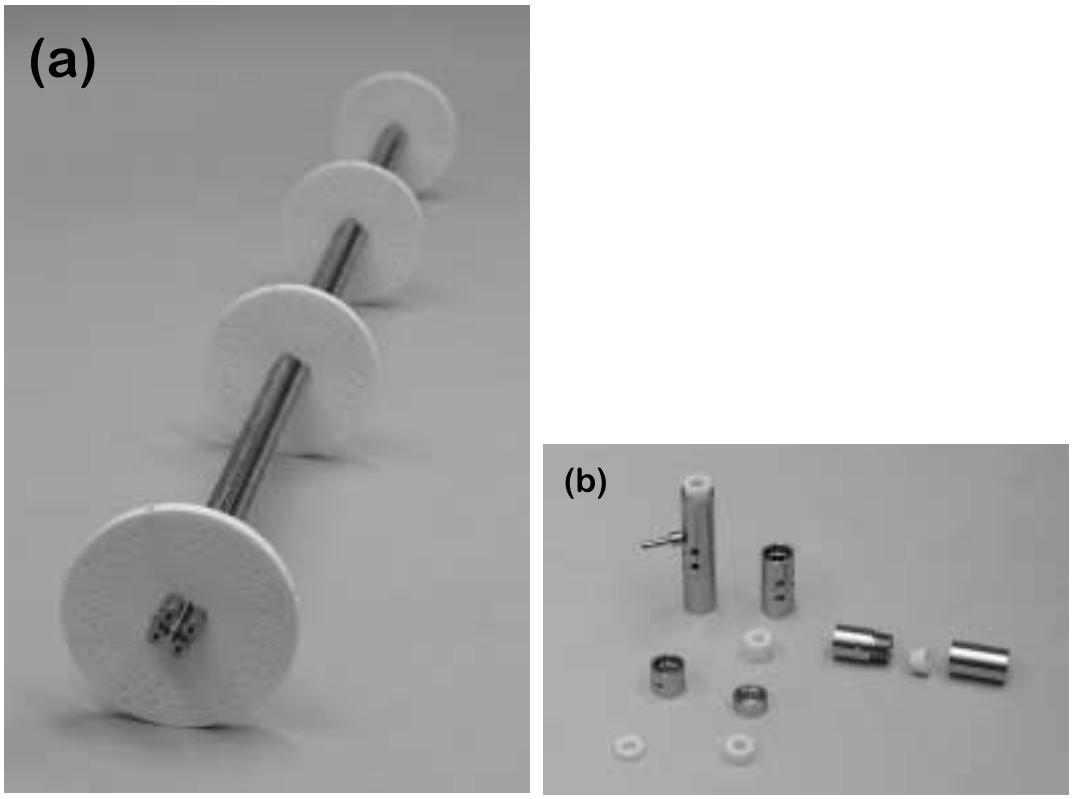

Figure 4.23: Photographs of the RFQ structure for SHIPTRAP. (a) Assembled structure, (b) electrodes and ceramic spacers.

Table 4.5: Parameters for operation of the RFQ structure for SHIPTRAP.

Element / Parameter	value
Injection	
potential applied at:	
ionization chamber	$+90\,V$
extraction plate	$-100\,V$
lens 1	$+20\,V$
lens 2	$+70\,V$
X-Y-steerer	$+70\,V$
lens 3	$+20\,V$
RFQ	
pressure (He)	$3 \cdot 10^{-2}\,mbar$
RF frequency $\nu = \Omega_{RF}/2\pi$	$1\,MHz$
RF amplitude V_{RF} for Kr-ions	$110\,V$
RF amplitude V_{RF} for Xe-ions	$80\,V$
potential applied at:	
rod electrode #1	$+70\,V$
rod electrode #2	$+80\,V$
rod electrode #3	$+82\,V$
rod electrode #4 - #30	+80 to +70 V
rod electrode (trapping) #31	$+65\,V$
rod electrode (releasing) #31	$+90\,V$
rod electrode (trap center) #32, 33	+60 V
rod electrode (trapping) #34, 35	$+90\,V$
rod electrode (releasing) #34, 35	$-1\,V$
Extraction	
potential applied at:	
extraction plates	$-200\,V$
lens	$-50\,V$
X-Y-steerer	$-50\,V$

Table 4.6: Pressures of the RFQ system for SHIPTRAP with and without buffer gas.

	Ion source chamber	RFQ chamber	Detector chamber
base pressure	$2 \cdot 10^{-8}\,mbar$	$1 \cdot 10^{-8}\,mbar$	$3 \cdot 10^{-8}\,mbar$
buffer gas	$3 \cdot 10^{-5}\,mbar$	$8 \cdot 10^{-3}\,mbar$	$2 \cdot 10^{-6}\,mbar$

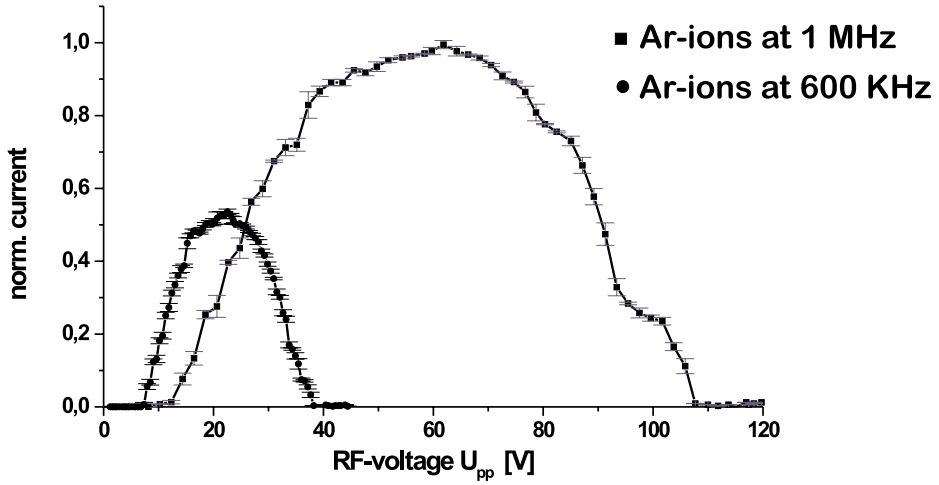

Figure 4.24: Transmission curve for Ar^+. The normalized current is shown as a function of applied RF amplitude for an operation with $\nu_{RF} = 600\,KHz$ and $\nu_{RF} = 1\,MHz$. The solid line is only to guide the eye.

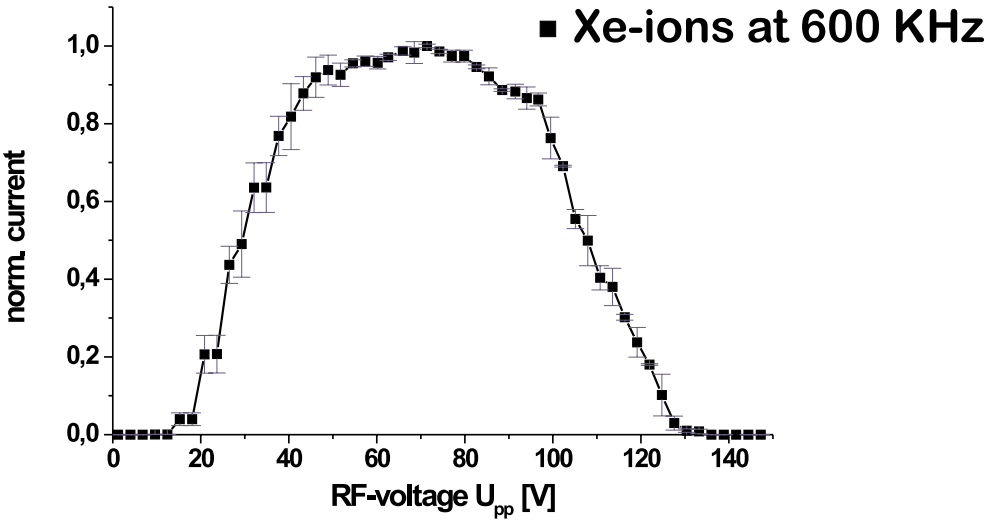

Figure 4.25: Transmission curve of Xe^+. The normalized current is shown as a function of applied RF amplitude for an operation with $\nu_{RF} = 600\,KHz$. The solid line is only to guide the eye.

operated in the RF-only mode, the stability parameter a is zero. The shape of the transmission curves are not of box form, but show some structure. This is due to the imperfect matching of the emittance with the ion source and the acceptance of the RFQ structure and also of the subsequently following detector. This behavior was investigated and is well understood (see for example [Mun95, Bla98]). The maximum currents of the two curves are also different. This can be understood by using the pseudopotential model [Deh67]. The motion of the charged particle in the RFQ-field is not described exactly, but rather first-order terms of the solutions are used for this model. Here the macro motion is considered as the motion of the particles in a pseudopotential well of depth V_{RF} given by

$$V_{RF}(r) = \frac{q \cdot U_{RF}}{4r_0^2} r^2 \,. \tag{4.17}$$

Since for higher frequencies the applied RF amplitudes are higher for the same q-parameter, the pseudopotential $V_{RF}(r)$ is deeper. This explains the higher currents of argon ions at $\nu_{RF} = 1\,MHz$. The transmission curve for Xe^+ is shown in fig. 4.25. Due to the mass dependence of the q-value the required RF-amplitude is higher as compared to argon to cover the complete stability spectrum. The maximum amplitude for transmission is reached at $q = 0.908$, corresponding to $U_{max} = 130V$. The diagram shows that basically nothing is transmitted at higher amplitudes. However, the edge for the transmission border is sharper for the argon curves at $U_{max} = 40.6\,V$ and $U_{max} = 113.4\,V$. This is probably due to the wider mass range of the natural isotopes of xenon as compared to the case of argon. Since regular gas bottles of noble gases (99.4) were used, the natural distribution is present.

These first tests showed the principle performance of the RFQ structure. Parameters for the operation were found for argon and xenon ions, were transmission is maximized and which can be used for the investigations of cooling and bunching.

The next step is the application of the longitudinal trapping potential under buffer gas conditions. These investigations are presently under way and are described in [Rod].

Chapter 5

The SHIPTRAP experiment

5.1 The experimental set-up

The SHIPTRAP experiment [Dil99] is currently being set up at GSI /Darmstadt. The novelty of SHIPTRAP is the coupling of an ion trap to an in-flight facility. The exotic nuclides are produced by a primary ion beam impinging on a thin target. The recoil particles are separated in-flight at typical energies of 20-500 keV/u using the velocity filter SHIP [Mue79]. The products are detected with a time of flight detector at the end of the system. Figure 5.1 shows the principle set-up of SHIP. For the on-line operation of the SHIPTRAP experiment the last element of SHIP, the time of flight detector, will be removed and the beam is transferred to the trapping facility. The principle components of SHIPTRAP are shown in fig. 5.2. The SHIPTRAP experiment consists of six basic elements. These are the stopping gas cell with extraction radiofrequency quadrupole (RFQ), the beam cooler and buncher RFQ, two Penning traps and a time of flight detector.

The exotic beam from SHIP will be stopped in the gas cell and extracted as a quasi-continuous low-energy beam ($E_{kin} \approx 100\,eV$) using the gas flow through a nozzle and electric fields. The extraction RFQ transfers the ions to the buncher trap. Here the ions are cooled by collisions with buffer gas. From the linear Paul trap the ions are extracted in a bunched mode. The ion stack is transported to the first Penning trap (purification trap) where the ensemble is purified via mass selective buffer gas cooling. In the next step the selected ions are injected into the measurement trap where the mass is determined via methods explained above. In the following the different components are described in detail.

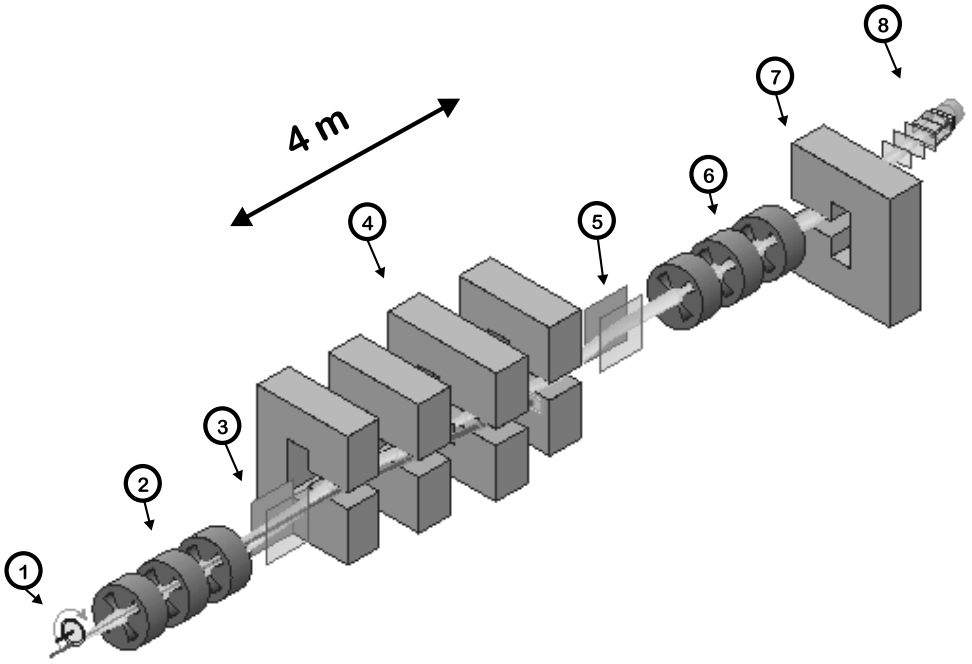

Figure 5.1: Experimental set-up of the SHIP facility. 1: rotating target wheel, 2 and 6: quadrupole lenses, 3 and 5: electric deflectors, 4 and 7: dipole magnets, 8: time of flight detector.

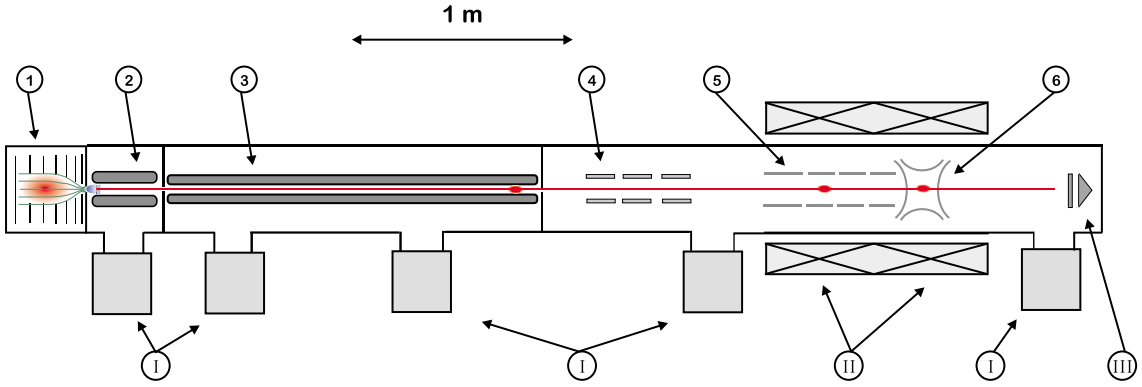

Figure 5.2: Experimental set-up of the SHIPTRAP experiment. 1: gas-filled stopping chamber, 2: extraction RFQ, 3: RFQ cooler and buncher, 4: transfer optics, 5: purification Penning trap, 6: precision Penning trap, I: turbo molecular pumps, II: super-conducting magnet with two homogeneous regions, III: time-of-flight detector.

Gas-filled stopping cell

The exotic ions from SHIP with typical energies between $20 - 500\,keV/u$ enter the stopping volume through a thin window. By interaction with the gas the ions are stopped and thermalized. The required helium gas pressure is between $10^{-5} \leq p_{He} \leq 100\,mbar$ depending on the initial energy of the exotic nuclides. The ions, predominantly singly charged, are then guided by electrostatic fields towards the exit nozzle of the cell. Investigations have demonstrated the proof of principle [Mai00, Mai99]. Extraction efficiencies on the order of 50% for similar devices [Sav00] have been reached. The stopping cell for SHIPTRAP is presently being developed in Munich [Eng00, Neu].

Extraction RFQ

The main purpose of this extraction RFQ is to guide the diverging beam from the stopping cell and allow for differential pumping between the gas cell and the RFQ cooler. The extraction RFQ is segmented to apply a longitudinal potential. Great care has to be taken with respect to discharge processes, which are critical in such pressure regimes. The extraction RFQ is also developed in Munich and is described in more details in [Eng00].

RFQ cooler and buncher

As described in previous chapters, with this component the ion beam is cooled to buffer gas temperature and converted into ion bunches. Differential pumping allows one to reach a pressure in the $10^{-6} - 10^{-7}\,mbar$ regime in the transfer section after the RFQ cooler.

Transfer section

Ion optical electrodes and lenses are used to transfer the ions from the RFQ structure to the Penning trap system with basically 100% efficiency. Two einzel lens systems are foreseen. This section has two practical purposes: to provide space for a pumping section and to mount vacuum valves to separate the gas-filled RFQ structure from the Penning trap section.

Purification Penning trap

Mass-selective buffer gas cooling in a Penning trap is the method of choice to prepare the ion ensemble in an isobarically pure sample. The system built up for SHIPTRAP is based on the ISOLTRAP cooler trap [Koe95a], where a cylindrical geometry of the trap electrodes is employed. Such an open geometry with an inner diameter of $\oslash_{in} = 32\,mm$ allows the transfer of ions into and out of the trap with high efficiency. In addition, it makes the necessary pumping possible to remove the buffer gas. The

Table 5.1: Components of the SHIPTRAP experiment with required pressures.

Element	pressure p_{He} [mbar]
stopping chamber	$1 \cdot 10^{2}$
extraction RFQ	$5 \cdot 10^{-1}$
buncher RFQ	$3 \cdot 10^{-2}$
transfer section	$5 \cdot 10^{-7}$
purification trap	$4 \cdot 10^{-6}$
precision trap	$1 \cdot 10^{-8}$
TOF section	$1 \cdot 10^{-8}$

Penning trap is presently being built up at GSI and is described in more details in [Sik].

Precision Penning trap

In the precision Penning trap the mass measurements via FT-MS or the TOF-method are performed. The first version for the SHIPTRAP experiment will be with a cylindrical geometry at room temperature. The inner diameter here is also $\oslash_{in} = 32\,mm$. This enables one to set up the two Penning traps as one stack of electrodes with a transfer section in between. In this way, optimized conditions for the transport of the ions from the preparation to the precision trap are guaranteed. In addition, the small opening ($\oslash = 2\,mm$) of the transfer tube between the two trapping sections provides differential pumping. This is crucial since both Penning traps are housed within the same super-conducting magnet with two homogeneous regions. Therefore the turbo molecular pump can only be placed outside the magnet to generate the necessary UHV regime for the precision Penning trap. Table 5.1 shows the foreseen pressures of the different components of the SHIPTRAP experiment.

5.2 Feasibility study

A novelty and a unique feature of the SHIPTRAP facility is the possibility to investigate transuranium nuclides which are inaccessible at ISOL-facilities. In the following a feasibility study for mass measurements at SHIPTRAP is presented. A budget for the necessary time and the expected transfer efficiencies for all involved components is shown in table 5.2. The accuracy obtained with mass measurements in a Penning trap is determined by the measurement time and the statistics. The measurement time is limited by the nuclear half-life and the statistics is limited by

Table 5.2: Budget of the time required for the manipulation of the SHIP beam and budget of the transfer efficiencies. The SHIP transfer efficiency depends on the type of reaction and here a minimum value is taken. The values marked (*) are approximations based on simulations. All other values are taken from other experimental set-ups. For the gas cell two types are listed, where the explanation is given in the text.

Element	Transfer Time	Transfer Efficiency
SHIP	$1\,\mu s$	10 %
Stopping cell (1) $(10^{-4} - 10^{-5} mbar)$	$\approx 1\,\mu s$	10 %*
Stopping cell (2) $(50 - 100 mbar)$	$\approx 10 ms$	10 %*
Extraction RFQ	$1\,ms$	80 %
Buncher RFQ	$10\,ms$	80 %
Transfer section	$50\,\mu s$	100 %*
Purification Penning Trap	$100\,ms$	100 %
Measurement Penning Trap	$500\,ms$	100 %
Time of flight section	$200\,\mu s$	100 %
Sum	$\approx 610\,ms$	0.64%

the available intensity. Therefore, specific limitations arise for exotic nuclides. An survey of *all known* transuranium nuclides is done here in order to identify possible candidates for mass measurements at SHIPTRAP.

For the half-life a limit of $T_{1/2} > 500\,ms$ is chosen because it allows one to reach a resolving power of $\Delta m/m \approx 5 \cdot 10^{-6}$, as desired to resolve isomeric states from the ground state. A second condition arises from the present mass uncertainty of the nuclides. Here a limit of δm$> 50\,keV$ is taken, which can be improved by SHIPTRAP. For example, for a mass of $A = 250\,amu$ an uncertainty of δm$= 50\,keV$ corresponds to an accuracy of $2 \cdot 10^{-7}$, which is routinely reached at ISOLTRAP.
In table 5.3 the nuclides fulfilling these two conditions are listed, together with production cross sections measured at SHIP [Kel81, Sch00] and the resulting number of nuclides at SHIPTRAP. A primary beam intensity of $I = 1\,P\mu A$, a target thickness of $350\,\mu g/cm^2$, a transfer efficiency of 10 % for SHIP and 6.4 % and for SHIPTRAP (see table 5.2) are assumed. The table is divided into three different regions which are distinguished by different recoil energies and pruduction rates. For the investigation of those nuclides different set-ups and measurement techniques are required.

Region 1: The nuclides in this region are produced in collisions of relatively light projectiles on heavy targets. A typical reaction would be ^{12}C (7.3 MeV/u) + ^{234}U (at rest) $\Rightarrow^{246}$Cf (17 keV/u). Due to the low kinetic energy of the recoil ions the entrance window of the stopping gas cell has to be very thin. Possibly a carbon foil

Table 5.3: Candidates for mass measurements at SHIPTRAP where the conditions of $T_{1/2} > 500\,ms$ and $\delta m > 50\,keV$ are fulfilled and which are produced with sufficient rates. Shown is the isotope, its half-life and mass uncertainty estimated from systematic trends [Aud95], the production cross section measured at SHIP and the expected number of ions at SHIPTRAP. For the different regions, the primary beam intensities, the transfer efficiency etc. see text.

Nuclide	$T_{1/2}$	δm [keV]	Cross section	Ions at SHIPTRAP
REGION 1				
^{239}Cm	3h	100	$12\,\mu b$	3.5/s
^{239}Bk	? s	290	$18\,\mu b$	6.5/s
^{240}Bk	5 m	159	$16\,\mu b$	6/s
^{239}Cf	39s	150	$8\,\mu b$	1/s
^{240}Cf	1 m	200	$12\,\mu b$	3.5/s
^{241}Cf	3.8 m	250	$10\,\mu b$	3/s
^{245}Cf	43.6 m	100	$370\,nb$	0.05/s
REGION 2				
^{245}Fm	4.2 s	280	$10\,nb$	0.001/s
^{246}Fm	1.1 s	200	$20\,nb$	0.002/s
^{249}Fm	2.6 m	140	$200\,nb$	0.02/s
^{250}Md	52 s	300	$10\,nb$	0.001/s
^{251}Md	4 m	200	$80\,nb$	0.01/s
^{252}Md	2.3 m	200	$800\,nb$	0.08/s
^{253}Md	6 m	210	$800\,nb$	0.08/s
^{254m}No	0.78 s	100	$500\,nb$	0.05/s
^{259}No	58 m	100	$600\,nb$	0.06/s
^{257}Rf	? s	270	$14\,nb$	0.001/s
^{259}Rf	3 s	70	$10\,nb$	0.001/s
REGION 3				
^{260}Db	1.5 s	230	$10\,nb$	0.001/s
^{261}Db	1.8 s	230	$10\,nb$	0.001/s
^{262}Db	34 s	180	$20\,nb$	0.002/s
^{263}Sg	0.9 s	70	$10\,nb$	0.001/s
^{263m}Sg	? s	120	$10\,nb$	0.001/s
^{265}Sg	20 s	100	$10\,nb$	0.001/s
^{264}Bh	740 ms	280	$100\,pb$	0.00001/s
^{265}Bh	1 s	350	$200\,pb$	0.00002/s

with $20\,\mu g/cm^2$ [Lom00] can be employed. The required gas pressure for stopping the recoil ions in the gas cell after transversing the carbon foil would be of the order of $p_{He} \approx 10^{-4}$ to $10^{-5} mbar$.

Region 2: In this case heavy ions impinge on heavy targets like ^{40}Ca (6.4 MeV/u) + ^{205}Tl (at rest) $\Rightarrow^{245}$Md (170keV/u). To stop the products a thicker window on the gas-cell is used, for example, a $100\,\mu g/cm^2$ Ni-foil. The gas pressure is $p_{He} \approx 100 mbar$.

Region 3: The stopping scenario is the same as for region 2 for a typical reaction like ^{54}Cr (5.6 MeV/u) + ^{208}Pb (at rest) $\Rightarrow^{262}$Sg (240 keV/u). The difference is that for these nuclides the production rate is so low that an extremely sensitive and non-destructive detection method like Fourier Transform Mass Spectrometry (FT-MS) has to be employed. This allows for a reduction of the required number of ions by at least a factor of 10.

5.3 Conclusion

The SHIPTRAP facility will open up the field for direct mass measurements of transuranium nuclides. Quite a number of very interesting cases were found. With accurately measured masses of, e.g., ^{257}Rf, ^{260}Db and ^{265}Sg combined with Q_α-values determined from α-decay chains originating from nuclides ^{269}110, ^{272}111 and ^{277}112 [Hof95, Hof96], the masses of the heaviest elements synthesized at SHIP could be determined directly. Other nuclides in this mass region not listed in table 5.3 are also interesting candidates for mass measurements. Here, information on the nuclear binding energy is obtained via Q_α-measurements. Direct mass measurements by SHIPTRAP are especially important for the nuclides with odd proton and/or neutron number where α-decays to excited states can not be excluded. An exact information on pairing and shell correction energies is crucial for future experiments for discovering further superheavy elements since those nuclei are only stabilized by shell effects.

Chapter 6

The ISOLTRAP experiment

6.1 Experimental set-up

The ISOLTRAP Penning trap spectrometer [Rai97, Bol96] is installed at the on-line facility ISOLDE/CERN in Geneva. Exotic nuclides are produced via proton bombardment of a thick target. The products are ionized, extracted and mass separated. The quasi-continuous beam of typically 30-60 keV is subsequently transported to the ISOLTRAP experiment.

The ISOLTRAP experiment consists of three electromagnetic traps which serve for different purposes. The first trap is used to stop, cool and transform the continuous beam into a low-energetic ion bunch. The second trap acts as an isobar separator and the third is a high-accuracy mass spectrometer. Figure 6.1 shows the set-up of the triple-trap mass spectrometer.

RFQ buncher

The first trap is a linear gas-filled radiofrequency quadrupole (RFQ) trap. The prototype of this device is described in detail in chapter 4. For the experiments presented in this study, the improved version of the RFQ structure was employed, which is described in [FHe01b]. The RFQ is sitting on a 60 kV high-voltage platform and captures the ISOLDE beam. The beam is electrostatically retarded and cooled by buffer gas to thermal temperature. Potential walls at the outer section allow one to accumulate the ions. By applying a fast pulse to the end section, the ions can be extracted as a low energetic bunched beam.

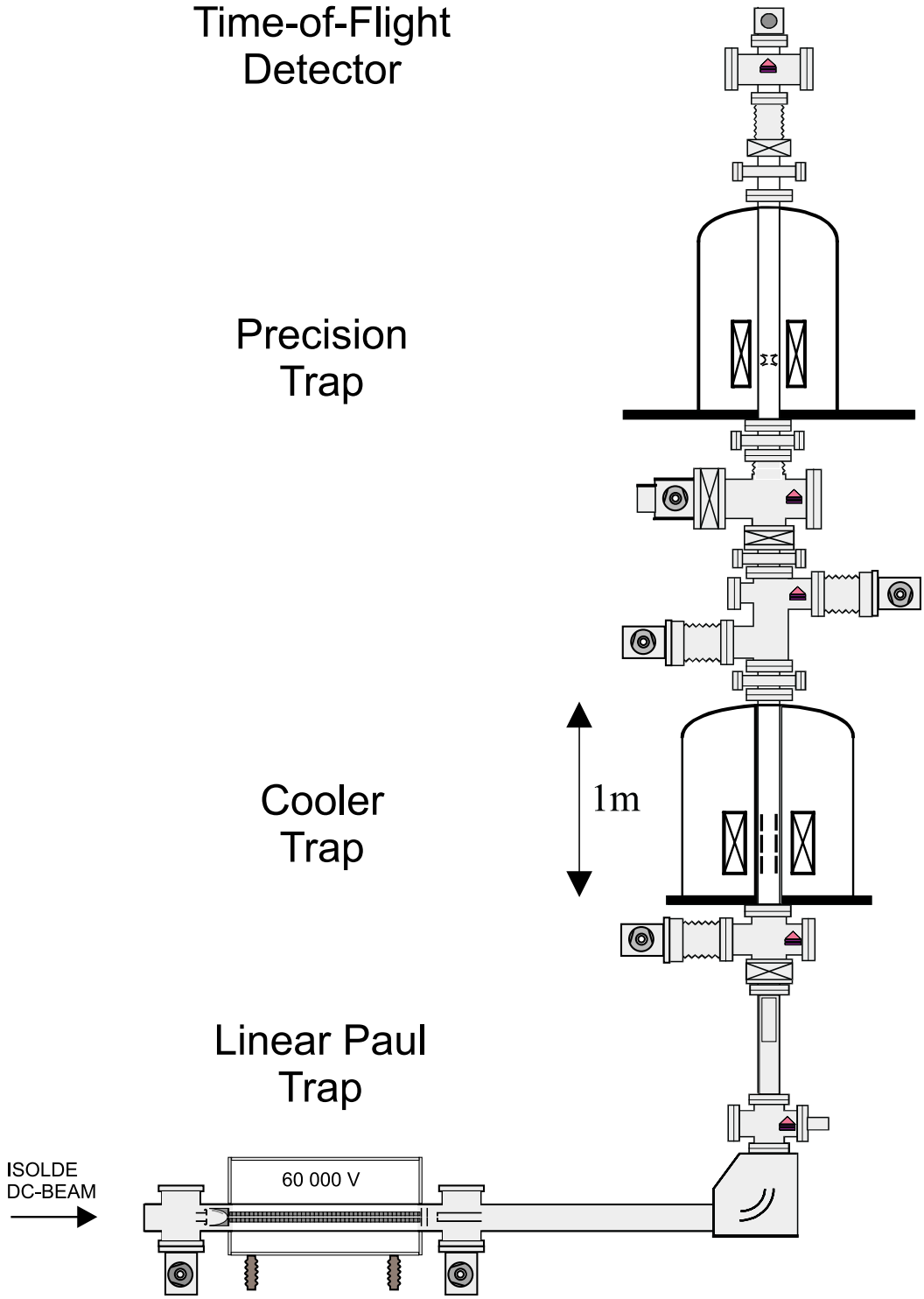

Figure 6.1: Experimental set-up of ISOLTRAP. The linear Paul trap is used for cooling and bunching of the ISOLDE beam. The cooler trap acts as an isobar separator. The high-accuracy mass measurement is performed in the precision trap by employing a time of flight technique.

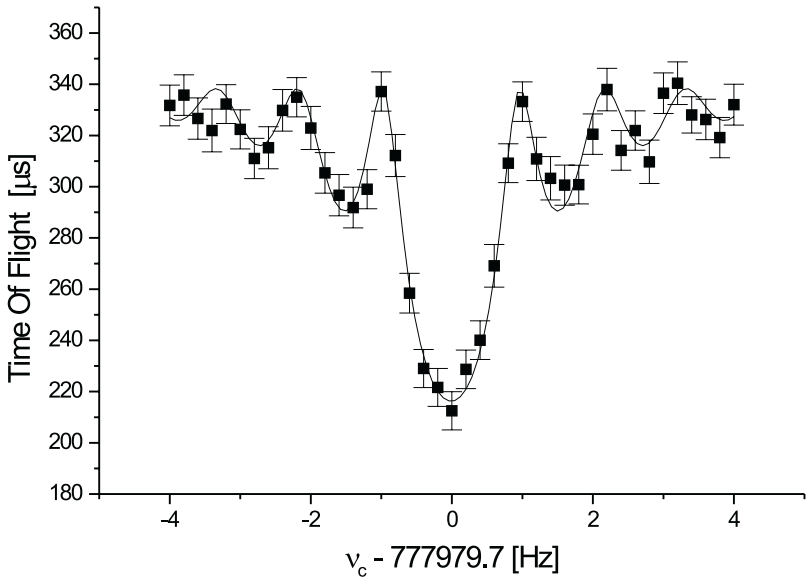

Figure 6.2: Cyclotron resonance curve for ^{117}Xe in the precision trap. Depicted is the time-of-flight of the ions from the trap to a detector as a function of applied radiofrequency. The solid line is a fit of the theoretically expected shape [Koe95b] to the experimental points.

Cooler Penning trap

The second trap is a large ($\oslash_{in} \approx 32mm$) cylindrical Penning trap located in the homogeneous field of a 4.7 T super conducting magnet. This cooler trap is used to further clean the ion sample by applying mass-selective buffer gas cooling [Rai97, Sav91]. From here the ions are ejected as a bunch and delivered to the precision trap.

Precision Penning trap

The precision trap is a hyperbolic Penning trap in a 6 T field of a second super conducting magnet. Here, the mass measurements are carried out via the TOF-MS method. Figure 6.2 shows a time-of-flight spectrum as a function of applied radiofrequency. The solid line is the theoretical expected shape of the resonance [Koe95b] fitted to the data points.

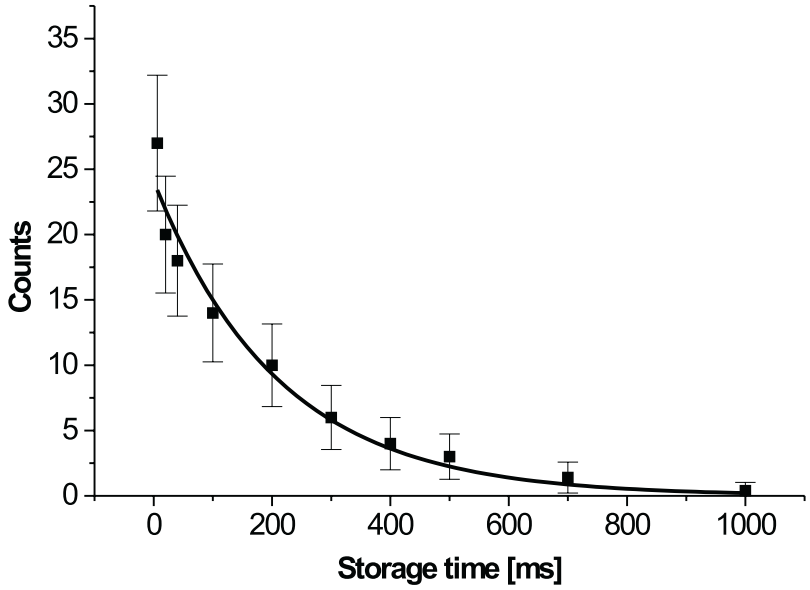

Figure 6.3: Losses of stable ^{130}Xe ions in the buncher as a function of storage time. The decay constant is $\tau = 210 \pm 24\,ms$. The loss is mainly due to charge exchange.

6.2 Beam preparation in the linear Paul trap

The measurements on noble gas isotopes reported here were only possible after the installation of the linear Paul trap . The RFQ trap is, as explained in chapter 4, filled with He buffer gas at a pressure of $p \approx 2 \cdot 10^{-2}\,mbar$. One of the critical points in this device is the loss of singly charged ions due to charge exchange processes. In the beginning of the experiments the xenon ions did not survive the transfer to the first Penning trap. Therefore the vacuum conditions has to be improved and the buffer gas further purified in order to obtain a sufficient survival time of the singly charged ions in the buncher. Figure 6.3 shows the number of extracted ions as a function of storage time in the RFQ trap. The decay constant is $\tau = 210\,ms$ which is an improvement by a factor of five to the initial conditions. This was reached by heating the RFQ system for several hours and including a cold trap into the feeding line of the buffer gas. Both measures led to a decrease of contaminants in the residual gas. Interactions with these impurities are the dominant effect for the neutralization processes of the xenon isotopes and consequent loss. The charge exchange cross section is maximized for a resonant process, with $IP_A - IP_B = \delta E = 0$, IP_A and IP_B are the ionization potentials of the ion under investigation and the neutral atom or molecule causing the charge exchange. The ionization potential of xenon is $IP_{Xe} = 12.1\,eV$. Therefore possible candidates for such a process would be: $O_2(12.1\,eV)$ or $CH_4(12.5\,eV)$. Both are present in the residual gas in vacuum

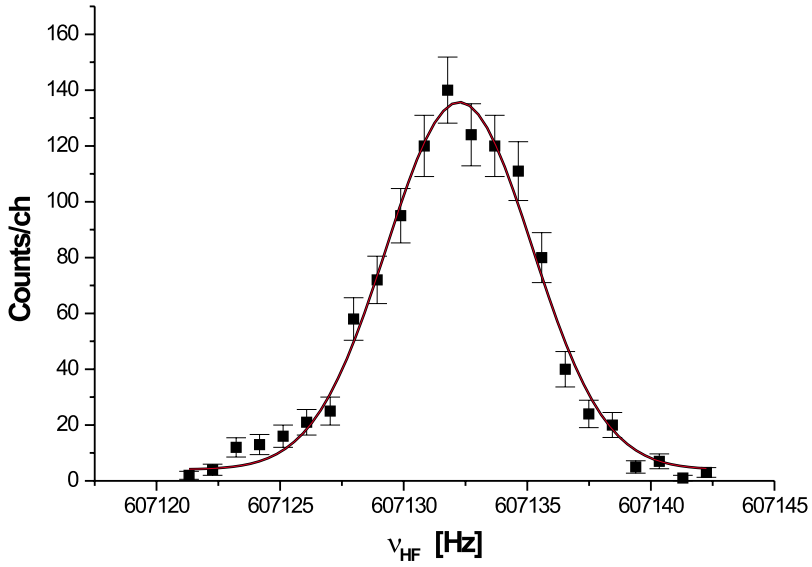

Figure 6.4: Resonance curve in the cooler trap for ^{123}Xe. The number of detected ions as a function of applied frequency is shown. The solid line is a Gauß curve fit to the data points.

systems. For further improvements of the survival time in the RFQ system, a higher level of purification of the vacuum system has to be reached.
Thermal equilibrium of xenon ions with the buffer gas is reached after $T_{cool} \approx 10\,ms$ at $p_{He} = 2 \cdot 10^{-2}\,mbar$ [FHe01b]. Therefore cooling times on the order of $10 - 20\,ms$ were used in the on-line experiments. The remaining 95 % of the ions were then ejected as a bunched beam with a ten-fold improved emittance [FHer00] at a transfer energy of $E_{trans} = 2.5\,keV$.

6.3 Obtaining an isobaric pure sample

The ISOLDE facility offers two magnetic separators. For the experiments reported here the general purpose separator (GPS) [Kug92] was used with a mass resolving power of about $R = m/\Delta m_{FWHM} \approx 1200$. Since this resolving power does not allow one to remove all isobaric contaminations, the ion cloud has to be cleaned from isobars in the gas-filled cooler Penning trap. For the xenon experiments, isobars of Cs, In, Sn, I and even molecules like InO have to be considered. A cleaning procedure was therefore performed in the cooler trap to remove impurities. By applying an RF field at ν_- with a duration of $T_{RF} = 20\,ms$ the magnetron motion of the all stored ions is excited leading to an increase of the radius of the motion. Then the centering of the investigated isotope with a duration of $T = 100\,ms$ was

started at its cyclotron frequency ω_c. In this way the resulting resolving power of $m/\delta m_{FWHM} \approx 70.000$ allows one to deliver a clean sample to the precision trap. In fig. 6.4 a cooler scan for mass $A = 123$ is shown where the number of ejected ions is depicted as a function of applied radiofrequency. The reached resolving power is $\Delta m/m = 1.5 \cdot 10^5$, allowing the separation of isobars with a mass difference of $1\,MeV$. In this a way, a clear separation of contaminants was achieved.

6.4 Measurements

The data presented on xenon masses in this work have been obtained during one on-line run. A La_2O_3 target was used coupled via a cold transfer-line to a plasma ion source. In this way the volatile isobars are drastically reduced. The target was bombarded by a 1 GeV proton beam with a current of 1 μA.

6.4.1 Efficiency

The overall efficiency of the experiment was determined by measuring the intensity of the ion beam in the focal plane of the GPS separator of ISOLDE and in front of the ISOLTRAP experiment, directly upstream of the buncher, with standard Faraday cups. These currents were compared with the number of detected ions at the time-of-flight particle detector of ISOLTRAP. For the transfer from the GPS to the experiment an efficiency of $\epsilon = 93 \pm 15\%$ was found. For the entire transfer from the separator to the TOF-detector behind the precision trap the overall efficiency was $\epsilon = 2 \cdot 10^{-4} \pm 3 \cdot 10^{-5}$, corresponding to an improvement of a factor of 1000 to the previously used set-up with the three-dimensional hyperbolic Paul trap. Detailed investigations show that the transmission could be significantly improved at three components: whereas the efficiency of the RFQ buncher is with $\epsilon \approx 25\%$ acceptable, the transfer efficiency from the RFQ to the cooler trap is only $\epsilon = 1\%$ and the transfer between the two Penning traps is $\epsilon = 10\%$. Here, investigations of necessary changes, mainly ion optics, are currently under way [Kel]. An improvement by at least a factor of 50 is expected.

6.4.2 Production yield

The production yield of the xenon isotopes was measured in the focal plane of the ISOLDE separator. For those isotopes, where the produced ion beam was too weak to be measured directly with a standard Faraday cup, the production yield was determined via the TOF detector of the precision Penning trap, assuming constant transport and detection efficiency. Figure 6.5 shows the production yields of the xenon isotopes. This can be compared to the measurements in [Klu86], where the yields are given for a $600\,MeV$ proton beam at 1 μA and which are slightly higher. This is probably due to the low ionization efficiency of the plasma ion source in

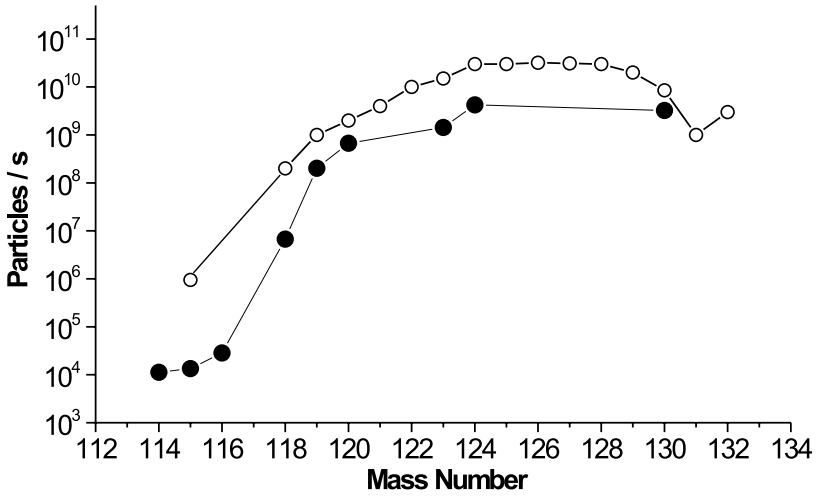

Figure 6.5: Yields for the production of Xe isotopes in the focal plane of the GPS separator of ISOLDE created by bombarding a La_2O_3 target with a 1 GeV / 1 μA proton beam. Open circles taken from [Klu86], solid points measured in this work assuming constant overall efficiency during the beam time. The connecting lines are only to guide the eye. For further explanation see text.

the actual beam time which turned out to be only about 3% [Joh99]. Usually such ion sources have an ionization efficiency of $30 - 40\%$ [Bjo86]. The yields in [Klu86] were only determined for Xe masses with $A \geq 116$, whereas the new data go further to $A = 114$. The general trend is changing here and some saturation seems to set in. This is most likely artificial, since a yield drop by approximately one order of magnitude per neutron is expected [Klu86]. A possible explanation is the change in ionization efficiency of the ion source since the data were not taken in chronological order.

6.4.3 Mass Measurement

Measurement Procedure

Mass measurements of neutron-deficient xenon isotopes with $114 \leq A \leq 124$ and $A = 130$ were carried out in this work. The measurement procedure includes the preparation in the RFQ trap (10 ms), the purification in the cooler trap (120 ms) and the measurement in the precision trap. In this last step the ions are excited for $T_{RF} = 900\,ms$ by an rf-field at a given frequency and then released from the trap towards the TOF-detector. The complete cycle is then performed 41 times (called supercycle) at equidistant rf-frequencies in the precision trap to determine the resonance (see fig. 6.2). The resonance width $\delta\nu_{FWHM}$ is, as shown before,

Table 6.1: Mass data of xenon isotopes measured by ISOLTRAP. The frequency ratio of the singly-charged xenon isotope to the reference ($^{133}Cs^{+}$) together with statistical and total error is listed in column two. In the next columns the maximum number of detected ions per cycle (#N), the number of supercycles (#S) for the time of flight measurements and in the next column the half-life is shown. The mass excess (column 6) derived from the Penning Trap (PT) frequency ratio and the literature (AME [Aud95]) value together with the corresponding absolute error are given (column 7). Values marked (#) are estimates from systematic trends [Aud95]. In the last column the difference (dev) between those two values is shown.

Nuclide	Freq.Ratio $\nu_{Ref.}/\nu$	#N	#S	$T_{1/2}$	ME PT [keV]	ME AME [keV]	dev [keV]
^{114}Xe	0.8572101482 (34) (93)	1	77	10 s	-67086 (12)	-66933 # (207#)	-153
^{115}Xe	0.8647216374 (32) (95)	1	73	18 s	-68657 (12)	-68426 # (239#)	-231
^{116}Xe	0.8722103533 (42) (109)	1	71	59 s	-73047 (13)	-72901 # (246#)	-146
^{117}Xe	0.8797253356 (19) (91)	9	19	61 s	-74185 (11)	-73994 (180)	-191
^{118}Xe	0.8872180141 (24) (93)	8	23	3.8 m	-78084 (12)	-77710 (1000)	-374
^{119}Xe	0.8947364709 (33) (91)	5	38	5.8 m	-78793 (11)	-78660 (123)	-133
^{120}Xe	0.9022333721 (40) (102)	1	52	40 m	-82170 (13)	-81832 (44)	-338
^{121}Xe	0.9097551270 (33) (100)	4	28	40.1 m	-82469 (12)	-82539 (24)	70
^{122}Xe	0.9172560020 (29) (99)	10	19	20.1 h	-85355 (12)	-85185 (87)	-169
^{123}Xe	0.9247811247 (40) (100)	4	25	2.08 h	-85237 (12)	-85260 (15)	23
^{124}Xe	0.9322857418 (22) (97)	9	25	stable	-87658 (12)	-87658 (2)	0
^{130}Xe	0.9774128763 (27) (101)	8	11	stable	-89878 (13)	-89881 (1)	3

basically equal to the inverse of the excitation period T_{RF}. For example for $A = 120$, the cyclotron frequency is $\nu_c = 760\,kHz$ in a magnetic field of $B = 6\,T$. Using an excitation time of $T_{RF} = 900\,ms$ a width of $\delta\nu_{FWHM} \approx 1.1\,Hz$ can be reached. This corresponds to a resolving power of $R \approx 10^6$, allowing mass measurements with an accuracy of $\delta m/m \approx 1 \cdot 10^{-7}$.

Frequency ratios

The cyclotron frequency is obtained by fitting the theoretical shape of the resonance [Koe95b] to the measured time-of-flight spectrum. The center frequency, the FWHM and the statistical uncertainty are deduced. The magnetic field has to be known for the conversion of the measured cyclotron frequency into an atomic mass. This is accomplished by loading stable reference ions of very well known mass into the spectrometer and determining their cyclotron frequency. Therefore the ratio of the two measured frequencies ν_{ref}/ν is the primary experimental result.

Table 6.1 shows the measured isotopes together with the frequency ratio with respect to ^{133}Cs ions. In the first brackets the statistical and in the second brackets the total error are shown. The statistical error is depending on the number of detected ions, given by the maximum number of ions detected per cycle (column 3) and the number of supercycles (column 4) per measurement. For example for ^{119}Xe the maximum number of ions detected in one cycle was 5 at 38 supercycles corresponding to a total of $5 \cdot 41 \cdot 38 = 7790$ ions. The average number of detected

ions was $\hat{N} \approx 5000$ in the experiments presented here. The expected statistical uncertainty can be approximated from the number of detected ions and the resolving power to

$$\delta\nu/\nu = (1/R) \cdot (1/\sqrt{\hat{N}}) = (1/500.000) \cdot (1/70.7) = 3 \cdot 10^{-8}. \quad (6.1)$$

The total error is given as the quadratic sum of the statistical and systematic error. The sources of systematic errors to be considered are the following:

- Frequency shifts due to magnetic field imperfections. These systematic errors are proportional to the mass difference between the reference ions and the ions under investigation. This difference is maximum δA =19 amu (for ^{114}Xe). For ISOLTRAP mass measurements this shift was investigated in [Bec97] to be $2 \cdot 10^{-9}$/amu, corresponding to a maximum shift of $4 \cdot 10^{-8}$.

- Contaminating ions of different mass in the measurement trap. Investigations at ISOLTRAP [Bol92] showed that these effects causes an error of $\delta m/m \approx 10^{-7}$ if many ones are stored simultaneously in the trap ($\geq$ 25 ions detected by the TOF detector) and if the mass difference between contaminant and investigated ions is smaller than the resonance width $\delta\nu_{FWHM}$. This was prevented by having always very few ions in the precision trap. Table 6.1 (column 3) shows the maximum number of detected ions per cycle.

- Temporal variations of the magnetic field due to changes, for example, of air pressure or ambient temperature which are not canceled out by the reference measurements. Typically a day-night shift of $\delta B/B \approx 10^{-7}$ was found [Bec97]. The measured average variation in the on-line experiments was $\delta B/B = 3 \cdot 10^{-8}$ for 11 reference measurements during the 28 hours duration of the experiment.

The total contribution of these systematic errors is below $1 \cdot 10^{-7}$. Nevertheless a conservative estimate of $1 \cdot 10^{-7}$ for systematic errors is added quadratically to the statistical error, which is on the order of $3 \cdot 10^{-8}$. Since a cycle time of $T_{cycle} \approx 1.3\,s$ was used, corresponding to a supercycle time of $T_{scycle} \approx 50\,s$, the average time for determining the frequency ratio of one isotope was $\hat{T} \approx 30\,min$.

Mass values

The conversion of the frequency ratio into an atomic mass is done by multiplying with the mass of the reference atom m_{ref}, and adding the rest mass of the electron m_e

$$m = (\nu_{ref}/\nu) \cdot m_{ref} + m_e\,. \quad (6.2)$$

Here $m_{ref} = m_{ref}(atom) - m_e$ because the atomic mass is used as reference but ions are measured. For the presented data ^{133}Cs was used as a reference mass for

three reasons: the mass was recently determined [Bra99] with a relative uncertainty of $\delta m/m = 2 \cdot 10^{-10}$; secondly, the mass difference between the reference and the xenon isotopes is small and finally, because Cs ions could be produced from an internal test ion source independently of the ISOLDE facility.

Using the frequency ratio and the known mass of the reference ion the atomic mass can be deduced. The mass excess derived is given in table 6.1 together with the final error. For comparison the mass excess from literature values [Aud95] or estimates (#) from systematics are also given.

The masses of the three isotopes ^{114}Xe, ^{115}Xe and ^{116}Xe were determined for the first time. For all other measured unstable xenon isotopes the accuracy was drastically improved. The reliability and accuracy of the ISOLTRAP measurement can be tested in the cases of the stable isotopes ^{124}Xe and ^{130}Xe, the masses of, which are known with an accuracy of about 10^{-8}. The deviation of the ISOLTRAP data from those values is $\delta m(^{124}Xe) = 1(12)\,keV$ and $\delta m(^{130}Xe) = 3(13)\,keV$, hence excellent agreement is observed.

6.5 Atomic mass evaluation and results

Within this work an atomic mass evaluation (AME) has been performed. A detailed description of such an evaluation can be found in [Aud95].

The concept is to use all available experimental mass data within a least-squares procedure of linear equations. Table 6.2 gives the result of the atomic mass evaluation. All nuclides whose mass values have changed by more than $10\,keV$ when including the new ISOLTRAP data are listed. From the 12 directly measured xenon isotopes a total number of 18 isotopes were found to be influenced notably. For the xenon isotopes some drastic shifts occurred in the mass excess values, going up to 7.7 standard deviations compared to the previous values of the AME. Figure 6.6 shows the difference of the atomic evaluation with and without the ISOLTRAP data. One clearly notices the dramatic change in accuracy reached now with the new ISOLTRAP values, which is on the order of $\delta m \approx 12\,keV$ for all measured xenon isotopes. For the isotopes $A = 114, 115$ and 116 only estimated values existed which could now be replaced by high-accuracy experimental data. It is ,however, notable that those estimated AME 95 values agree well within their (large) error bars with the now measured values. This is in contrast to previously experimentally determined masses used for AME 95, closer to the valley of stability, namely for ^{120,121,123}Xe. One notices also that most of the previous masses were too small. This can be explained by systematic errors made by determining the masses at on-line facilities, where the background could probably not be sufficiently suppressed (see below).

Table 6.2: Results of the atomic mass evaluation. The nuclides which are influenced by ISOLTRAP measurements on Xe isotopes are listed in column 1. The mass excess values from two least-squares adjustment are given in columns 2 (AME 95) and 3 (AME new) with the total error in brackets. The first adjustment AME 95 [Aud95] contains no data obtained in this work. The second adjustment AME new is including the new ISOLTRAP data The deviation between both is listed in column 4. Values marked with # are estimations from systematic trends [Aud95].

Nuclide	AME 95 [keV]	AME new [keV]	dev [keV]
^{114} Xe	-66933.0 # (207.0#)	-67086.2 (11.0)	-153.2
^{115} Xe	-68426.0 # (239.0#)	-68657.0 (12.0)	-231.0
^{116} Te	-85305.7 (92.0)	-85288.3 (95.0)	14.4
^{116} I	-77560.5 (142.6)	-77543.2 (144.6)	17.4
^{116} Xe	-72901.0 # (246.0#)	-73047.0 (13.0)	-146.0
^{117} I	-80436.5 (71.1)	-80447.1 (72.4)	-10.5
^{117} Xe	-73993.6 (179.9)	-74184.7 (11.0)	-191.1
^{117} Ba	-56952.0 # (648.0#)	-57098.0 # (600.0#)	-146.0
^{118} Xe	-77709.7 (1000.1)	-78084.7 (11.0)	-375.0
^{119} I	-83666.0 (63.4)	-83671.5 (64.8)	-5.5
^{119} Xe	-78659.9 (123.4)	-78793.0 (11.0)	-133.1
^{119} Ba	-64220.8 (1019.9)	-64595.8 (200.3)	-375.0
^{120} Xe	-81831.5 (44.0)	-82169.5 (13.0)	-338.0
^{121} Xe	-82539.3 (24.4)	-82468.9 (12.0)	70.4
^{121} Cs	-77139.3 (13.9)	-77068.9 (23.4)	70.4
^{121} Ba	-70342.5 (303.2)	-70680.6 (300.3)	-338.0
^{122} Xe	-85185.2 (87.3)	-85354.5 (12.0)	-169.3
^{123} Xe	-85259.9 (15.4)	-85245.5 (9.0)	14.4

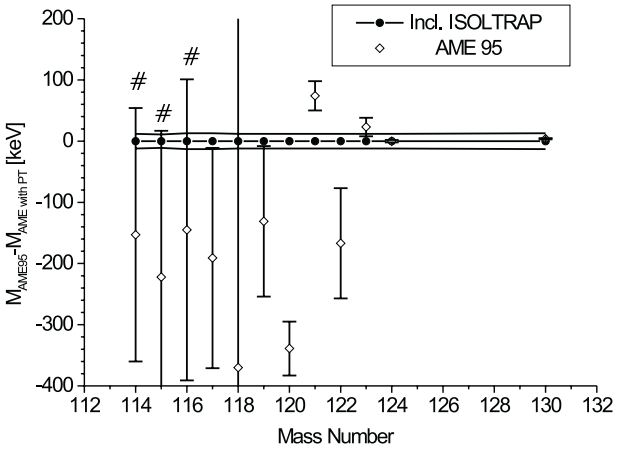

Figure 6.6: Difference between xenon mass values from the Atomic Mass Evaluation 1995 (AME 95) [Aud95] (data points with error bars) and an evaluation including the ISOLTRAP data (zero line with error band). For isotopes marked with #, masses are estimated from the extrapolation of systematic trends [Aud95].

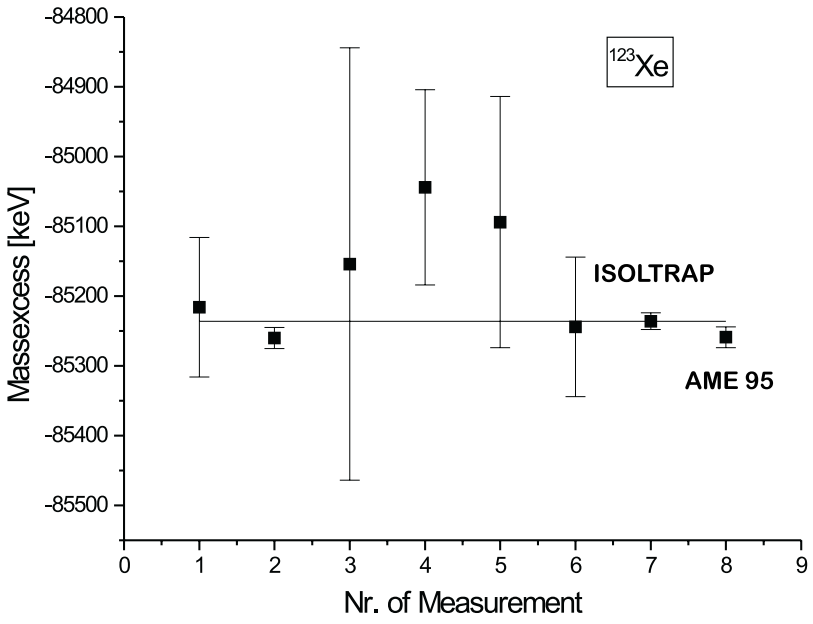

Figure 6.7: Comparison of the ISOLTRAP value for ^{123}Xe with previously measured data of the mass excess and AME 95. The horizontal line indicates mass value reported in this work. Measurement #1 [Mat75], #2 [Moo60], #3 [Wes75], #4 [Sof81], #5 [Par83], #6 [Alk93].

6.6 Discussion of the new input data set

In this section a detailed comparison between existing measurements and the new ISOLTRAP data is performed. All publications used or documented in previous atomic mass evaluations [Aud95] were taken into account. For the evaluation the available data are therein carefully checked and categorized with regard to quality or documentation. In the evaluation the values are weighted in the linear equations accordingly. However, for the new evaluation the ISOLTRAP data have basically 100% influence on the determination of the mass value in the cases of the exotic xenon nuclides.

^{123}Xe: For ^{123}Xe six previous mass measurements were used for the adjustment of the AME95 [Aud95]. All were β-endpoint determinations. The most accurate one by R.B. Moore [Moo60] (fig.6.7 #2) had the strongest influence in the AME 95 but disagrees by $1.5\,\sigma$ from the ISOLTRAP datum. R.B. Moore [Moo00] states that the original error estimation of the β-endpoint measurement was probably too small. There is also a $1.4\,\sigma$ deviation in the case of the measurement #4 shwon in 6.7. This datum is derived by K. Sofia et al. [Sof81] by a linear fit to a Fermi-Kurie plot.

The assigned error seems to be too small since it looks possible to fit linear functions to the data points leading to endpoints outside the error interval. The other values for this isotope agree well with the ISOLTRAP datum within their error bars. For the new atomic mass evaluation the value given in [Moo60] and [Sof81] are excluded from the adjustment and marked with "Well-documented data which disagree with other well-documented values".

^{122}Xe: Five endpoint measurements were performed prior to the ISOLTRAP mass measurement of which two concern the very same experiment with different corrections for the isomeric state of the mother nucleus. One of those corrections [Par83] disagrees with our datum. The documentation of this experiment, a PhD thesis of the University of California, Berkeley, by R.F. Parry was not available, therefore a judgment of the quality was not possible. A discrepancy is also found with the experiment reported by G.D. Alkhazov et al. [Alk93]. Here the technique of β-decay energy determination via γ-ray endpoints was used, where a cascade of γ-rays is summed up in a total absorption detector. For this determination it is necessary to fully understand the beta-decay strength function $S_\beta(E)$ which is not the case for this isotope. Therefore this value is disregarded for the evaluation. The other experiments agree well within the given error.

^{121}Xe: Four of the six previously performed mass measurements of this nuclide agree well with the ISOLTRAP value. All of them are β-endpoint data. Disagreement is found with a measurement of E. Beck et al. [Bec70] (fig. 6.8 #2). Very little information can be found in the original publication. The method used is the least-squares fit to the Fermi-Kurie plot, but it is not reported whether coincidences were used or in what way the calibration of the detector system was done. Another deviation from the ISOLTRAP datum is found in a measurement of K. Sofia et al. [Sof81] (fig. 6.8 #4). Looking more closely at the original publication (fig. 6.9) it is obvious that the assigned error is too small. The Fermi-Kurie plot was fitted using two different binnings and the final Q_β value is the weighted mean of the two. No information whether the background is subtracted is given, which might shift the endpoint. In the same publication the identical method applied to another nuclide, here even in γ-coincidence, leads to an error seven times larger (for $^{121}Xe : \Delta E = 20\,keV$, for $^{123}Xe : \Delta E = 140\,keV$). The two experiments of E. Beck et al. and K. Sofia et al. are now excluded from the evaluation and marked as "Well-documented data which disagree with other well-documented values".

^{120}Xe: For ^{120}Xe five mass measurements were carried out before. One of them was exclusively (fig. 6.10 #1) used for the AME95. However the size of the error was modified from the original publication of F. Münnich et al. [Mue74], where the assigned error is $200\,keV$, to $40\,keV$ for AME 95. The Q_β-value is determined in this measurement by the EC/β^+-ratio measurement. This is based on various

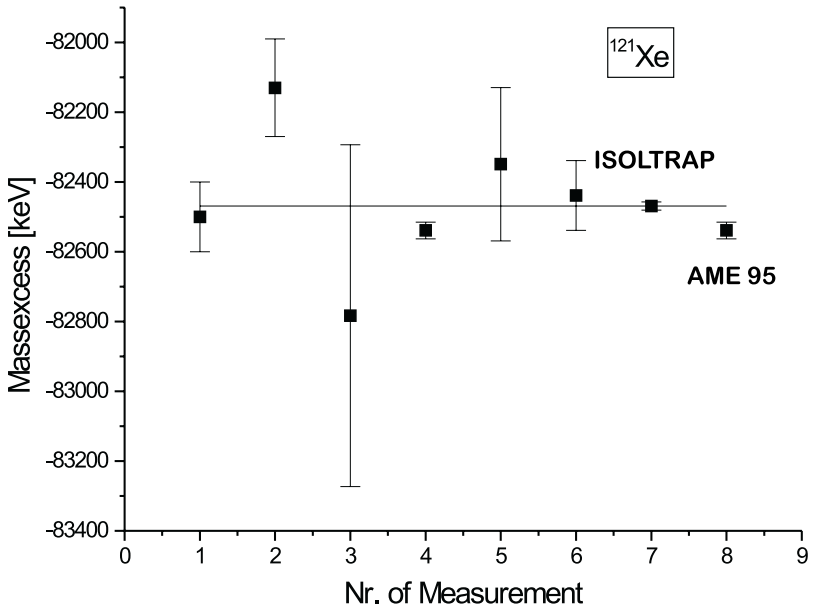

Figure 6.8: Comparison of the ISOLTRAP value for ^{121}Xe with previously measured data of the mass excess. The horizontal line indicates the mass value determined by ISOLTRAP. Measurement #1 [Sof81], #2 [Bec70], #3 [Moo60], #4 [Wes75], #5 [Par83].

assumptions such that energy and parity of the ground state of ^{120}I are well known and that there is no feeding by other positrons of this state. Further discussion with the authors of the AME [Wap00] led to an exclusion of this value, due to uncertainties in those assumptions. The masses of the measurements #3 and #5 agree well within error bars. The error in the original publication seems to be too small for [Bat76] (fig. 6.10 value #2) where the value is derived by a linear fit to a Fermi-Kurie plot. For the other disagreeing value (#4) no documentation is available [Par83].

^{119}Xe: The mass of this isotope given in the atomic mass evaluation of 1995 is the weighted average of two measurements [Bec70] and [Par83]. Both values and the average agree well within the error bar with the ISOLTRAP datum.

^{118}Xe: The value of ISOLTRAP is in agreement with the measured value [D'A76] taken for AME95. Another measurement [Bec70] with smaller errors is excluded and marked: "Data from incomplete reports, at variance with other data or with systematics" in the documentation of the new AME, due to little information given in the publication.

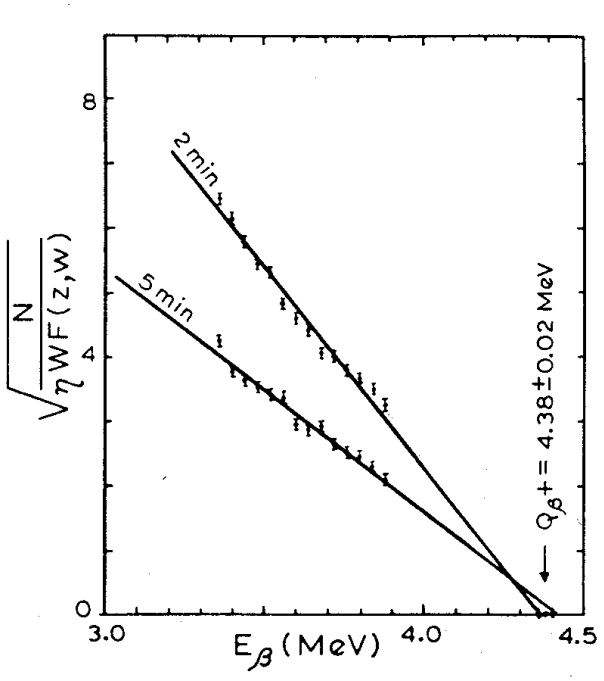

Figure 6.9: Fermi-Kurie plot for ^{121}Xe [Sof81].

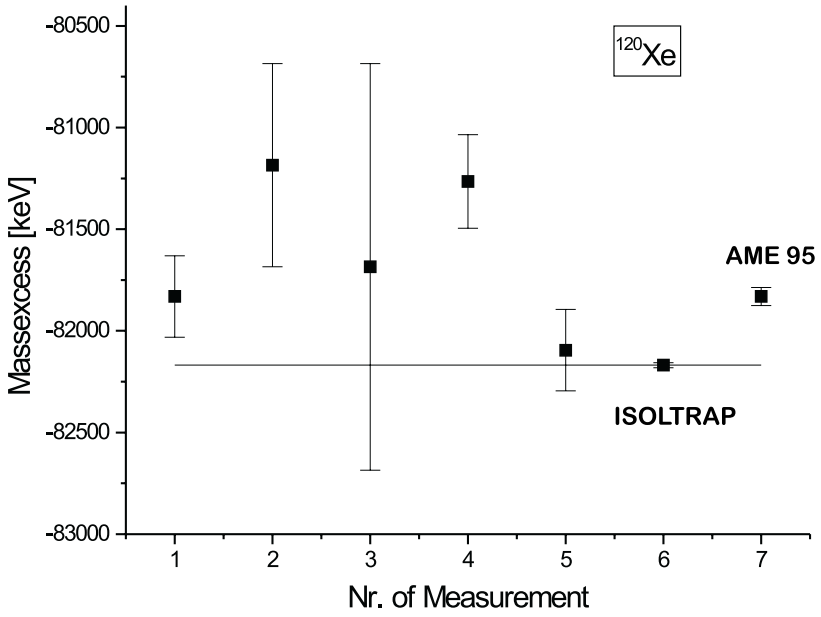

Figure 6.10: Comparison of the ISOLTRAP value for ^{120}Xe with previously measured data of the mass excess. The horizontal line indicates the mass value reported in this work. Measurement #1 [Mue74], #2 [Alk93], #3 [D'A78], #4 [Bat76], #5 [Par83].

^{117}Xe: Two measurements of the mass of this isotope were performed previously. The ISOLTRAP datum agrees well with the data of P. Hornshøj et al. [Hor72] and R.S. Lee et al. [Lee85].

^{116}Xe: In the AME 95 an estimate of the mass from systematic trends is given. However, a measurement by G.M Gowdy et al. is documented [Gow76], where the value is derived from the difference of two Fermi-Kurie plots. For the AME 95 this value was regarded as differing too much from the systematic trend and therefore marked as "Nuclei for which masses estimated from systematic trends are thought better than the experimental masses". Agreement of this experimental datum with the ISOLTRAP datum is found within the estimated uncertainty of the extrapolation.

^{115}Xe: For the isotope ^{115}Xe there were two values documented [D'A78, Bog77] in the AME 95, but the given mass is an estimation from systematic trends. The experimental masses were regarded as not reliable enough as in the case of ^{116}Xe. The ISOLTRAP value agrees well with these measurements and the value derived from systematic trends. By looking at the original publication of J. D'Auria et al. [D'A78] it seemed that the datum used in AME 95 is rather the prediction from systematics in their work than their measured value. For the new documentation this is corrected.

^{114}Xe: No measurements existed for this isotope. The mass reported in this work is within the expectation from systematic trends.

6.7 Discussion of the results of the new atomic mass evaluation

6.7.1 Two-neutron separation energies

The two-neutron separation energy is defined as the difference in binding energy ($\mathrm{E}^B(Z,N)$) for two isotopes differing in neutron number N by 2

$$S_{2n}(Z,N) = E^B(Z,N) - E^B(Z,N-2). \tag{6.3}$$

The two-neutron separation energy allows one to recognize changes in the nuclear structure without the complication of the huge odd-even effects caused by pairing. Figure 6.14 shows the S_{2n} as a function of mass number A for the measured xenon chain and neighboring elements where changes occurred due to ISOLTRAP data. This is the case for 23 S_{2n}-values where at least one datum of the S_{2n} input was changed. The new values are plotted as solid points, the previous data taken from the AME 95 [Aud95] as open circles.

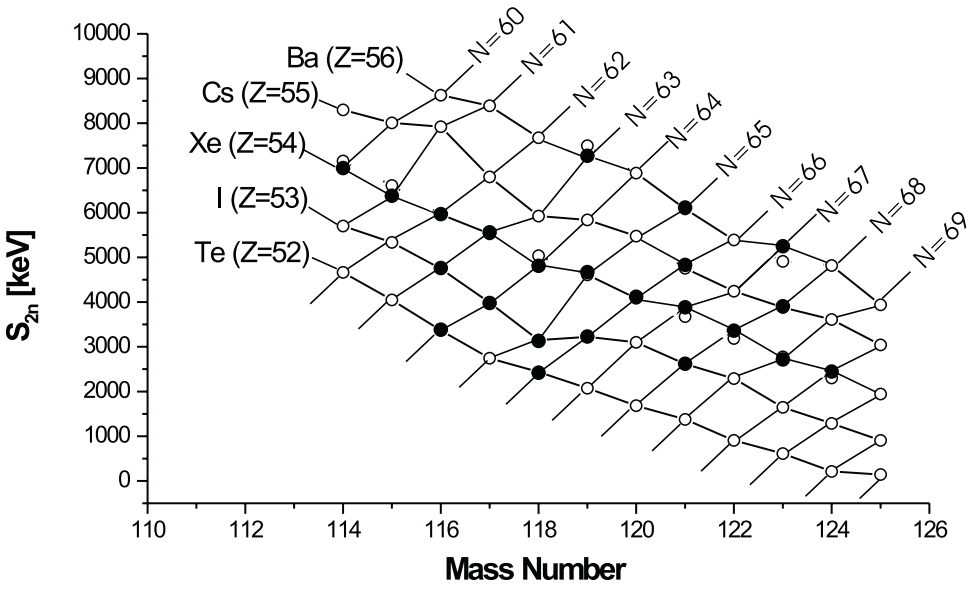

Figure 6.11: Two-neutron separation energy S_{2n} as a function of mass number A. Filled circles show the new values, open circles old data calculated from AME [Aud95]. No error bars are shown.

Generally, a very smooth behaviour of the two-neutron separation energies (especially for the nuclides with even proton number) is found in this region of the chart of nuclides, indicating the absence of any drastic nuclear structure effects in those neutron mid-shell nuclides. However at the neighboring chains of xenon some local irregularities appear like in the case of ^{116}Cs at $A = 116$. The binding energy for ^{116}Cs isotope is experimentally known with an uncertainty of $\delta m = 351\,keV$. The corresponding value of ^{114}Cs is an estimate from systematics with $\delta m = 305\,keV$. That might be also the reason for the deviation at ^{118}Cs at $A = 118$ for which the ^{116}Cs-datum is also used. As a consequence, the mass of ^{116}Cs should be experimentally checked with good accuracy.

Another case for such a clear deviation from the general trend is found for iodine isotopes at $A = 118$. The experimental uncertainty of the two isotopes is $\delta m = 144\,keV$ and $\delta m = 72\,keV$, respectively. Again, better precision would be desired, to discriminate between an error in the input data or a nuclear structure effect.

6.7.2 Comparing the experimental results with mass formulae

There are a large number of for mass models. But it is necessary to compare the models to experimental results for further development. This is required to improve, for example, the predictive power of nuclear models for regions very far from stability, where the knowledge of masses is required as, for example, to calculate the pat of the r-process. Other approaches even need the experimental results to build a set of parameters with which the mass landscape is then described an extrapolated into unknown regions. A recent overview of those models can be found in [Pat99]. A comparison of five different models is carried out within this work. The graphs in fig. 6.12 and fig. 6.13 show the difference between experimental and theoretical values.

The model of Pearson et al. [Abo92], (top) based upon an extended Thomas-Fermi-Strutinski ansatz, includes a Skyrme term to describe the interaction between the nucleons. The contributions accounting for deformation effects seem to be overestimated in the region around $A = 121$, where no changes in the experimental deformation values are observed. Here, a rather smooth behaviour would be expected. The root-mean-squares (RMS) deviation for the xenon isotopes in the mass region $114 \leq A \leq 136$ is $\Delta m(RMS) = 301\,\mathrm{keV}$.

The mass values by Duflo and Zuker [Duf95] (middle) are derived by a microscopic mass model. The odd-even staggering is clearly overestimated in this mass formula. The masses near the closed neutron shell $N = 82\,(A = 136)$ are well reproduced. The deviation found is $\Delta m(RMS) = 413\,keV$.

For the macroscopic microscopic model of Möller and Nix [Moe95] (bottom) the odd-even staggering is also overestimated. The overall trend is best described by this model especially in the mid-shell nuclei, wheras the shell-closure at $N = 82$ is not well described. The RMS-difference for this model is $\Delta m(RMS) = 253\,keV$.

In the top graph of fig. 6.13 the model of Dobaczewski et al. [Dob84] is used for comparison. A self consistent Hartree-Fock-Bogoliubov (HFB) ansatz of spherical nuclei with a Skyrme force is employed. This model properly describes nuclear radii and shell effects, but has apparently a lack of predictive power for mass values. This is reflected in the rather large differences found in the comparison of theoretical and experimental values of the ground-state masses of $\Delta m(RMS) = 5410\,keV$.

As a more recent model the one by Tachibana et al. [Kou00], is used in the lower graph of fig. 6.13. This is also a macroscopic microscopic model, where the general trend is covered by the macroscopic part and corrections are made by shell energies in a single particle picture. The RMS-difference for this model is

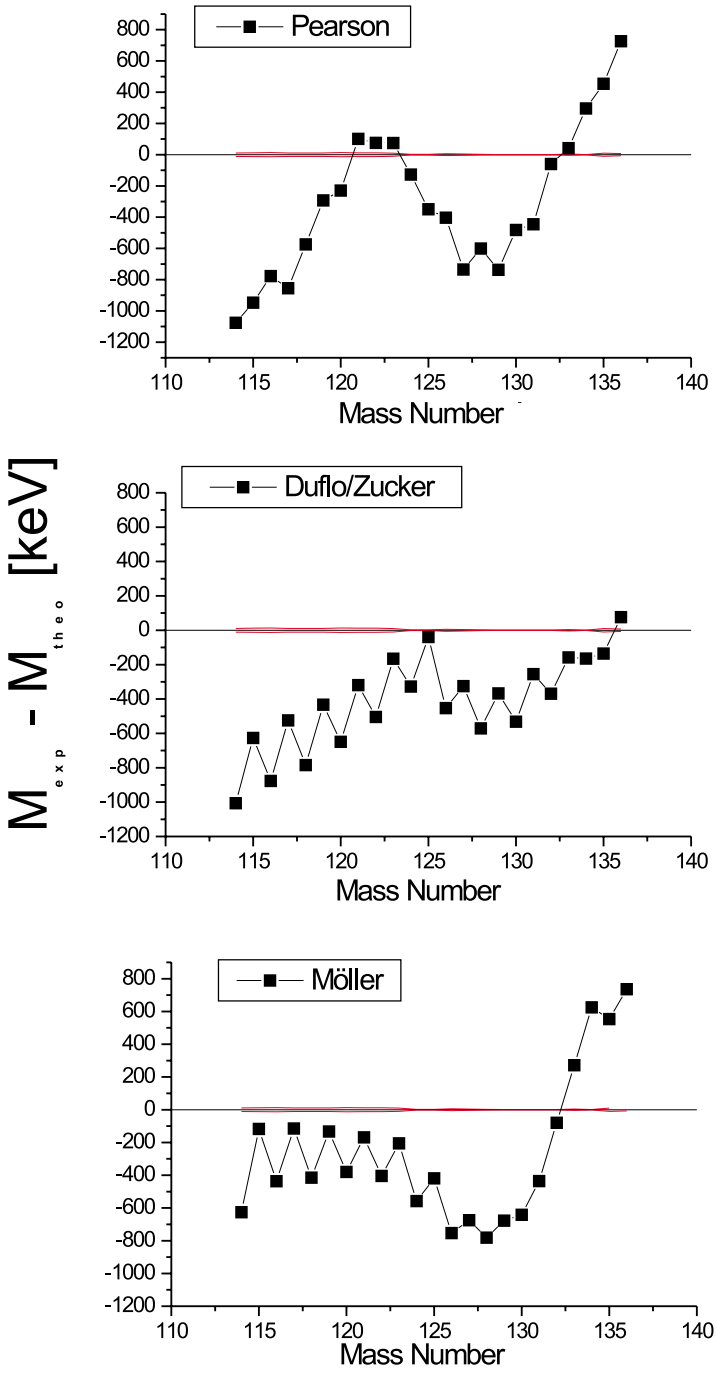

Figure 6.12: Comparison of the new AME mass values (shown as zeroline with an errorband) with predictions of different mass models for some xenon isotopes.

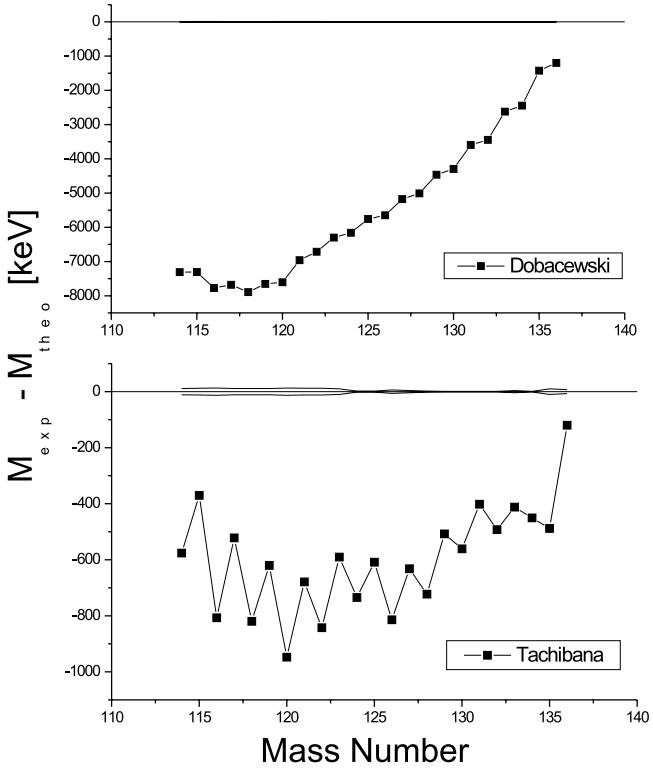

Figure 6.13: Difference between predictions of two mass models and the new AME mass values for some xenon isotopes.

$\Delta m(RMS) = 596\,keV$.

6.7.3 Deformation effects within the xenon isobaric chain

Figure 6.14 shows the two-neutron separation energies for xenon isotopes with $114 \leq A \leq 141$. Here, S_{2n} is reduced by a linear function, in order to pronounce more clearly nuclear shape effects. Besides the strong discontinuity observed at the shell closure at $N = 82$, a smoothly varying two-neutron separation energy is observed in the region $58 \leq A \leq 82$ with a slight minimum around mid-shell. This is obviously due to a nuclear deformation effect.

Information on the quadrupole deformation can also be obtained, for example, from isotope shift measurements deduced by collinear laser spectroscopy [Bor89]. Figure 6.14 shows the change in the mean-squared charge radii $\delta < r^2 >^{136,A}$ as a function of neutron number N or mass number A. The difference is taken with respect to the isotope $A = 136$ with a closed shell, which is considered to have spherical shape. Shown are also equideformaton lines of $< \beta^2 >^{1/2}$-values at 0.1,

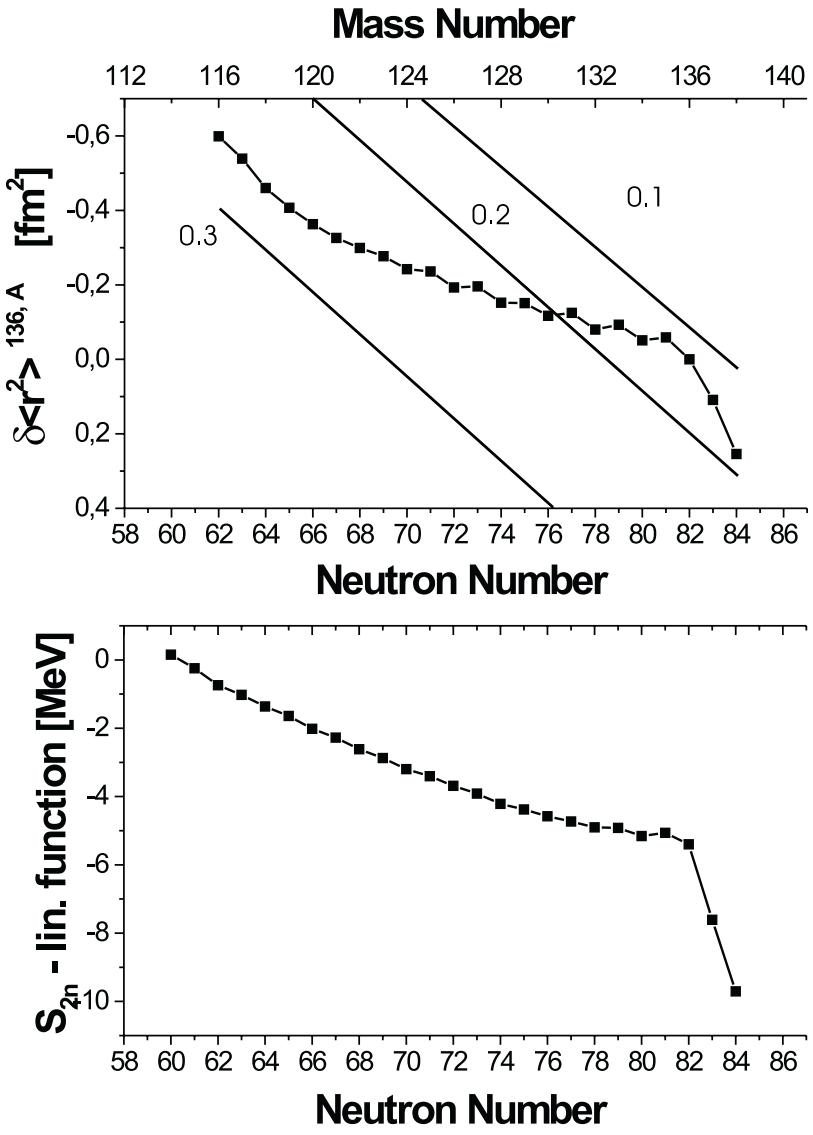

Figure 6.14: Top: Changes in the mean charge-squared radii of xenon isotopes relative to ^{136}Xe (taken from [Bor89]). Shown are also equideformation lines of $< \beta^2 >^{1/2}$-values at 0.1, 0.2 and 0.3 as calculated from the droplet model [Moe88]. Bottom: Reduced two-neutron separation energies for xenon isotopes derived from the experimental mass data presented in this work and AME.

0.2 and 0.3 as calculated by use of the droplet model [Moe88]. Comparing the reduced S_{2n} values with $\delta < r^2 >$, both graphs show a similar smooth trend from the very neutron-deficient isotopes towards the shell closure at $N = 82$ where a drastic change appears. In both cases a weak odd-even staggering is visible. The gradually increasing deformation for neutron numbers below $N = 82$ as obtained from the isotope shift data is obviously reflected in the bump of the S_{2n} values. No signature for a sudden transition appears, neither in the isotope shift nor in the mass data. This is consistent with the description of a 'soft'-core by T.R. Werner and J. Dudek [Wer95]. However, the signature of shape coexistence by a particle-hole intruder configuration is not reflected. This is one of the suggested models for the enhanced $E0$ and $E2$ transition rates in the midshell Xe isotopes, particularly at $N = 64, 66$ and 68, found by P.F. Mantica and W.B. Walters [Man96]. Also, shape coexistence is often associated with isomerism [Woo99, Bec99], which is excluded in our measurements due to the high resolving power of the spectrometer.

6.8 Conclusion

The xenon isotopes with $123 \geq A \geq 114$ have been directly measured for the first time using the ISOLTRAP triple trap spectrometer. The experimental precision could be increased drastically and is now $\delta m \approx 12\,keV$ for all nuclei investigated. For the isotopes ^{114,115,116}Xe values estimated from systematic trends were previously used in the tables of the AME. This could now be replaced by high-accuracy experimental data.

An atomic mass evaluation was performed and differences to the existing data were found going up to several standard deviations. These conflicts were discussed in detail and could be solved. The new direct and indirect mass results are used to describe the mass landscape in the S_{2n}-picture. The measured xenon isotopes smoothly follow the general trend. Other chains show local deviations due to large experimental uncertainties. This could basically be overcome with the present ISOLTRAP set-up. Isotopes like ^{116}Cs or ^{114}Cs with half-lives $T_{1/2} = 700\,ms$ and $T_{1/2} = 570\,ms$ are now within reach of the experiment. The comparison with theoretical mass models clearly shows that experimental values are crucially needed for cross checking the theoretical predictions. Furthermore, the experimental data are required to improve the models and reach better predictive power for nuclides further away from the valley of stability. A comparison of the reduced S_{2n}-values with changes in the mean-square charge radii shows the same trends in nuclear structure.

The new RFQ linear cooler and buncher allowed for the first time mass measurements on a chain of noble gases. Improvements of the vacuum system and the gas-feeding line extended the survival time of xenon isotopes in the buncher to $\tau = 210\,ms$. For the overall experimental efficiency a value of $\epsilon = 2 \cdot 10^{-4}$ was found.

Investigations indicate where losses occur. The transfer efficiency will be improved to a total efficiency is $\epsilon \approx 1\%$ by optimization of ion optics.

Chapter 7

Summary and Outlook

In this work the possible usage of linear Paul traps as cooler and buncher for mass separated exotic beams was investigated. Simulations were carried out in order to determine the requirements for such devices. Two RFQ structures were designed, built and commissioned. For the first time such linear gas-filled Paul traps were operated with an additional longitudinal trapping potential. The experience gained with the prototype for ISOLTRAP led to further developments, resulting in the optimized design of the SHIPTRAP and the new ISOLTRAP buncher. The latter one is now installed and first physics experiments were performed successfully.

Within the scope of this work mass measurements of a chain of noble gas isotopes were performed for the first time. The masses of $^{114-124,130}$Xe were measured with a typical accuracy of $\delta m \approx 12\,keV$. This is a tremendous improvement for the exotic nuclides of up to a factor of almost 100. For the cases of ^{114,115,116}Xe only values estimated from systematics were used in the mass tables which could now be replaced by experimental ones. Experiments on ^{114}Xe could be performed for the first time at ISOLDE, due to the enhanced efficiency of the RFQ cooler and buncher, as compared to the previous ISOLTRAP set-up

Within the work presented here an atomic mass evaluation was carried out and the results were discussed. Discrepancies with previous experimental mass results were found, with up to 7.7 standard deviations. These differences were discussed and solved. The two-neutron separation energy changed in 23 cases. The mass surface in this region was found to exhibit a very smooth behaviour except for two cases. For those the experimental uncertainties are too large to identify nuclear effects. Here new and better data are desirable. A comparison of two-neutron separation energies with laser spectroscopy data of charge radii was carried out. The S_{2N}-values as well as the isotopic shift data show a very similar trend caused by increasing nuclear deformation as one goes away from the neutron shell-closure at $N = 82$ corresponding to $A = 136$ for xenon. However, as in the case of charge radii no fingerprint of shape coexistence is observed.

The SHIPTRAP experiment is presently being set up and will become operational winter 2001. First on-line tests are foreseen in spring/summer 2002. A survey of candidates for first mass measurements of transuranium nuclides with SHIPTRAP was carried out. More than 25 nuclides were identified where SHIPTRAP could be used to improve the mass data considerably. Moreover, systematic mass measurements will be carried out with SHIPTRAP, like the nuclides around ^{100}Sn.

Measurements in Penning traps are the most precise way to determine the atomic mass of exotic nuclides. Due to the new technical developments, mainly the RFQ cooler and buncher, a new class of experiments becomes possible which was inaccessible for example because of lack of efficiency.

The two Penning trap experiments ISOLTRAP and SHIPTRAP will have complementary mass measurement programs because of the different production facilities they are coupled to. The next cases to be measured with ISOLTRAP will be placed further away from the value of stability, in the very neutron deficient region. SHIPTRAP will concentrate on very heavy systems ($A \geq 230$), but also on the heavy ($A \geq 80$) $N = Z$ regions. These mass measurements will improve our knowledge of nuclear properties at the borders of the chart of nuclides and will allow to develop better nuclear models.

Bibliography

[Abo89] Y. Aboussir et al., *At. Data Nucl. Data Tables* **61**, 127 (1989).

[Abo92] Y. Aboussir et al., *Nucl. Phys. A* **549**, 155 (1992).

[Ade99] E.G. Adelberger et al., *Phys. Rev. Lett.* **83**, 1299 (1999).

[Alk93] G.D. Alkazov et al., *Z. Phys. A* **344**, 425 (1993)

[Ame99] F. Ames et al., *Nucl. Phys. A* **651**, 3 (1999).

[Ars64] F.M. Arscott, *Periodic Differential Equations*, Macmillian (1964).

[Aud95] G. Audi and A.H. Wapstra, *Nucl. Phys. A* **595**, 409 (1995).

[Bat76] T. Batsch et al.,in Proc. Int. Conf. on the Properties of Nuclei Far From the Region of Beta-Stability, Cargese, 1976, CERN 76-33, Vol.1, p.106 (1976).

[Bec97] D. Beck et al., *Nucl. Inst. Meth. B* **126**, 374 (1997).

[Bec] D. Beck et al., *Euro. J. Phys.* sent for publication.

[Bec70] E. Beck et al.,in Proc. Int. Conf. on the Properties of Nuclei Far From the Region of Beta-Stability, Lysin, 1970, CERN 70-30, Vol.1, p.353 (1970).

[Bec99] F. Becker et al., *Eur. Phys. J. A* **4**, 103 (1999).

[Bla98] K. Baum et al., *Int. J. Mass Spectrom.* **202**, 81 (2000).

[Bjo86] T. Bjornstat et al., *Phycsica Scripta* **34**, 578 (1986).

[Bla98] K. Blaum, Diploma Thesis, University of Mainz, Germany, 1998.

[Bog77] D.D. Bogdanov et al., *Phys. Lett. A* **71**, 67 (1977).

[Bol89] G. Bollen, PhD Thesis, University of Mainz, Germany, 1989.

[Bol90] G. Bollen et al., *J. Appl. Phys.* **68**, 4355 (1990).

[Bol92] G. Bollen et al., *Phys. Rev. C* **46**, R2140 (1992).

[Bol96] G. Bollen et al., *Nucl. Instr. Meth. A* **368**, 675 (1996).

[Bor89] W. Borchers, Ph.D. thesis, University of Mainz, Germany, 1989.

[Bra99] M.P. Bradley et al., *Phys. Rev. Lett.* **83**, 4510 (1999).

[Bro86] L.S. Brown and G. Gabrielse, *Rev. Mod. Phys.* **58**, 233 (1986).

[Car72] J.O Carrico. *Dynamical Mass Spectroscopy* **3**,1 (1972).

[Com86] M.B. Comisarow and N.M.M. Nibbering, *Inter. J. Mass. Spec. Ion. Pro.* Special Issue (1986).

[D'A76] J.M. D'Auria et al.,in Proc. Int. Conf. on the Properties of Nuclei Far From the Region of Beta-Stability, Cargese, 1976, CERN 76-33, Vol.1, p.100 (1976).

[D'A78] J.M. D'Auria et al., *Nucl. Phys. A* **301**, 397 (1978).

[Daw95] P.H. Dawson *Quadrupole mass spectrometry and its applications*, American Institute of Physics (1995).

[Day54] I.E. Dayton et al., *Rev. Sci. Instrum.* **25**, 485 (1954).

[Deh67] H.G. Dehmelt,*Adv.At. Mol Phys.* **3**, 53 (1967).

[Den71] D.R. Denision, *J. Vac. Sci. Technol.* **8**,266 (1971).

[Dil99] J. Dilling et al., *Hyperfine Interactions* **127**, 491 (1999).

[Dob84] J. Dobaczewski et al., *Nucl. Phys. A* **422**, 103 (1984).

[Duf95] J. Duflo and A.P. Zucker, *Phys. Rev. C* **52**, R23 (1995).

[Duf97] J. Duflo et al., data obtainable from:`www-csnsm.in2p3f.fr/amdc/amdcuk.html`.

[VDy87] R. S. Van Dyck et al., *Phys. Rev. Lett.* **59**, 26 (1987).

[Ell78] H.W. Ellis et al.,*At. Data and Nucl. Data. Tables* **22**, 179 (1978).

[Eng00] O. Engels et al., conference proceedings APAC 2000, *Hyperfine Interactions*, in preparation.

[Gab95] G. Gabrielse et al., *Phys. Rev. Lett* **74**, 3544 (1995).

[Gei95] H.Geissel et al., *Annu. Rev. Nuc. Part. Sci.* **45**, 163 (1995).

[Gow76] G.M. Gowdy et al., *Phys. Rev. C* **13**, 1601 (1976).

[Gos95] P.K. Ghosh, *Ion traps*, Oxford University Press, 1995.

[Grä80] G.Gräff et al., *Z.Phys A* **297**, 35 (1980).

[Gua95] S. Guang and A.G. Marshall, *Inter. J. Mass. Spec. Ion. Pro.* **146/147**, 261 (1995).

[FHer00] F. Herfurth et al., *Nucl.Instr.Meth.* (to be published).

[FHe01a] F. Herfurth et al., submitted to *Phys. Rev. Lett.*

[FHe01b] F. Herfurth, PhD Thesis, University of Heidelberg, Germany, in preparation.

[NHe00] N. Hermanspahn et al., *Phys. Rev. Lett.* **84**, 427 (2000).

[Hof95] S. Hofmann et al., *Z.Phys.* A **350**, 281 (1995).

[Hof96] S. Hofmann et al., *Z.Phys.* A **354**, 229 (1996).

[Hor72] P. Hornshøj et al., *Nucl. Phys. A* **187**, 599 (1972).

[Hor91] P. Horrowitz and W. Hill, *The art of electronic*, Cambridge University Press, 2nd edition 1991.

[Joh99] O.C. Johnson, private communication.

[Kel81] J.G. Keller, Diploma Thesis, Technische Hochschule Darmstadt, Germany, 1981, and references therin.

[Kel98] A.G. Kellerbauer, M.Sc., McGill University, Motreal, Canada, 1998.

[Kel] A.G. Kellerbauer, PhD Thesis, McGill University, Motreal, Canada, in preparation.

[Kim97] T. Kim, PhD Thesis, McGill University, Montreal, Canada, 1997.

[Klu86] ISOLDE User's Guide, ed. H.-J. Kluge, *CERN* 86-05, (1986).

[Koe95a] M. König, PhD Thesis, University of Mainz, Germany, 1995.

[Koe95b] M. König et al., *Int. J. Mass. Spectr. Ion. Proc.* **142**, 95 (1995).

[Kou00] H. Koura et al., *Nucl. Phys. A* **674**, 47 (2000).

[Kre91] M. Kretzschmar, *Euro. J. Phys.* **12**, 240 (1991).

[Kug92] E. Kugler et al., *Nucl. Instr. Meth. B* **70**, 41 (1992).

[Lee71] G.E. Lee-Whiting and L. Yamazaki. *Nucl. Instr. Meth.* **94**, 319 (1971).

[Lee85] R.S. Lee et al., *Phys. Rev. C* **32**, 277 (1985).

[Let97] J. Lettry et al., *Nucl. Instr. Meth. B* **126**, 130 (1997).

[Lom00] B. Lommel, private communication.

[Lun92] M.D.N. Lunney, PhD Thesis, McGill University, Montreal, Canada, 1992.

[Lun99] M.D. Lunney and R.B. Moore, *Int. J. Mass Spectrom.* **190**, 153 (1999).

[Mai99] M. Maier, Diploma Thesis, University of Heidelberg, Germany, 1999.

[Mai00] M. Maier et al., conference proceedings APAC 2000, *Hyperfine Interactions*, submitted.

[Man96] P.F. Mantinca and W.B. Walters, *Phys. Rev. C* **53**, R2586 (1996).

[Mar00] G. Marx et al., conference proceedings APAC 2000, *Hyperfine Interactions* (2000) submitted.

[Mat75] H. B. Mathur et al., *Phys. Rev. A* **96**, 126 (1975).

[Mee53] J.M. Meek and J.D.Craggs, *Electrical Breakdown of gases*, Oxford Publishing, 1953.

[Moe88] P. Möller et al., *At. Data Nucl. Data Tables* **39**, 225 (1988).

[Moe95] P. Möller et al., *At. Data Nucl. Data Tables* **59**, 185 (1995).

[Moo60] R.B. Moore, *Bulletin of the Am. Phys. Soc.* p.68 (1960).

[Moo00] R.B. Moore, private communication.

[Mue74] F. Münnich et al., *Nucl. Phys. A* **224**, 437 (1974).

[Mue79] G. Münzenberg et al.,*Nucl. Instr. Meth.* **161**, 65 (1979).

[Mun95] F. Muntean, *Inter. J. Mass. Spec. Ion. Pro.* **151**, 223 (1995).

[Neu] J. Neumayr, PhD Thesis, University of Munich, Germany, in preparation.

[Ott89] E.W. Otten in. *Treatise on heavy-ion science, Vol. 8*, ed. D.A. Bromley, Plenum Publishing Coperation, p.535 (1989).

[Pau53] W. Paul and H. Steinwedel, *Z. Naturforschung* **8a**, 448 (1953).

[Pau89] W. Paul, *Rev. Mod. Phys.* **62**, 531 (1989).

[Par83] R.F. Parry, Ph.D. thesis, University of California at Berkeley, USA, 1983.

[Pat91] Z. Patyk and A. Sobiczewski, *Nucl.Phys. A* **533**, 132 (1991).

[Pat99] Z. Patyk et al., *Phys. Rev. A* **59**, 704 (1999).

[Rai97] H. Raimbault-Hartmann et al., *Nucl. Inst. Meth. B* **126**, 378 (1997).

[Rod] D. Rodrıguez-Rubiales, University of Valencia, Spain, in preparation.

[Zar00] F. Sarazin et al., *Phys. Rev. Lett.* **84**, 5062 (2000).

[Sav91] G. Savard et al., *Phys. Lett. A* **158**, 247 (1991).

[Sav00] G. Savard et al., conference proceedings APAC 2000, *Hyperfine Interactions*, submitted.

[Sch00] M. Schädel, private communication.

[Sch98] S. Schwarz, PhD Thesis University of Mainz, Germany, 1998.

[Sch01] S. Schwarz et al., submitted to *Phys. Rev. A*

[Sik] G. Sikler, PhD Thesis, University of Heidelberg, Germany, in preparation.

[S3D00] SIMION 3D Version 7.0, D.A. Dahl, INEEL, Idaho Falls, ID 83415, USA, 2000.

[SSi98] M. de St. Simon, private communication.

[Sof81] K. Sofia et al., *Phys. Rev. C* **24**, 1615 (1981).

[Sta98] S.K. Stahl, PhD Thesis, University of Mainz, Germany, 1998.

[Sto90] H. Stolzenberg et al., *Phys. Rev. Lett.* **65**, 3104 (1990).

[Wap00] A. Wapstra, private communication.

[Wer95] T.R. Werner and J. Dudek, *At. Data Nucl. Data Tables* **54**, 1 (1995).

[Wes75] L. Weestgard et al., *Z. Phys. A***275**, 127 (1975).

[Woo99] J.L. Wood et al.,*Nucl. Phys. A* **651**, 323 (1999).

[Wut95] M. Wutz, H. Adam, W. Walcher. *Therie und Praxis der Vakuumtechnik*, Vieweg Verlag, 4th edition 1988.

Danksagung

An dieser Stelle möchte ich all denen meinen Dank aussprechen, die zum Gelingen dieser Arbeit beigetragen haben.

Zunächst möchte ich meinem Doktorvater Prof. H.-Jürgen Kluge danken für das entgegengebrachte Vertrauen, die fortlaufende Unterstützung sowie die Möglichkeit, an ISOLDE/CERN als auch an der GSI arbeiten zu können.

Mein besonderer Dank gilt Prof. Georg Bollen, der mich während der Aufbauphase des RFQs an ISOLDE/CERN unterstützte und geholfen hat, daß am Ende alles funktionierte.

Herrn Priv. Doz. Wolfgang Quint danke ich für die Diskussionsbereitschaft, das ständige Interesse und besonders für die Unterstützung bei der Anfertigung der Dissertation.

Der SHIPTRAP/ISOLTRAP Truppe danke ich für die hervorragende Unterstützung, während der Aufbauphasen, aber auch bei Strahlzeiten und Testmessungen. In diesem Sinne ist diese Arbeit entstanden aus einem Teamwork mit meinen Post-Docs: Gerrit Marx, Johannes Schönfelder, Emily Lamour, Christoph Scheidenberger, Stefan Schwarz und Dietrich Beck, als auch mit meinen Doktorandenkollegen: Günther Sikler, Daniel Rodriques, Christine Weber, Frank Herfurth und Alban Kellerbauer.

Dank gilt auch Prof. R. Bob Moore, von dem ich, während seiner Zeit an der GSI viel lernen konnte und der entscheidend zur ersten Version des RFQ beigetragen hat.

Für die Gelegenheit eine Auswertung der atomaren Massen vornehmen zu können und den damit verbundenen Aufenthalt in Orsay danke ich Prof. Georges Audi.

Ausserdem möchte ich mich für die gute technische Unterstützung von Seiten der Werkstätten und Techniker bedanken, die auch dringende und/oder eigenwillige Aufträge prompt erledigten.

Mein ganz besonderer Dank gilt natürlich meiner Frau Petra und meinen Söhnen Darian und Silas. Ohne deren Unterstützung, Aufmunterung und Hilfe wäre aus dieser Arbeit nichts geworden!